

INFORMATION TO USERS

This manuscript has been reproduced from the microfilm master. UMI films the text directly from the original or copy submitted. Thus, some thesis and dissertation copies are in typewriter face, while others may be from any type of computer printer.

The quality of this reproduction is dependent upon the quality of the copy submitted. Broken or indistinct print, colored or poor quality illustrations and photographs, print bleedthrough, substandard margins, and improper alignment can adversely affect reproduction.

In the unlikely event that the author did not send UMI a complete manuscript and there are missing pages, these will be noted. Also, if unauthorized copyright material had to be removed, a note will indicate the deletion.

Oversize materials (e.g., maps, drawings, charts) are reproduced by sectioning the original, beginning at the upper left-hand corner and continuing from left to right in equal sections with small overlaps. Each original is also photographed in one exposure and is included in reduced form at the back of the book.

Photographs included in the original manuscript have been reproduced xerographically in this copy. Higher quality 6" x 9" black and white photographic prints are available for any photographs or illustrations appearing in this copy for an additional charge. Contact UMI directly to order.

UMI

A Bell & Howell Information Company
300 North Zeeb Road, Ann Arbor MI 48106-1346 USA
313/761-4700 800/521-0600

The Pennsylvania State University

The Graduate School

Department of Materials Science and Engineering

**FUNDAMENTALS OF THE DIRECTED OXIDATION
PROCESS FOR SYNTHESIS OF ALUMINA/ALUMINUM
COMPOSITES**

A Thesis in

Materials Science and Engineering

by

Hari Venugopalan

Submitted in Partial Fulfillment
of the Requirements
for the Degree of

Doctor of Philosophy

May 1996

UMI Number: 9628195

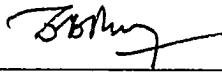
UMI Microform 9628195
Copyright 1996, by UMI Company. All rights reserved.

**This microform edition is protected against unauthorized
copying under Title 17, United States Code.**

UMI
300 North Zeeb Road
Ann Arbor, MI 48103

We approve the thesis of Hari Venugopalan.

Date of Signature



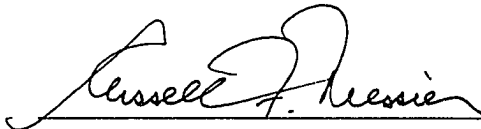
10 January 1996

Tarasankar DebRoy
Professor of Materials Science and Engineering
Thesis Adviser
Chair of Committee



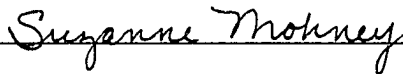
9 January 1996

John R. Hellmann
Associate Professor of Ceramic Science and Engineering



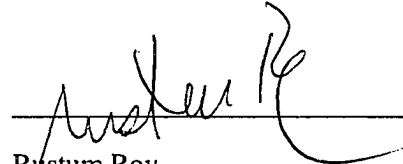
Jan. 9, 1996

Russell F. Messier
Professor of Engineering Science and Mechanics



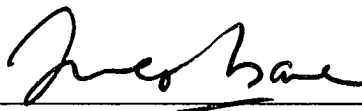
1/9/96

Suzanne Mohney
Assistant Professor of Materials Science and Engineering



1/9/96

Rustom Roy
Evan Pugh Professor of the Solid State



1/15/96

Kwadwo Osseo-Asare
Professor of Metallurgy
In Charge of Graduate Programs in
Metals Science and Engineering

ABSTRACT

Synthesis of oxide matrix composites by the directed metal oxidation process offers significant advantages over traditional composite processing routes. Much of the previous work on directed oxidation has been focused on understanding the microstructural evolution during the process. In this work, the kinetics of formation of $\text{Al}_2\text{O}_3/\text{Al}$ composites from Al-Mg alloys has been examined. In addition, growth kinetics of $\text{Al}_2\text{O}_3/\text{Al}$ composites through Al_2O_3 preforms has been studied. Furthermore, the nature of metal distribution in $\text{Al}_2\text{O}_3/\text{Al}$ composites, and its dependence on growth temperature, have been investigated.

On heating Al-Mg alloys in argon, MgO forms in the initial stage on introduction of oxygen. The amount of MgO formed determines the residual Mg content in the alloy. The onset of alumina formation in the growth stage corresponds to the time required to reduce the Mg composition in the alloy to that at which Al_2O_3 is in equilibrium with the Al-Mg alloy. Thus, it is clear that the amount of MgO which forms in the initial stage and the mechanism of initial stage oxidation are important. A theoretical and experimental approach is used to understand the mechanism of the initial stage of oxidation. The theoretical work involved calculations of velocity, temperature and concentration fields in the gas phase to understand the role of magnesium evaporation in the oxidation behavior of the alloy. The predictions of oxidation rates were compared with the experimental results. The agreement confirms reaction enhanced, gaseous diffusion limited, vaporization of magnesium in the initial stage. It is shown that the interface, where magnesium vapor reacts with oxygen to form MgO, progressively moves towards the alloy surface during the reaction. The end of the initial stage corresponds to the arrival of the oxygen front close to the alloy surface.

The kinetics of Al_2O_3 formation in the growth stage of directed oxidation of Al-Mg and Al-Mg-Si alloys has been investigated theoretically and experimentally. Analysis of the oxidation kinetics of Al-Mg and Al-Mg-Si alloys for various oxygen pressures, temperatures and durations of oxidation demonstrates that the growth kinetics can be tailored by the control of alloy composition. For the Al-Mg alloys, transport of oxygen through a thin alloy layer near the surface controls the growth rate. When Si is added to the alloy, the oxidation mechanism is completely changed. The rate of oxidation of Al-Mg-Si alloys depends on the transport of electronic species through a thin MgO layer at the top surface of the composite. Apart from contributing to a more complete understanding of the growth stage, the mechanism of composite growth will serve as a basis for improving growth rates.

The toughness of $\text{Al}_2\text{O}_3/\text{Al}$ composites is determined by the amount and the nature of metal distribution in the composite. The metal distribution in $\text{Al}_2\text{O}_3/\text{Al}$ composites and its dependence on growth temperature were examined. Electrical conductivities and microstructures of $\text{Al}_2\text{O}_3/\text{Al}$ composites synthesized by directed oxidation of Al-5056 alloy are investigated. The high conductivity of the $\text{Al}_2\text{O}_3/\text{Al}$ composite compared to sintered Al_2O_3 - 4% MgO is shown as a proof of the presence of some continuous metal channels in the composite. The activation energy for the diffusion of the dominant charge carrier in the oxide matrix is found to be 1.36 eV from the analysis of the conductivity data. Both the amount of metal in the composite and the extent of interconnection of the metal channels decrease with increasing growth temperature. The observed changes in microstructure with temperature can be explained by considering temperature variations of grain boundary energies in alumina and the alumina/aluminum interfacial energy. The metal content of the $\text{Al}_2\text{O}_3/\text{Al}$ composites, prepared by directed oxidation of Al-5056 alloys, can be tailored by the choice of the growth temperature.

The mechanism of oxidation of Al-Mg alloys into Al_2O_3 preforms has been investigated theoretically and experimentally. Analysis of the oxidation kinetics for various preform particle sizes, and durations of oxidation, demonstrates that the preform provides preferential sites for Al_2O_3 nucleation. The weight gain rate decreases with increasing Al_2O_3 particle size. With increasing oxidation time, liquid metal transport to the oxidation front slows down and becomes a factor in controlling the weight gain rate. The study demonstrates that the growth kinetics of Al alloys into Al_2O_3 preforms can be tailored by the control of preform particle size.

TABLE OF CONTENTS

	Page
LIST OF FIGURES.....	x
LIST OF TABLES.....	xv
ACKNOWLEDGMENTS.....	xvii
Chapter 1. INTRODUCTION.....	1
1.1 Directed Metal Oxidation.....	1
1.2 Advantages of Directed Metal Oxidation.....	3
1.3 Range of Composites and Their Applications.....	3
1.4 Mechanism of Composite Formation.....	4
1.5 Importance of the Initial Stage.....	6
1.6 Growth Stage Kinetics.....	8
1.7 Metal Distribution in Al ₂ O ₃ /Al Composites.....	10
1.8 Oxidation into Preforms.....	11
1.9 Statement of Objectives.....	11
1.10 Organization of Thesis.....	13
1.11 References.....	14
Chapter 2. BACKGROUND AND PREVIOUS WORK.....	17
2.1 Introduction.....	17
2.2 Oxidation of Liquid Al-Mg Alloys.....	17
2.3 Directed Oxidation of Liquid Al-Mg Alloys.....	20
2.4 Mechanism of Oxidation in the Initial Stage.....	21
2.4.1 Initial Heating in Air.....	21
2.4.2 Initial Heating in Argon.....	21
2.5 Incubation Stage of Directed Oxidation.....	24
2.5.1 Mechanism of Oxidation During Incubation.....	24
2.5.2 Duration of Incubation.....	26
2.6 Growth Stage of Directed Oxidation.....	27

2.6.1	Initiation of Alumina Formation.....	27
2.6.2	Mechanism of Alumina Formation.....	27
2.6.3	Composite Microstructure at the End of the Growth Stage.....	31
2.6.4	Effect of Composite Microstructure on the Mechanical Properties of Al ₂ O ₃ /Al Composites.....	36
2.7	Effect of Process Parameters on Directed Oxidation.....	38
2.7.1	Effect of Alloy Composition.....	38
2.7.2	Effect of Temperature.....	38
2.8	Directed Oxidation into Al ₂ O ₃ Preforms.....	39
2.8.1	Microstructure.....	39
2.8.2	Growth Kinetics.....	39
2.9	Summary.....	40
2.10	References.....	42
Chapter 3. PROCEDURES.....		46
3.1	Description of the Thermogravimetric Set-up.....	46
3.1.1	Pressure and Flow Control System.....	46
3.2	Initial Stage.....	48
3.2.1	Experiments.....	48
3.2.2	Modeling of Heat Transfer and Fluid Flow During the Initial Stage.....	49
3.3	Growth Stage.....	55
3.3.1	Experiments.....	55
3.3.2	Estimation of Al-Mg-Si Liquid Solution Thermodynamics.....	57
3.4	Electrical Conductivity Experiments.....	63
3.4.1	Nature of Metal Distribution in Al ₂ O ₃ /Al Composite.....	63
3.4.2	Dependence of Metal Distribution on Growth Temperature.....	65
3.5	Growth into Preforms.....	66
3.6	References.....	68

Chapter 4.	RESULTS AND DISCUSSION.....	70
4.1	Mechanism of Initial Stage.....	70
4.1.1	Effect of Diffusivity on the Oxidation Rate.....	79
4.1.2	Termination of the Initial Stage.....	80
4.2	Growth Stage Kinetics of Al-Mg Alloys.....	85
4.2.1	Electronic Transport Through MgO.....	91
4.2.1.1	Oxygen Pressure and Time Dependencies..	94
4.2.2	Liquid Metal Transport.....	94
4.2.2.1	Oxygen Pressure and Time Dependencies..	95
4.2.2.2	Predicted Rate vs the Experimental Growth Rate.....	95
4.2.3	Oxygen Transport Through Alloy Film.....	96
4.2.3.1	Flux of Oxygen.....	96
4.2.3.2	Oxygen Pressure and Time Dependencies..	99
4.2.3.3	Predicted Rate vs the Experimental Growth Rate.....	100
4.2.3.4	Activation Energy for Oxygen Transport...	102
4.3	Growth Stage Kinetics of Al-Mg-Si Alloys.....	103
4.3.1	Influence of Silicon on Oxygen Transport Through the Alloy Layer.....	107
4.3.2	Influence of Silicon on Electronic Transport Through MgO.....	110
4.4	Metal Distribution in Al ₂ O ₃ /Al Composite.....	111
4.4.1	Nature of Metal Distribution.....	111
4.4.1.1	Activation Energy for Diffusion.....	115
4.4.2	Dependence of Metal Distribution in Al ₂ O ₃ /Al Composite on Growth Temperature.....	118
4.5	Oxidation into Preforms.....	124
4.5.1	Initial Stage.....	126
4.5.2	Growth Stage.....	130
4.5.2.1	Oxygen Transport.....	133

4.5.2.2	Liquid Metal Transport.....	138
4.6	References.....	143
Chapter 5.	SUMMARY AND CONCLUSIONS.....	148
APPENDIX A	CALCULATION OF BINARY DIFFUSION COEFFICIENT..	151
APPENDIX B	ADAPTATION ROUTINE FOR THE CALCULATION OF RATE OF MAGNESIUM VAPORIZATION FROM THE Al- Mg ALLOY.....	152
APPENDIX C	ESTIMATION OF ACTIVITY COEFFICIENT OF Mg AND Al IN Al-Mg-Si MELT.....	168
APPENDIX D	DETERMINATION OF RATE EXPRESSION FOR LIQUID METAL TRANSPORT.....	171
APPENDIX E	DETERMINATION OF ELECTRICAL CONDUCTIVITY OF AN Al ₂ O ₃ /Al COMPOSITE CONTAINING TORTUOUS METAL CHANNELS.....	174

LIST OF FIGURES

Figure		Page
1.1	Schematic description of formation of ceramic matrix composites by the directed oxidation process.....	2
1.2	Schematic plot of weight gain as a function of time for directed oxidation of Al-Mg alloys.....	7
1.3	Schematic diagram of the composite structure.....	9
2.1	Oxidation features of liquid Al-Mg alloys [2].....	19
2.2	Estimated phase diagram showing the stability of various phases in the Al-Mg-O system [17]. Also shown are the liquidus (T_L) and the solidus lines (T_S).....	22
2.3	Schematic of possible mechanism leading to channel initiation within oxide buds at the start of incubation [13].....	25
2.4	Microstructure of the composite growth front illustrating the MgO/metal/ Al_2O_3 layered structure [20].....	28
2.5	Plot of growth rate data of Al-10 wt% Si -3 wt% Mg alloys. Data set shows consistency with both an activation energy of 370 kJ/mole and oxygen partial pressure dependence of $P_{O_2}^{1/4}$ [20].....	30
2.6	Plot of growth rate data of Al- 5 wt% Mg alloys, with and without Pt wires [16].....	32
2.7	Bright field TEM micrograph showing a low-angle Al_2O_3 - Al_2O_3 grain boundary and a high-angle Al/ Al_2O_3 grain boundary in Al_2O_3 /Al composite produced by directed oxidation[28].....	34
3.1	Schematic diagram of the thermogravimetric setup.....	47
3.2	Schematic diagram of the computational domain chosen for calculation of velocity, temperature and concentration fields of Mg	

	vapor and oxygen.....	52
3.3	Measured temperature profile along the wall of the TGA reactor...	53
3.4	Schematic description of the near surface aluminum alloy layer present in the growth stage of directed oxidation.....	58
3.5	Schematic description of Al-Mg-Si thermodynamics from the limiting binaries using the shortest distance composition path. Al-Mg-Si thermodynamics at composition A, estimated from the thermodynamics of Al-Mg at composition P, of Mg-Si at composition Q, and of Al-Si at composition R, respectively.....	60
3.6	Schematic description of the conductivity setup.....	64
4.1	Plot of weight gain in the initial stage vs time for various oxygen pressures.....	71
4.2	X-ray diffraction pattern of the white powder formed on the crucible walls, during the initial stage of oxidation of Al-Mg alloys.....	72
4.3	Computed velocity and concentration profiles of magnesium and oxygen in the gas phase, for an oxygen pressure of 3266 Pa, total pressure of 93303 Pa at 1391 K, at the initiation of the experiment. (Note $1 \text{ gm/cm}^3 = 10^3 \text{ kg/m}^3$).....	74
4.4	Schematic diagram showing the magnesium and oxygen boundary layers formed in the gas phase above the melt, and within the crucible, during the initial stage of oxidation of Al-Mg alloys.....	76
4.5	Comparison of experimental and calculated weight gain vs time for oxygen pressures of (a) 3266 Pa and (b) 39187 Pa. Experiments were done at 1391 K and 93303 Pa total pressure....	78
4.6	Weight gain vs time during initial stage of oxidation of Al-Mg alloys in O ₂ -Ar and O ₂ -He atmospheres.....	81
4.7	(a) Weight gain vs time in the initial stage of oxidation for different total pressures. (b) Weight gain rate in the initial stage vs	

	oxygen diffusivity in the reactive atmosphere.....	82
4.8	Computed concentration profiles of magnesium and oxygen in the gas phase, for an oxygen pressure of 3266 Pa, total pressure of 93303 Pa at 1391 K. The profiles show the movement of the oxygen front towards the melt surface with time. (Note $1 \text{ gm/cm}^3 = 10^3 \text{ kg/m}^3$).....	84
4.9	Computed variation in the thickness of the Mg boundary layer (δ) during the initial stage of directed oxidation as a function of time for two different partial pressures of oxygen.....	86
4.10	Weight gain vs time for the Al-Mg alloy at different oxygen pressures in the growth stage: (a) 85092 Pa, (b) 21273 Pa, and (c) 42546 Pa. The oxygen pressure was initially maintained at 85092 Pa and subsequently changed in the growth stage. The total pressure, temperature and the total gas flow rate were maintained constant at 93303 Pa, 1373 K, and 8333 mm^3/s STP, respectively.....	87
4.11	Weight gain rate vs temperature for Al-Mg alloy for an oxygen pressure of 85092 Pa. The total pressure and the total gas flow rate were maintained constant at 93303 Pa and 8333 mm^3/s STP, respectively.....	88
4.12	Macrostructure of composite grown from Al-5 wt% Mg alloy.....	90
4.13	Weight gain vs time for the Al-Mg-Si alloy at different temperatures: (a) 1393 K, (b) 1508 K, and (c) 1612 K. The total pressure, oxygen pressure and the total gas flow rate were maintained constant at 93303 Pa, 93303 Pa, and 8333 mm^3/s STP, respectively.....	104
4.14	Weight gain rate vs temperature for Al-Mg-Si alloy for an oxygen pressure of 93303 Pa. The total pressure and the total gas flow rate were maintained constant at 93303 Pa and 8333 mm^3/s STP,	

	respectively.....	105
4.15	Calculated equilibrium oxygen solubility in the Al-Mg alloy film at (a) the MgO/alloy film interface, and (b) the Al ₂ O ₃ /alloy film interface for varying magnesium contents.....	108
4.16	Calculated equilibrium oxygen solubility in the Al-Mg-10 wt% Si alloy film at (a) the MgO/alloy film interface, and (b) the Al ₂ O ₃ /alloy film interface for varying magnesium contents.....	109
4.17	Electrical conductivity of Al ₂ O ₃ /Al composite and sintered Al ₂ O ₃ -4 wt% MgO at various temperatures. Measurements were made in argon at 1-atm pressure and a gas flow rate of 500 sccm.....	112
4.18	Arrhenius plot of $\ln(\sigma T)$ vs $1000/T$ for determination of the activation energy for the diffusion of the dominant charge carrier in sintered Al ₂ O ₃ - 4 wt% MgO.....	117
4.19	Electrical conductivity of Al ₂ O ₃ /Al composites, as a function of the growth temperature. Measurements were made at 298 K in argon at 1-atm pressure and a gas flow rate of 500 sccm.....	119
4.20	SEM micrographs showing the general microstructural features of composites produced by directed melt oxidation of Al-5056 alloy at different temperatures (a) 1393 K, (b) 1508 K, and (c) 1612 K.	120
4.21	Schematic representation of conditions for formation of metal channels (a) Metal channels cannot form ($\gamma_{SS} < 2 \gamma_{SL}$) (b) Metal channels can form in the grain boundary($\gamma_{SS} > 2 \gamma_{SL}$).....	122
4.22	Weight gain vs time for directed oxidation of Al-Mg alloy at 1450 K into Al ₂ O ₃ preforms of different particle sizes. The weight gain vs time plot for the base alloy is also shown. The oxygen pressure, total pressure and the total gas flow rate were maintained constant at 85092 Pa, 93303 Pa and 8333 mm ³ /s STP, respectively.....	125
4.23	Weight gain per unit area vs time for directed oxidation of Al-Mg	

	alloy at 1450 K into Al_2O_3 preforms of different particle sizes. The weight gain per unit area vs time plot for the base alloy is also shown. The oxygen pressure, total pressure and the total gas flow rate were maintained constant at 85092 Pa, 93303 Pa and 8333 mm^3/s STP, respectively.....	127
4.24	Weight gain per unit area vs time in the initial stage of directed oxidation of Al-Mg alloy at 1450 K into Al_2O_3 preforms of different particle sizes: (a) 8 μm , (b) 16 μm , (c) 110 μm , and (d) 0.53 μm . The weight gain per unit area vs time plot in the initial stage for the base alloy (e) is also shown. Data correspond to the initial stage in Fig. 4.23.....	128
4.25	Parabolic kinetics in the growth stage of directed oxidation of Al-Mg alloy at 1450 K into Al_2O_3 preforms of different particle sizes. Data correspond to the growth stage in Fig. 4.22.....	131
4.26	Weight gain per unit area vs time for directed oxidation of Al-Mg alloy at 1450 K into Al_2O_3 preform of 8 μm particle size at different oxygen pressures: (a) 21273 Pa, and (b) 85092 Pa. The total pressure and the total gas flow rate were maintained constant at 93303 Pa and 8333 mm^3/s STP, respectively.....	132
4.27	Schematic diagram showing the movement of the oxidation front from (a) to (c), as directed oxidation of Al-Mg alloy proceeds through an Al_2O_3 preform.....	140
B.1	Schematic diagram of the computational domain chosen for calculation of velocity, temperature and concentration fields of Mg vapor and oxygen.....	153
E.1	Schematic representation of metal channels in an $\text{Al}_2\text{O}_3/\text{Al}$ composite.....	175

LIST OF TABLES

Table		Page
1.1	Examples of Lanxide® ceramic matrix systems [1].....	5
2.1	Relative proportions of various phases in the bulk and bottom of the Al ₂ O ₃ /Al composite, produced by directed oxidation of Al-2.5 wt% Mg alloy [24].....	35
2.2	Effect of metal volume fraction and interconnectivity on flexural strength and toughness of Al ₂ O ₃ /Al composite [28].....	37
3.1	Data used in the modeling of the initial stage.....	51
3.2	Nominal composition of the alloys used for directed oxidation experiments.....	56
3.3	Excess free energies of mixing for Al-Si, Mg-Si and Al-Mg binaries.....	61
3.4	Description of the characteristics of the alumina preforms used in the directed oxidation of Al-5 wt% Mg alloy.....	67
4.1	Characteristics of various events in the growth stage of Al-5 wt% Mg alloy.....	93
4.2	Data used for the calculation of the rate of liquid metal transport during the growth stage.....	97
4.3	Data used in the calculation of rate of oxygen transport through the near surface alloy layer.....	101
4.4	Growth rate of Al-Mg-Si alloy as a function of oxygen pressure at 1612 K.....	106
4.5	Volume fraction of metal in Al ₂ O ₃ /Al composites as a function of the growth temperature.....	121

4.6	Maximum weight gain rate as a function of Al_2O_3 particle size, for infiltration of Al-Mg alloy into Al_2O_3 preforms at 1450 K.....	135
4.7	Data used in the calculation of rate of oxygen transport through the near surface alloy layer.....	136
4.8	A_w as a function of Al_2O_3 particle size, for infiltration of Al-Mg alloy into Al_2O_3 preforms at 1450 K.....	137
4.9	Weight gain rate as a function of Al_2O_3 particle size, at 30000 s, for infiltration of Al-Mg alloy into Al_2O_3 preforms at 1450 K.....	141
B.1	Sample output of the program used for modeling the initial stage.....	165

ACKNOWLEDGMENTS

I would first like to extend my gratitude to my thesis advisor, Dr. Tarasankar DebRoy, for all the help and guidance during the course of this investigation. I also wish to thank Dr. J. Hellmann, Dr. R. Messier, Dr. S. Mohny, and Dr. R. Roy for the time, effort and valuable advice while serving with Dr. DebRoy on my thesis committee. I had the pleasure of working with Dr. Kanishka Tankala during the course of this study. His advice and suggestions are deeply appreciated. My thanks to Dr. Kamlesh Mundra for his help, especially in modeling the initial stage of oxidation. My thanks to Mr. T. Palmer for his help with the SEM. I wish to acknowledge my gratitude to my family for their support. My special thanks to Mr. A. Kebede for friendly advice and for helping me with the TGA set-up.

This work was supported by the National Science Foundation, Division of Materials Research under Grant No. DMR-9118075.

CHAPTER 1

INTRODUCTION

1.1 Directed Metal Oxidation

In most structural applications, the primary disadvantage of ceramics is their lack of toughness. As a result, they are sensitive to sudden failure in response to accidental overloading, contact damage, or rapid temperature cycling. This deficiency has led to attempts to produce ceramic matrix composites which provide adequate toughness and other desirable properties. The directed oxidation of molten aluminum alloys by vapor phase oxidants (DIMOX), developed by Lanxide Corporation, can be used to produce tough ceramic matrix composites [1]. Fig. 1.1 illustrates schematically the formation of composite materials in this process. Under appropriate conditions of alloy composition, temperature and oxygen pressure, a rapid reaction of the molten alloy with the oxidant to form α -alumina occurs and the reaction product grows outward from the original metal surface. The reaction is fed by transport of liquid metal through the reaction product. The resulting material is a $\text{Al}_2\text{O}_3/\text{Al}$ composite with a network of unoxidized metal. The fact that over 2700 patents have been filed world-wide and the first hundred or so US patents have been allowed [2] are quantitative indices of the significance of this process. Reinforced composites with the desired structural properties can be obtained by growing the "composite" matrix into preforms consisting of reinforcing particulates, whiskers or fibers of Al_2O_3 , SiC etc. [3-5].

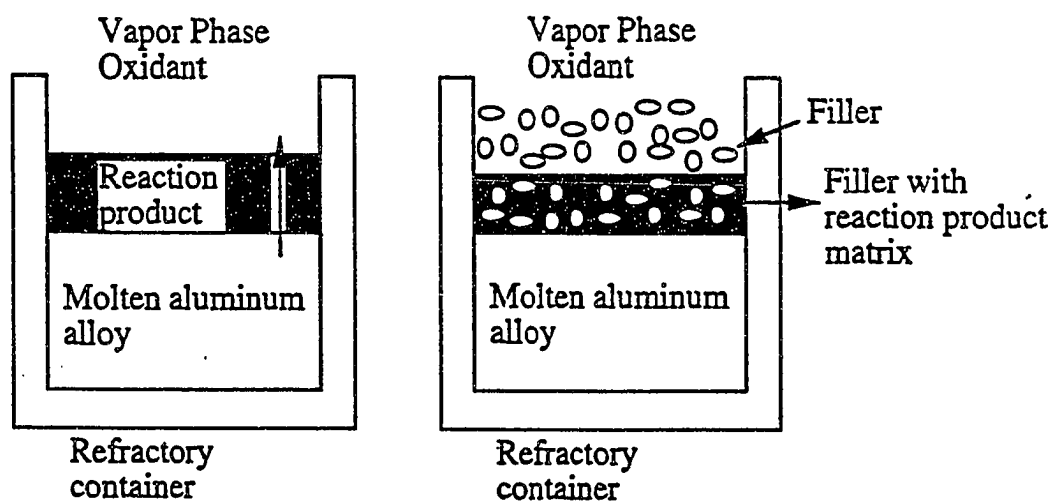


Fig. 1.1 Schematic description of formation of ceramic matrix composites by the directed oxidation process.

1.2 Advantages of Directed Melt Oxidation

The primary advantages of this process include its ability to economically form near-net shapes with tailored microstructures, with varying amounts of metal (5-30 vol %) and ceramic in the composite [5]. For example, at low temperatures, the unreacted metal in the $\text{Al}_2\text{O}_3/\text{Al}$ composite serves as a ductile toughening phase while tailored interfaces between the reaction product and the ceramic preform may provide additional toughness by debonding and fiber-pullout mechanisms [6]. For high temperature applications, the metal can be removed, by treating with nickel aluminate filler, to form an $\text{Al}_2\text{O}_3/\text{NiAl}$ composite, which is reported to have better high-temperature properties than the $\text{Al}_2\text{O}_3/\text{Al}$ composite [7]. Conventional processing of ceramic matrix composites (CMCs) involves the powder metallurgy technique of mechanical mixing of the matrix and reinforcement and subsequent forming and sintering. The absence of a sintering step in DIMOX eliminates residual binders in the composite and differential shrinkage during densification. Thus, unlike traditional ceramic processing, the growth of a composite matrix into preforms by the directed oxidation route involves no change in dimensions. Finally, the ample range of starting materials (alloys and fillers) and processing conditions (temperature, oxidant atmosphere) that can be used in this technology, provide great flexibility in tailoring the product microstructure and thus its properties to specific needs.

1.3 Range of Composites and their Applications

Composites made by directed oxidation can be tailored to have good toughness, thermal shock resistance, wear resistance, high stiffness, and high temperature stability. SiC fiber-reinforced Al_2O_3 matrix composites, made by growing the Al_2O_3 matrix around the fibers, have excellent thermal shock resistance and, are being evaluated for components in gas turbine engines like flame holders, turbine shrouds, exit vanes, and combustor parts [7].

Al_2O_3 matrix composites reinforced with coarse SiC particles have a higher wear resistance compared to partially stabilized zirconia (PSZ), and have been commercialized for armor applications [5]. Al_2O_3 matrix composites containing fine SiC particles have been developed for high temperature applications, such as furnace and heat exchanger components [5]. Several other ceramic composite systems based on the directed-metal-oxidation technology have been developed, as listed in Table 1.1 [3]. Typically the reaction involves a molten metal and a gas; however, the directed reaction of molten zirconium with solid B_4C has been used to make ZrB_2 -platelet reinforced ZrC composites and are being evaluated for use in rocket engines [8]. Recently, an important group of structural ceramics, the so-called NZP ($\text{NaZr}_3\text{P}_3\text{O}_{12}$) materials, have been synthesized by the directed oxidation route [9]. NZP materials are characterized by high ionic conductivity, and low and tailorable thermal expansion, and thermal expansion anisotropy. Thus, the directed oxidation process has demonstrated its ability to produce several technologically important composite structures and a promise for the development of a new class of composite materials. However, the scientific basis for the oxidation behavior involved in the process is far from fully understood.

1.4 Mechanism of Composite Formation

In the past few years, the growth of $\text{Al}_2\text{O}_3/\text{Al}$ composites by the directed oxidation route has been the subject of several microstructural studies. A few kinetic studies have also been carried out. It is now recognized that the presence of volatile elements like Li, Na, Mg or Zn is crucial for directed oxidation to take place [1,10-12]. Dopants like Li, Na, Mg or Zn are believed to hinder the formation of a protective alumina film on the alloy surface and thus allow continued oxidation of the alloy. Additional elements such as Si are usually necessary to increase composite formation rates, and/or to improve alloy/preform

Table 1.1 Examples of Lanxide®* ceramic matrix systems [1].

Parent metal	Reaction product
Al	Oxide, nitride, boride, titanate
Si	Nitride, boride, carbide
Ti	Nitride, boride, carbide
Zr	Nitride, boride, carbide
Hf	Boride, carbide
Sn	Oxide
La	Boride

* Lanxide® is a registered trademark of Lanxide Corporation, DE.

compatibility. These dopants can be either applied to the surface of the aluminum exposed to the oxidant, or if soluble, alloyed with the parent metal. The microstructural evolution during directed oxidation has already been outlined in the early investigations. Three distinct stages can be observed in the oxidation of Al-Mg alloys at a given temperature [13] (Fig. 1.2). An initial stage of rapid weight gain occurs, corresponding to the formation of MgO [13]. Formation of a dense, thin layer of MgAl_2O_4 beneath the MgO halts the initial stage of oxidation and corresponds to the start of incubation [13]. During incubation, metal channels are observed to form in the spinel and the arrival of these metal channels to the top of the spinel is believed to correspond to the end of incubation and the start of the growth stage [14]. Composite formation in the growth stage starts when the near surface aluminum alloy becomes depleted in Mg and reaches a concentration where Al_2O_3 formation becomes more favorable than MgAl_2O_4 [14]. During growth, molten Al is believed to be transported by wicking (capillary action), from the bulk alloy, to the top surface where oxidation of Al to Al_2O_3 occurs [15].

1.5 Importance of the Initial Stage

The amount of aluminum converted to alumina in the growth stage is critically dependent on the Mg composition in the alloy [1,13]. The processing time (the total time required to convert all the aluminum in the alloy to alumina) is essentially dominated by the time required for alumina formation to commence [13] and can be reduced by reducing the onset time. The onset of the alumina formation corresponds to the time required to reduce the Mg composition in the alloy from the original concentration to that at which alumina is in equilibrium with the Al-Mg alloy [14]. Since the residual Mg content in the alloy is controlled by the amount of MgO that forms in the initial stage, the mechanism of initial stage is clearly important. Formation of MgO in the initial stage of oxidation

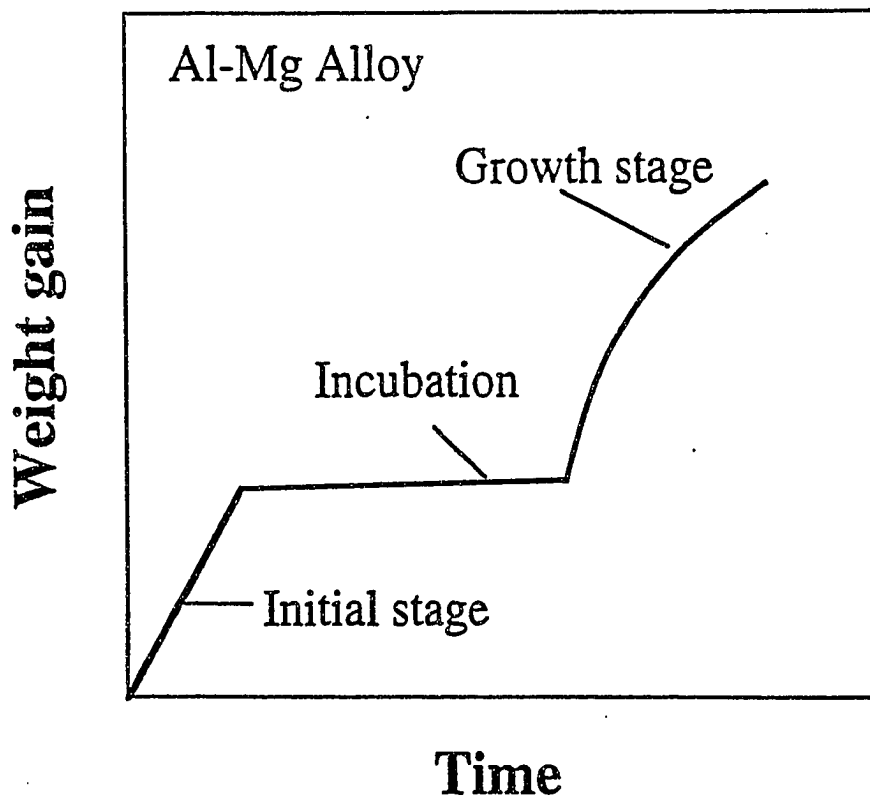


Fig. 1.2 Schematic plot of weight gain as a function of time for directed oxidation of Al-Mg alloys.

has been observed by several investigators. Vlach et al. [13] suggested that the formation of MgO in the initial stage of oxidation occurs by reaction enhanced, gaseous diffusion limited, vaporization of Mg followed by its oxidation. However, no experimental evidence was presented to corroborate the suggested mechanism. They [13] also suggested that the initial stage of oxidation ends when a dense layer of spinel forms on the surface of the melt and prevents further vaporization of magnesium. However, no explanation for the sudden formation of spinel, leading to the sharp decrease in rate at the end of the initial stage of oxidation, was presented. Although the amount of MgO at the melt surface plays an important role in the bulk oxidation of Al-Mg alloys, a review of literature on directed oxidation of aluminum alloys reveals that the mechanism and the reason for the abrupt end of the initial stage of oxidation is not completely understood.

1.6 Growth Stage Kinetics

Several models have been proposed to explain the kinetics of oxidation of Al to Al_2O_3 in the growth stage [13,16]. It has been suggested that during the growth stage of directed oxidation of Al-Mg alloys, a continuous MgO film exists at the top of the alumina matrix with a thin aluminum alloy film separating the two layers [15,17] (Fig. 1.3). The presence of this continuous MgO film restricts the formation of a protective alumina layer on the surface. At the MgO/Al-alloy film interface, MgO dissociates and oxygen dissolves in the Al-alloy film. The magnesium ions formed by dissociation of MgO diffuse through the MgO layer to the MgO/air interface where they are oxidized to regenerate MgO. During the outward transport of magnesium ions through MgO, electrical neutrality is maintained by the simultaneous transport of electronic defects [16]. The oxygen dissolved in the alloy film is transported, from the MgO/alloy film

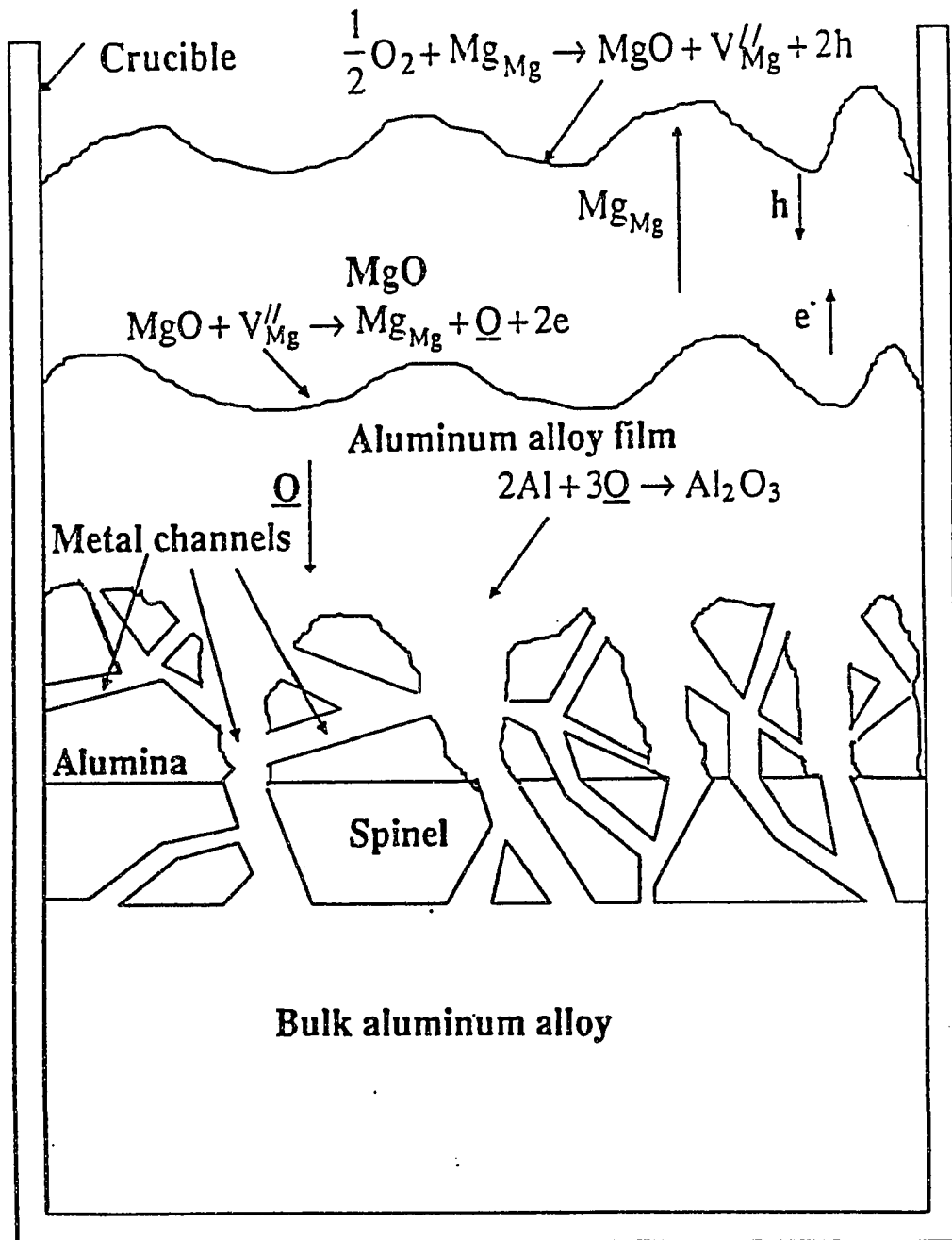


Fig. 1.3 Schematic diagram of the composite structure.

interface, to the alloy film/ Al_2O_3 interface where composite growth takes place. The supply of aluminum to the alloy film/ Al_2O_3 interface is thought to be sustained by the wicking of metal through channels in the alumina. One or more of the above mentioned reaction steps could be the rate controlling mechanism in the growth stage.

Nagelberg et al. [16] conducted directed oxidation studies of Al-Mg alloys to which Si was added. According to Nagelberg et al. [16], the rate of oxidation of Al-Mg-Si alloys in the growth stage is controlled by the electronic conductivity of the continuous, external, MgO layer. To investigate the role of electronic transport in the oxidation kinetics in the growth stage, DebRoy et al. [18] carried out directed oxidation experiments of an Al-Mg alloy (Al-5056 alloy) in which platinum wires were positioned inside the alloy so that the wires would extend through the composite matrix and the top MgO layer to facilitate electronic transport. They [18] observed that the rate of oxidation in the growth stage was independent of the presence or absence of Pt wires indicating that the transport of electronic species does not control the oxidation kinetics of Al-Mg alloys that do not contain silicon. Thus, in the absence of silicon, electronic transport through the MgO layer is no longer the rate controlling mechanism in the growth stage of Al-Mg alloys. In view of the crucial difference in the oxidation mechanism of Al-Mg alloys with or without the presence of Si, the role of silicon on the mechanism of composite growth from Al-Mg alloys needs to be investigated in detail.

1.7 Metal Distribution in $\text{Al}_2\text{O}_3/\text{Al}$ Composites

The presence of narrow channels of alloy in selected microscopic sections in the oxide composite has been presented as "evidence" of the wicking process [19]. However, the observation of a few alloy channels in an arbitrarily selected microscopic section does not really constitute a rigorous proof that the narrow metal channels extend from the bulk liquid

metal at the bottom all the way through the ceramic oxide matrix to the top. It is known that the amount, and the extent of interconnection, of the aluminum metal remaining in the composite, at the end of the growth stage, control the toughness of the composite [20]. Therefore, the effect of an important reaction parameter like oxidation temperature on the degree of metal interconnection needs to be addressed.

1.8 Oxidation into Preforms

The practical utilization of directed melt oxidation lies in the ability to form the oxidation product in a porous preform (filler material). The preform may be reactive (e.g. SiC) or inert (e.g. Al₂O₃) with respect to the aluminum melt. Watari et al. [21] observed that the presence of Al₂O₃ preforms decreased the oxidation rate of aluminum alloys. They also observed that the composite growth rate decreased with decreasing pore size of the Al₂O₃ preform. Nagelberg [22] observed that the growth rate of aluminum alloys into Al₂O₃ preforms, in an oxygen atmosphere, initially increased rapidly and subsequently decreased as matrix growth proceeded through the preform. It is clear from these experimental observations [21-22] that while Al₂O₃ preforms can provide sites for the epitaxial nucleation of fresh Al₂O₃, the loose preform can also provide a tortuous path for metal wicking to the growth surface and, thus, limit liquid metal transport. The effect of preform particle size on the interplay between secondary nucleation and liquid metal transport, and their effects on the composite growth rate, need to be addressed.

1.9 Statement of Objectives

The overall objective of this study is to investigate the rate phenomena and the mechanism of synthesis of oxide based composites, with and without filler materials, by directed oxidation of aluminum alloys.

In the directed metal oxidation of aluminum alloys, three distinct stages can be observed. An initial stage of rapid weight gain, corresponding to the formation of MgO, terminates with the formation of a dense layer of MgAl_2O_4 spinel. This signifies the start of incubation. The arrival of metal channels at the top of the spinel corresponds to the end of incubation and the start of the growth stage. During growth, molten aluminum is believed to be transported by wicking from the bulk alloy to the top surface where oxidation of Al to Al_2O_3 occurs.

The principles of heat transfer, fluid flow and mass transfer have been applied to understand the mechanism of the initial stage of oxidation. Kinetics of oxidation in the growth stage of Al-Mg alloys and Al-Mg-Si alloys have also been analyzed by thermogravimetry. The specific questions addressed are: What is the mechanism of the initial stage of oxidation? Why does the initial stage end abruptly? What determines the extent of incubation? What is the mechanism of composite formation in the growth stage of Al-Mg alloys? Does the silicon additions to Al-Mg alloy shift the oxidation mechanism from oxygen transport through the near surface alloy layer to electronic transport through MgO? How does the oxidation kinetics of Al-Mg alloys change in the presence of Al_2O_3 preforms? The answers to these basic questions are sought through both experimental and theoretical work.

An understanding of the metal distribution in $\text{Al}_2\text{O}_3/\text{Al}$ composites was sought through electrical conductivity measurements. The study was focused on seeking answers to the following questions: What is the evidence for liquid metal transport by capillarity? What is the nature of metal distribution in $\text{Al}_2\text{O}_3/\text{Al}$ composites? How does the metal distribution in $\text{Al}_2\text{O}_3/\text{Al}$ composites vary with temperature?

1.10 Organization of Thesis

The thesis is divided into five chapters.

Chapter 1 is the introduction. This chapter presents the important problems and issues related to the rates of directed oxidation of aluminum alloys with an emphasis on (a) the initial and growth stages of oxidation, (b) the metal distribution in $\text{Al}_2\text{O}_3/\text{Al}$ composites, and (c) oxidation into preforms. Chapter 2 is a review of the literature relevant to the mechanism of the various stages of directed oxidation and the progress made in understanding the kinetics of oxidation of Al-Mg alloys, with or without silicon. The third chapter is devoted to the description of the experimental procedures and the theoretical approach used in this study. It includes the experiments conducted and the data analysis undertaken to understand the mechanism of oxidation of Al-Mg alloys in the initial and growth stages, and to examine the role of silicon in the alloy on the growth rate. The role of Al_2O_3 preforms on the growth rate of Al alloys is also investigated. The metal distribution in the $\text{Al}_2\text{O}_3/\text{Al}$ composites is studied by electrical conductivity measurements and microstructural analysis. The experimental and theoretical results are presented and discussed in the fourth chapter. Finally, chapter 5 represents the conclusions of this study.

1.11 References

1. M. S. Newkirk, A. W. Urquhart, H.R. Zwicker and E. Breval, "Formation of Lanxide™ Ceramic Composite Materials," *J. Mater. Res.*, **8** [7-8] 879 (1987).
2. A. W. Urquhart, "Molten Metals Sire MMC's and CMC's," *Adv. Mater. Proc.*, No. 7, 25-29 (1991).
3. M. S. Newkirk, H. D. Lesher, D. R. White, C. R. Kennedy, A. W. Urquhart, and T. D. Claar, "Ceramic Matrix Composites: Matrix Formation by the Directed Oxidation of Molten Metals," *Ceram. Eng. Sci. Proc.*, **6** [9] 1964-81 (1991).
4. C. A. Andersson, P. Barron-Antolin, G. H. Schiroky and A. S. Fareed, "Properties of Fiber-Reinforced Lanxide™ Alumina Matrix Composites," *Whisker and Fiber Toughened Ceramics*, ASM International, Materials Park, OH, 1988, pp 209-15.
5. A. W. Urquhart, "Novel Reinforced Ceramics and Metals: A Review of Lanxide's Technologies," *Materials Science and Engineering*, **A144** 75-82 (1991).
6. M. D. Thouless and A. G. Evans, "Effects of Pullout on the Mechanical Properties of Ceramic-Matrix Composites," *Acta Metall.*, **36** [3] 517-22 (1988).
7. A. S. Fareed, B. Sonuparlak, C. T. Lee, A. J. Fortini and G. H. Schiroky, "Mechanical Properties of 2-D Nicalon™ Fiber Reinforced Lanxide™ Aluminum Oxide and Aluminum Nitride Matrix Composites," *Ceram. Eng. Sci. Proc.*, **11** [7-8] 782-794 (1990).
8. W. B. Johnson, T. D. Claar and G. H. Schiroky, "Preparation and Processing of Platelet Reinforced Ceramics by the Directed Reaction of Zirconium with Boron Carbide," *Ceram. Eng. Sci. Proc.*, **10** [7-8] 588-98 (1989).
9. E. Breval, "Thermal Expansion Characteristics of NZP, $\text{NaZr}_2\text{P}_3\text{O}_{12}$ -Type Materials, a Review," *Brit. Ceram. Trans.*, **94** [1] 27-32 (1995).
10. A. S. Nagelberg, "Growth Kinetics of Al_2O_3 /Metal Composites From a Complex Aluminum Alloy," *Solid State Ionics*, **32/33**, 783-88 (1989).
11. P. Xiao and B. Derby, "Alumina/Aluminum Composites Formed by the Directed Oxidation of Aluminum Using Sodium Hydroxide as a Surface Dopant," *J. Am. Ceram. Soc.*, **77** [7] 1771-76 (1994).

12. M. S. Newkirk and S. F. Dizio, Novel Ceramic Materials and Methods for Making the Same, European Patent, Application No. 85301820.8
13. K. C. Vlach, O. Salas, H. Ni, V. Jayaram, C. G. Levi and R. Mehrabian, "A Thermogravimetric Study of the Oxidative Growth of Al₂O₃/Al Composites," *J. Mater. Res.*, **6** [9] 1982-95 (1991).
14. O. Salas, V. Jayaram, K. C. Vlach, C. G. Levi and R. Mehrabian, "Early Stages of Composite Formation by Oxidation of Liquid Aluminum Alloys," *J. Am. Ceram. Soc.*, **78** [3] 609-22 (1995).
15. O. Salas, H. Ni, V. Jayaram, K. C. Vlach, C. G. Levi and R. Mehrabian, "Nucleation and Growth of Al₂O₃/Metal Composites by Oxidation of Aluminum Alloys," *J. Mater. Res.*, **6** [9] 1964-81 (1991).
16. A. S. Nagelberg, S. Antolin, and A. W. Urquhart, "Formation of Al₂O₃/Metal Composites by Directed Oxidation of Molten Aluminum-Magnesium-Silicon Alloys: Part II, Growth Kinetics," *J. Am. Ceram. Soc.*, **75** [2] 455-62 (1992).
17. S. Antolin, A. S. Nagelberg and D. K. Creber, "Formation of Al₂O₃/Metal Composites by Directed Oxidation of Molten Aluminum-Magnesium-Silicon Alloys: Part I, Microstructural Development," *J. Am. Ceram. Soc.*, **75** [2] 447-54 (1992).
18. T. DebRoy, A. Bandhopadhyay and R. Roy, "Oxide Matrix Composite by Directional Oxidation of a Commercial Aluminum-Magnesium Alloy," *J. Am. Ceram. Soc.*, **77** [5] 1296-1300 (1994).
19. E. Breval, M. K. Aghajanian and S. J. Luszcz, "Microstructure and Composition of Alumina/Aluminum Composites Made by Directed Oxidation of Aluminum," *J. Am. Ceram. Soc.*, **73** [9] 2610-14 (1990).
20. M. K. Aghajanian, N. H. Macmillan, C. R. Kennedy, S. J. Luszcz and R. Roy, "Properties and Microstructure of Lanxide® Al₂O₃- Al Ceramic Composite Materials," *J. Mat. Sci.*, **24** 658-70 (1989).
21. T. Watari, K. Mori, T. Torikai, and O. Matsuda, "Growth of Alumina/Metal Composites into Porous Ceramics by the Oxidation of Aluminum," *J. Am. Ceram. Soc.*, **77** [10] 2599-602 (1994).

22. A. S. Nagelberg, "The Effect of Processing Parameters on the Growth Rate and Microstructure of Al₂O₃/Metal Matrix Composites," *Mater. Res. Soc. Symp. Proc.*, **155**, 275 (1989).

CHAPTER 2

BACKGROUND AND PREVIOUS WORK

2.1 Introduction

It is now recognized that the presence of Mg is crucial for directed oxidation of aluminum alloys to take place [1]. The active role of Mg in the conventional oxidation of Al alloys has long been known. A number of studies [2-10] have been conducted to understand the effect of Mg on the oxidation of liquid aluminum alloys. In the past, the objective had been to limit the harmful effect of Mg [2], since Mg additions to Al alloys usually result in oxide formation. In contrast, in the DIMOX™ technology, the enhanced oxidation that results from alloying Al with Mg [1] is specifically sought. In addition, prior to the advent of the DIMOX™ technology, almost all of the oxidation studies on Al-Mg alloys had been conducted under conditions in which the formation of Al₂O₃/Al composites does not occur. Nevertheless, the early investigations can provide useful insight in elucidating the mechanism of directed oxidation of Al-Mg alloys.

2.2 Oxidation of Liquid Al-Mg Alloys

A review of the literature [2-10] indicates that very rarely has a mechanistic study been conducted to explain the observed oxidation behavior. A comprehensive study was carried out by Cochran et al. [2]. They covered wide composition ranges (1-14 wt% Mg), oxidation temperatures (873-1373 K), oxidant atmospheres (oxygen, air, flue gas and carbon dioxide), and heating procedures. The observed oxidation features are schematically

shown in Fig. 2.1. Initially, the oxidation rate is low. During this initial period a protective film of amorphous MgO is formed [2-6]. Subsequently MgO crystallizes. This is accompanied by an acceleration of the oxidation which proceeds until all the Mg is oxidized, either as MgAl_2O_4 or MgO. It can be seen from Fig. 2.1 that the time required for this acceleration of oxidation of Al-Mg alloys decreases with increasing temperature and increasing Mg concentration in the alloy. Subsequently, the oxidation rate becomes negligible [2-6,10].

While most of the earlier investigations [2-6,10] only reported MgO and/or MgAl_2O_4 as the oxidation products, there are indications that, in a few instances, formation of an $\text{Al}_2\text{O}_3/\text{Al}$ composite may have occurred. For example, the weight gains reported in the oxidation studies of Drouzy et al. [4] were as high as 80%. In addition, the oxidized samples displayed a “mushroom” morphology [4], which is similar to the morphology of the composite structure obtained by directed oxidation [1]. Furthermore, complete conversion of the 6% magnesium in the alloy to MgO and MgAl_2O_4 would only result in weight gains of 4% and 16% respectively. In addition, oxide films from several Al alloys stripped after oxidation at 1373 K showed electron diffraction patterns corresponding to $\alpha\text{-Al}_2\text{O}_3$ [8]. Moskovits [9] carried out oxidation of an Al 1200 alloy samples by exposing them to an oxygen-gas torch. He observed that initially an $\alpha\text{-Al}_2\text{O}_3$ scale formed on the surface. Subsequently, at some point in the oxidation, a rapid reaction began which produced a tree-like Al_2O_3 structure. This structure is similar to the morphology of $\text{Al}_2\text{O}_3/\text{Al}$ composites produced by directed oxidation [1].

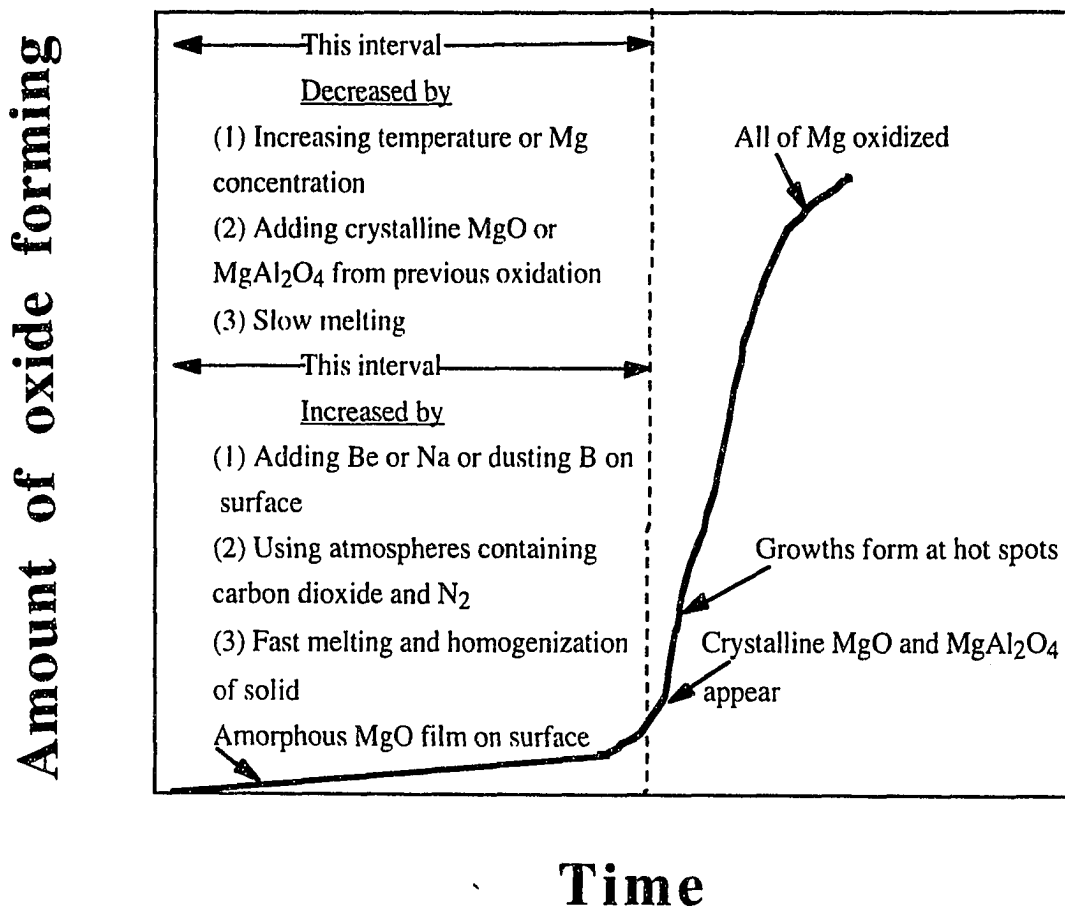


Fig. 2.1 Oxidation features of liquid Al-Mg alloys (after Cochran et al. [2]).

2.3 Directed Oxidation of Liquid Al-Mg Alloys

Newkirk et al. [1] were the first to observe that under appropriate conditions of alloy composition, temperature and oxygen pressure, a rapid reaction of liquid Al alloys with gaseous oxidants to form α - Al_2O_3 occurs, and the reaction product grows outward from the original metal surface. The resulting material was an $\text{Al}_2\text{O}_3/\text{Al}$ ceramic matrix composite. A weight gain of 80% was observed in complete conversion of the aluminum in the alloy to alumina [1]. Practical Al_2O_3 formation rates of 2.5-3.8 cm in 24 hours were reported [11]. These observations were based on oxidation studies of Al-Mg-Si alloys (0-10 wt% Mg, 0-10 wt% Si) in the temperature range of 1400-1700 K [1]. According to Newkirk et al. [1-11], alloying elements with high vapor pressure like Mg, Zn along with group IVB elements like Si, Ge, Pb etc. were necessary for directed oxidation to take place. Dopants like Mg, Zn etc. are believed to hinder the formation of a protective alumina film on the surface and thus allow continued oxidation of the aluminum alloy. These dopants could either be applied to the surface of the aluminum exposed to the oxidant or alloyed with the parent metal. As shown in Fig. 1.2, the overall sequence of directed oxidation consists of an initial oxidation event of rapid weight gain, followed by an incubation period of relatively no weight gain. Subsequently, bulk aluminum oxidation to alumina in the growth stage begins with a substantial increase in the oxidation rate. The mechanism of oxidation in the various stages of directed oxidation are discussed in the following sections.

2.4 Mechanism of Oxidation in the Initial Stage

2.4.1 Initial Heating in Air

In the case of heating of Al-Mg alloys in air to the test temperature, the weight gain in the initial stage is believed to correspond to the formation of MgAl_2O_4 spinel [12]. The initial formation of MgAl_2O_4 spinel was explained on the basis of Al-Mg-O thermodynamics by Salas et al. [13]. Figure 2.2 shows the stability of various phases in the Al-Mg-O system. It can be seen from Fig. 2.2 that when Al-Mg alloys (typical composition of 2-5 wt % Mg [12]) are heated to the oxidation temperature (1273-1673 K [12]), MgAl_2O_4 spinel would be the stable phase in contact with the Al-Mg melt and hence would be expected to form. In the melt, the oxygen activity is, therefore, established by the Al-Mg/ MgAl_2O_4 equilibrium, and is small (10^{-34} atm at 1373 K for an Al - 5wt % Mg alloy) [13]. The large difference in the oxygen activity in the external atmosphere (0.21 atm) and in the alloy melt leads to the establishment of an oxygen potential gradient. Since Mg^{+2} diffuses faster than Al^{+3} through the spinel layer, the spinel subsequently demixes to form MgO on the surface in presence of the oxygen gradient [12]. Thus, at the end of the initial stage, a dark MgO covered MgAl_2O_4 layer is observed on the top surface of the melt [12-15].

2.4.2 Initial Heating in Argon

On heating Al-Mg alloys to the oxidation temperature in argon, formation of MgO results on introduction of oxygen [16-17]. Since MgO is not stable in contact with the melt for the alloy compositions used in directed oxidation (Fig. 2.2), the stable MgAl_2O_4 spinel phase subsequently evolves between the MgO and the liquid alloy layers [17]. Thus the microstructure at the end of the initial stage is comprised of a MgO covered MgAl_2O_4 layer on the top surface of the melt and is similar to that observed during heating in air [17].

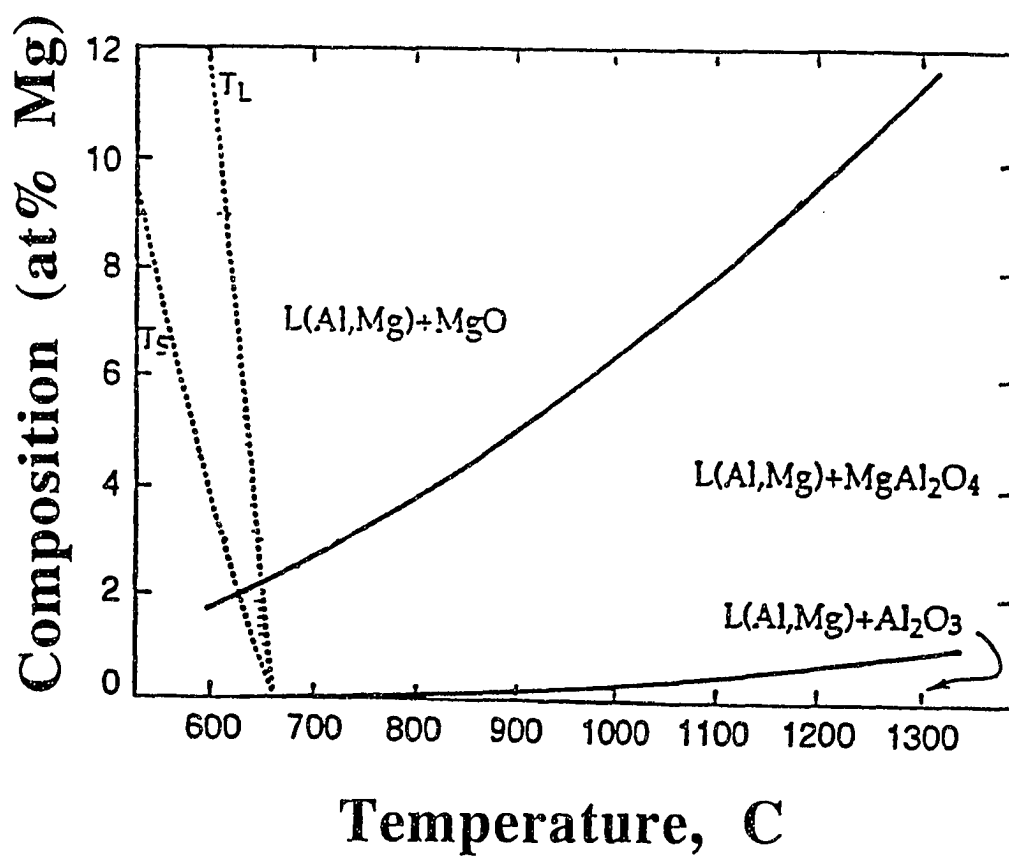


Fig. 2.2 Estimated phase diagram showing the stability of various phases in the Al-Mg-O system [17]. Also shown are the liquidus (T_L) and the solidus (T_S) lines.

However, the MgO layer is white in color [16] unlike the dark MgO layer obtained during heating in air.

Vlach et al. [17] suggested that the formation of MgO in the initial stage of oxidation of Al-Mg alloys occurs by reaction enhanced, gaseous diffusion limited, vaporization of Mg followed by its oxidation. However, no experimental evidence was presented to corroborate the suggested mechanism. They [17] also suggested that the initial stage of oxidation ends when a dense layer of spinel forms on the surface of the melt and prevents further vaporization of magnesium. However, no explanation for the sudden formation of spinel, leading to the sharp decrease in rate at the end of the initial stage of oxidation, was presented.

Though models for the reaction enhanced vaporization of pure metals are available in literature [18-19], the vaporization of alloys in a reactive atmosphere has not been studied. Turkdogan et al. [18] and Wagner [19] showed that the rate of vaporization of pure metals was independent of the vapor pressure of the metal but dependent on the partial pressure of the reactive gas. In their study, the vapor pressures of metals were significantly lower than the partial pressure of the reactive gas, oxygen. This is not the case in the directed oxidation of Al-Mg alloys, since the vapor pressure of Mg is comparable to the oxygen partial pressures typically utilized in the oxidation of the Al-Mg alloys. Furthermore, unlike the vapor pressure of a pure metal, the vapor pressure of magnesium over the Al-Mg alloy decreases continuously with time as vaporization proceeds owing to the depletion of magnesium from the alloy. Hence, the models for vaporization of pure metals in a reactive atmosphere [18-19] cannot be used to test the hypothesis of Vlach et al. [17], on the mechanism of the initial stage of directed oxidation. Therefore, to understand the role of vapor phase oxidation of magnesium in oxygen atmosphere in the initial stage of directed oxidation, the reaction enhanced vaporization of Mg into the gas phase must be coupled

with the loss of magnesium from the alloy to accurately calculate the rate of Mg vaporization.

2.5 Incubation

2.5.1 Mechanism of Oxidation During Incubation

In the case of initial heating in argon, formation of a thin layer (2 μm) of MgAl_2O_4 spinel corresponds to the end of the initial stage and the onset of incubation [17]. During incubation, metal channels are observed to form in the spinel [12,17]. The sequence of events in channel formation, as envisaged by Salas et al. [13], is illustrated in Fig. 2.3. A small lens-shaped spinel nucleus forms at the interface between the MgO surface layer and the alloy, Fig. 2.3(a). Since MgO is unstable in presence of the Al alloy, the MgAl_2O_4 spinel precipitates according to the following reaction [13]:



wherein the excess Mg from reaction (2.1) migrates to the surface to react with atmospheric O_2 and form more MgO. Spinel formation by reaction (2.2) is most favorable near the three-phase junction, where the diffusional distances for (O) are shortest. Thus, the spinel nucleus would tend to spread along the melt/MgO interface, as shown in Fig. 2.3 (b). However, any significant growth must be accompanied by upward recession of the MgO/melt interface as the excess Mg migrates to the surface and regenerates most of the MgO. Since four moles of MgO are converted to one mole of MgAl_2O_4 , the latter accounts for only $\approx 88\%$ of the dissolved oxide volume. This volume change associated with the

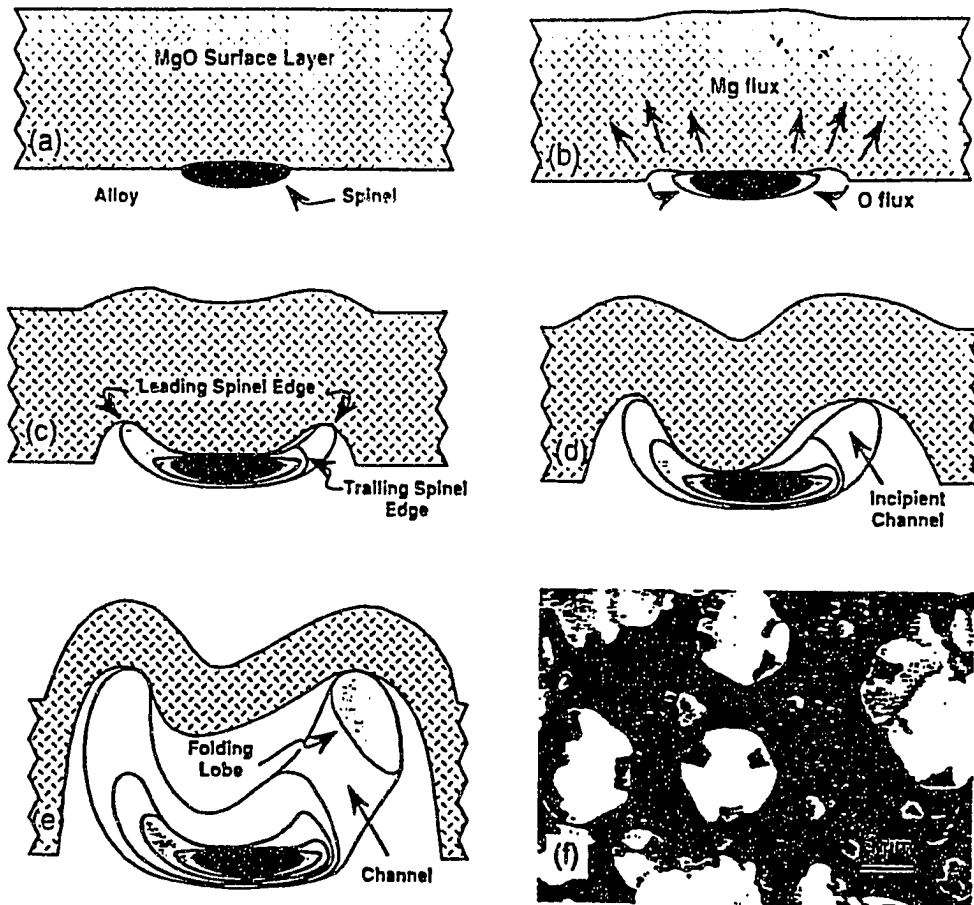


Fig. 2.3 Schematic of possible mechanism leading to channel initiation within oxide buds at the start of incubation [13].

oxide conversion leads to an opening gap between the receding MgO and the advancing spinel which is filled by the underlying melt. As the (O) source moves forward, it is followed by the leading edge of the spinel, imparting a concave shape to the evolving bud (Figs. 2.3(c-e)). Eventually the advancing spinel front cannot maintain its circular profile and breaks down due to morphological instability (Fig. 2.3f) [13]. This instability is likely to be linked to the diffusional constraints associated with the growth process. The interfacial breakdown extends the MgO/Al-melt contact and hence the favorable area for MgO dissolution and MgAl₂O₄ precipitation. The lobes developed in the spinel edge continue their upward growth but gradually turn inward and fold upon themselves, creating a channel, as illustrated in Fig. 2.3(e) [13]. Thus, the microstructure at the end of incubation consists of an MgO layer on the top surface, separated from the bulk metal by a MgAl₂O₄ layer containing metal channels [12-17]. As shown in Fig. 1.2, the weight gain rates during incubation are quite low. Thickening of the MgAl₂O₄ layer by cation diffusion accounts for most of the weight gain in this period [17].

2.5.2 Duration of Incubation

Growth stage starts and incubation ends with the formation of discrete spinel nodules at the points where individual metal channels pierce through the dense spinel and reach the MgO/MgAl₂O₄ interface [13]. The duration of incubation is associated with the time required for a significant number of metal channels to undergo this process. According to Salas et al. [13], the time required for this process is controlled by the activity of Mg in the metal channels. It has been observed that increasing oxidation temperatures decrease the period of incubation [1,11,17]. It has also been noted that Si additions reduced the incubation period [15,17]. Vlach et al. [17] suggested that silicon could accelerate the microchannels in the spinel towards the spinel/MgO interface, and thus, reduce incubation. According to Salas et

al. [13], Si could reduce the activity of Mg in the Al melt, and thereby enhance spinel dissolution which would curtail incubation. Thus, the role of oxidation temperature, and silicon in the melt on the duration of incubation is not clearly understood. Control of the spinel layer morphology may be crucial for controlling metal channel distribution which, in turn, would control subsequent oxide growth.

2.6 Growth Stage of Directed Oxidation

2.6.1 Initiation of Alumina Formation

Since MgO is unstable for the typical Al alloy compositions used in directed oxidation (Fig. 2.2), MgO dissociates in presence of the Al alloy and the stable MgAl_2O_4 phase precipitates. Since the $[\text{Mg}]/[\text{Al}]$ ratio in the alloy is much lower than that required by the stoichiometry of the spinel, the Mg content in the melt decreases as the spinel nodules grow. Eventually, the Mg concentration in the near surface alloy drops to a value at which Al_2O_3 becomes more favorable than MgAl_2O_4 and, epitaxial nucleation of Al_2O_3 on MgAl_2O_4 takes place [12-14]. Thus, during bulk oxide growth, the surface microstructure consists of a MgO layer (thickness 1 to 4 μm [14]) on top of the alumina matrix with a thin Al alloy film separating the two layers (Fig. 2.4) [14].

2.6.2 Mechanism of Alumina Formation

Several models have been proposed to explain the kinetics of oxidation of Al to Al_2O_3 in the growth stage. All of the proposed models are based on the premise that during the growth stage of directed oxidation of Al-Mg alloys, a continuous MgO film exists at the top of the alumina matrix with a thin aluminum alloy film (0.1-3 μm) separating the two layers [12,14] (Figs. 2.4, 1.2). At the MgO/Al-alloy film interface, MgO dissociates and



Fig. 2.4 Microstructure of the composite growth front illustrating the MgO/metal/ Al_2O_3 layered structure [20].

oxygen dissolves in the Al-alloy film. The magnesium ions formed by dissociation of MgO diffuse through the MgO layer to the MgO/air interface where they are oxidized to regenerate MgO. During the outward transport of magnesium ions through MgO, electrical neutrality is maintained by the parallel transport of electronic defects. The oxygen dissolved in the alloy film in contact with the MgO layer is transported to the alloy film/alumina interface where composite growth takes place. The supply of aluminum to the alloy film/alumina interface is thought to be sustained by the wicking of metal through channels in the alumina. One or more of the above mentioned reaction steps could be the rate controlling mechanism in the growth stage.

Vlach et al. [17] carried out directed oxidation studies of Al-Mg-Si alloys in the temperature range of 1273-1373 K and observed parabolic oxidation kinetics in the growth stage with an activation energy of 270 kJ/mole. They [17] suggested that the major rate controlling step in the growth stage was the transport of liquid Al to the near surface alloy layer through the composite channels. Xiao et al. [21] carried out directed oxidation experiments of pure aluminum to which MgO powder was added. They observed that the growth rate was parabolic with an activation energy of 260 kJ/mole. It was suggested that oxygen required for aluminum oxidation was provided by dissociation of MgO, with the MgO being regenerated by vapor phase oxidation.

Nagelberg et al. [20] studied the growth kinetics of an Al₂O₃/metal composite from an Al-10 wt% Si-3 wt % Mg alloy in the temperature range of 1398-1548 K. The growth rate of these alloys was constant, proportional to $P_{O_2}^{1/4}$, where P_{O_2} is the partial pressure of oxygen, and had an activation energy of 310 kJ/mole (Fig. 2.5). It was proposed by Nagelberg et al. [20] that the rate of oxidation of Al-Mg-Si alloys in the growth stage was controlled by the electronic conductivity of the continuous external MgO layer. Khatri et al.

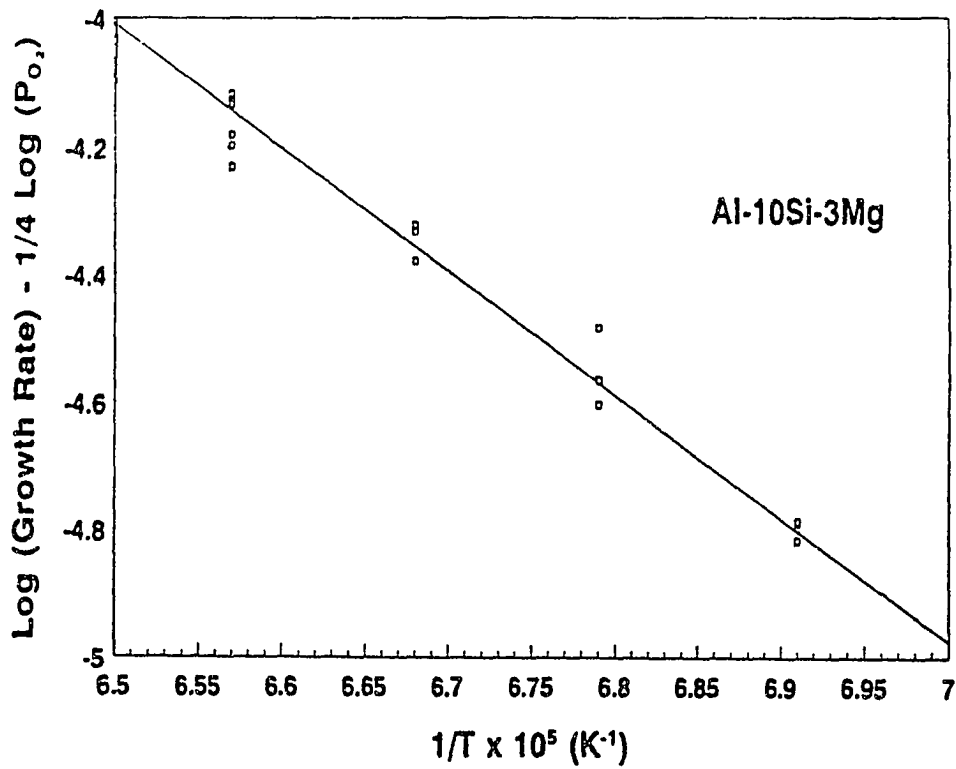


Fig. 2.5 Plot of growth rate data of Al-10 wt% Si-3 wt% Mg alloys. Data set shows consistency with both an activation energy of 370 kJ/mole and oxygen partial pressure dependence of $P_{\text{O}_2}^{1/4}$ [20].

[22] conducted oxidation studies of Al-Mg alloys with varying silicon contents [22]. They concluded that the growth rate for the Al-5 wt% Mg-5 wt% Si alloy at 1573 K was controlled by electronic transport through the outer MgO layer. According to Khatri et al. [22], at 1573 K, silicon back-diffusion through the metal channels to the bulk alloy controlled the growth rate of the Al alloy with the higher silicon content (Al-5 wt% Mg-10 wt% Si). Nagelberg also investigated the growth kinetics from an Al-Zn-Si alloy [23]. He observed that the growth rate decreased with time, was independent of oxygen pressure, and had an activation energy of 90 kJ/mole. The growth rate data was consistent with the electronic transport behavior of a n-type surface oxide layer such as ZnO [23]. To investigate the role of electronic transport in the oxidation kinetics in the growth stage, DebRoy et al. [16] carried out directed oxidation experiments of a Al-5 wt% Mg alloy (Al-5056 alloy) in which platinum wires were positioned inside the alloy so that the wires would extend through the composite matrix to the MgO layer at the top surface and facilitate electronic transport. They [16] observed that the rate of oxidation in the growth stage was independent of the presence or absence of Pt wires (Fig. 2.6) indicating that the transport of electronic species does not control the oxidation kinetics, in the growth stage, of Al-Mg alloys containing no silicon. Thus, in the absence of silicon, electronic transport through the MgO layer is no longer the rate controlling mechanism in the growth stage of Al-Mg alloys. In view of the crucial difference in the oxidation mechanism of Al-Mg alloys with or without the presence of Si, the role of silicon on the mechanism of composite growth from Al-Mg alloys needs to be investigated in detail.

2.6.3 Composite Microstructure at the End of the Growth Stage

According to Breval et al. [24], the bulk of the Al₂O₃/Al composite consists of interpenetrating networks of Al₂O₃ and Al arranged in a macrostructure of columnar cells

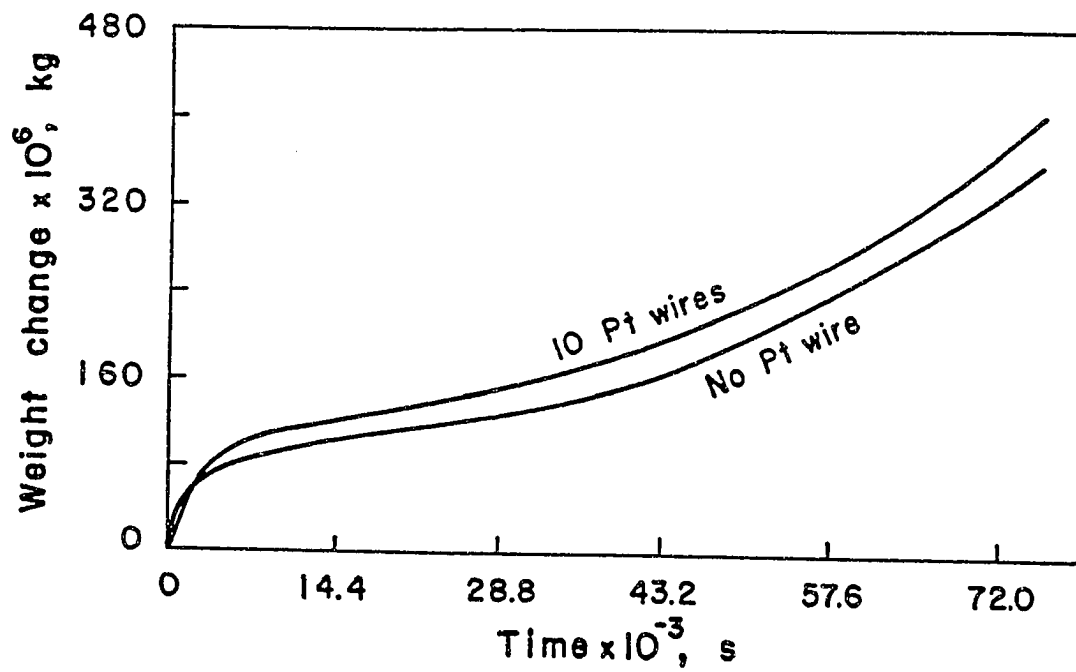


Fig. 2.6 Plot of growth rate data of Al-5 wt% Mg alloys, with and without Pt wires [16].

(up to several millimeters wide) that grow outward from the molten alloy surface. The metal microchannels are typically 1 to 10 μm in diameter [12]. The orientation of the Al_2O_3 changes slightly from cell to cell and the growth direction is almost parallel to the c-axis of the Al_2O_3 structure [1,12,24]. The alumina exhibits the same crystallographic orientation over hundreds of microns [12] which indicates that Al_2O_3 growth takes place epitaxially. The majority of the domains within the cells are separated by low angle boundaries which are free of intergranular phases (Fig. 2.7) [1]. High angle grain intersections were found to typically contain thin channels of metal separating neighboring Al_2O_3 crystals rather than a high angle $\text{Al}_2\text{O}_3/\text{Al}_2\text{O}_3$ grain boundary (Fig. 2.7) [1]. The presence of narrow channels of alloy in selected microscopic sections in the oxide composite has been presented as “evidence” of the wicking process [24]. However, the observation of a few alloy channels in arbitrarily selected microscopic sections does not really constitute a rigorous proof that the narrow metal channels extend from the bulk liquid metal at the bottom all the way through the ceramic oxide matrix to the top surface.

The relative proportions of the various phases in the composite microstructure was analyzed by Breval et al. [24]. Their results (Table 2.1) demonstrate that the bulk material was predominantly Al_2O_3 . A layer of MgAl_2O_4 spinel was found at the bottom of the composite, and both regions contained a metallic phase which was primarily Al [24]. Several investigators have measured the Mg concentration in the metal channels [20,21,25] and found it to correspond to the Al alloy/ $\text{Al}_2\text{O}_3/\text{MgAl}_2\text{O}_4$ equilibrium at the reaction temperature.

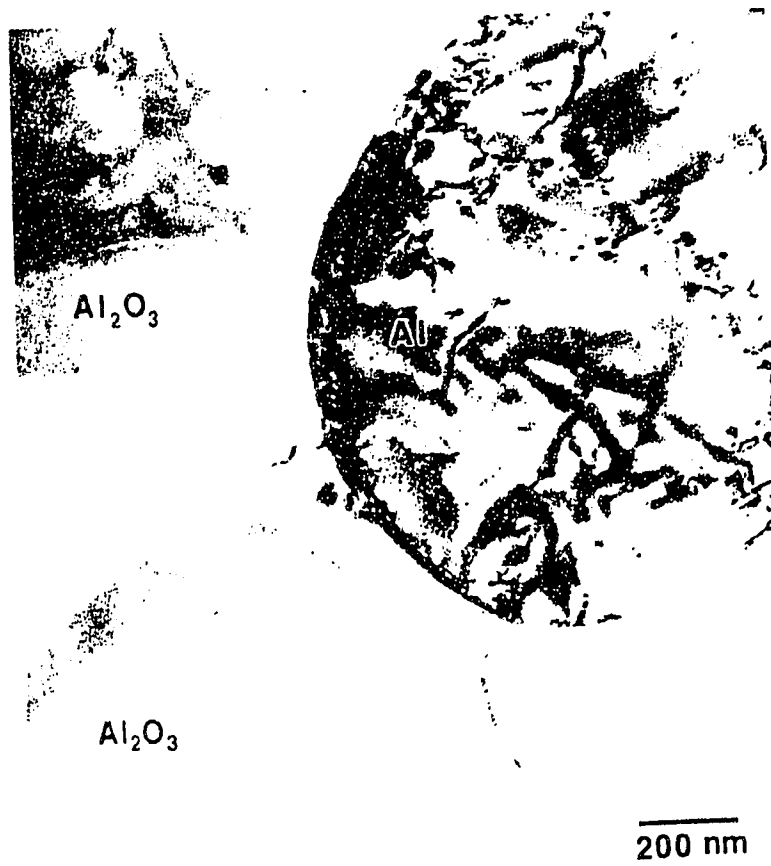


Fig. 2.7 Bright field TEM micrograph showing a low-angle Al₂O₃-Al₂O₃ grain boundary and a high-angle Al-Al₂O₃ boundary in Al₂O₃/Al composite produced by directed oxidation [28].

Table 2.1 Relative proportions of various phases in the bulk and bottom of the $\text{Al}_2\text{O}_3/\text{Al}$ composite, produced by directed oxidation of Al-2.5 Mg alloy [24].

Location	Metal, vol %	Al_2O_3 , vol %	MgAl_2O_4 , vol %
Bulk	19	75	1
Bottom	13	19	68

2.6.4 Effect of Composite Microstructure on the Mechanical Properties of Al₂O₃/Al Composites

It has been recognized that the toughness of ceramic matrix composites containing ductile phases is controlled by the volume fraction and interconnection of the ductile phase [26,27]. Aghajanian et al. [28] measured the mechanical properties of Al₂O₃/Al composites grown by directed melt oxidation of aluminum alloys. They observed that the flexural strength of Al₂O₃/Al composites increased with increase in the volume fraction and interconnection of Al metal channels [28] (Table 2.2). It was also found that the critical strain energy release rate, which is a measure of toughness, was the highest for the composite which contained the largest amount of interconnected Al channels [28] (Table 2.2). Thus, it is clearly seen that the metal distribution in Al₂O₃/Al composites needs to be tailored to ensure maximum enhancements in toughness.

Very little information is available in the literature on the procedure to tailor the metal content of Al₂O₃/Al composites prepared by directed oxidation. A notable exception is the investigation of Manor et al. [29] who measured the volume fraction of Al in Al₂O₃/Al composites, grown by directed oxidation of a complex Al-Zn-Mg-Si-Cu-Fe alloy at various temperatures. They observed that the volume fraction of Al in the Al₂O₃/Al composites decreased with increasing growth temperature. However, the reason for the observed dependence of the amount of metal in the composite on the growth temperature is not clearly understood. The dependence of metal interconnection in Al₂O₃/Al composites on the growth temperature has not been investigated. In addition to controlling the toughness of Al₂O₃/Al composites, the interconnection of Al metal is the basis for liquid metal transport in the growth stage by wicking to occur.

Table 2.2 Effect of metal volume fraction and interconnectivity on flexural strength and toughness of Al₂O₃/Al composite [28].

Metal volume fraction in composite, vol %	Number of dimensions in which Al is continuous	Flexural strength, MPa	G _{1c} , J/m ²
22	3	350	350
3	0	46	92
13	0	250	110

Thus, the dependence of Al metal volume fraction and Al interconnection in $\text{Al}_2\text{O}_3/\text{Al}$ composites on growth temperature needs to be investigated.

2.7 Effect of Process Parameters on Directed Oxidation

2.7.1 Effect of Alloy Composition

Newkirk et al. [1] observed that the presence of both Mg and Si was required for accelerated oxide growth from Al-Mg-Si alloys. Nagelberg [15] investigated the role of Mg and Si in the directed oxidation of Al-Mg-Si alloys. He observed that composite growth occurred only for the ternary Al-Mg-Si alloy. To initiate composite growth from binary Al-Mg alloys, mechanical disruption of the surface oxide was required. Xiao et al. [21] conducted directed oxidation studies of pure Al covered with MgO powder. They [21] observed that composite growth in the directed oxidation of Al-Mg alloys could be initiated without mechanical disruption of the surface oxide scale, which is consistent with the observations of DebRoy et al. [16]. It was observed [30] that the addition of transition metals (Ni, Fe) to aluminum alloys refines the microstructure. These additions also enhance the growth rate. However, the reason for the microstructural refinement and growth rate enhancement is not understood.

2.7.2 Effect of Temperature

Newkirk et al. [1] observed that composite growth was confined to temperatures in the range of 1370 K to 1670 K in the Al-Mg-Si system. It was noted by Vlach et al. [17] that Al_2O_3 formation occurred only in the temperature range of 1273 K - 1623 K. For continued oxidation of the Al alloy, formation of the protective Al_2O_3 film on the surface must be avoided. In the case of Al-Mg alloys, formation of the continuous MgO layer on the surface ensures composite formation. Since the Mg vapor pressure over the melt

decreases exponentially with temperature, formation of the continuous MgO layer might not be feasible at low temperatures. This would curtail Al_2O_3 formation. At high processing temperatures, Mg loss during initial heating might be appreciable enough to prevent formation of an MgO layer, and thus, prevent composite formation.

2.8 Directed Oxidation into Al_2O_3 Preforms

2.8.1 Microstructure

Breval et al. [29] examined the structure of $\text{Al}_2\text{O}_3/\text{Al}$ composite produced by directed oxidation of an Al alloy into Al_2O_3 preforms. They observed that the preform refines the alumina grain size and the size of the metal regions. The preform also lead to a more randomly oriented Al_2O_3 unlike the preferred orientation [1,11,23] ([0001] axis of Al_2O_3 parallel to the growth direction) obtained in the absence of an Al_2O_3 preform. Even though the preform effectively disrupted the columnar matrix Al_2O_3 structure, the MgO layer on the top surface of the composite was retained [28]. In addition, the presence of a thin metal layer beneath the MgO layer was also observed.

2.8.2 Growth Kinetics

Watari et al. [37] investigated the growth of $\text{Al}_2\text{O}_3/\text{Al}$ composites into Al_2O_3 preforms. They measured the thickness of the composite as a function of oxidation time and temperature. It was observed that the thickness of the $\text{Al}_2\text{O}_3/\text{Al}$ composite increased at a constant rate with time at 1473 K. At 1523 K, the thickness increased as a parabolic function of time, and was proportional to the square root of the pore size. However, no explanation was advanced for the observed change in the thickness dependence. Nagelberg [32] observed that the growth rate of aluminum alloys into Al_2O_3 preforms initially increased rapidly to a maximum value and subsequently decreased as matrix growth

proceeded through the preform. Upadhyaya et al. [34] observed that the growth rate of Al-2.5 wt% Mg alloy into Al_2O_3 preforms increased with decreasing Al_2O_3 particle size. However, the growth rate was not found to be proportional to the surface area of the Al_2O_3 particle. It is clear from these experimental observations that while Al_2O_3 preforms can provide sites for the epitaxial nucleation of fresh Al_2O_3 , the loose preform can also provide a tortuous path for metal wicking to the growth surface and, thus, limit liquid metal transport. Thus, the effect of preform particle size on the interplay between secondary nucleation and liquid metal transport, and their effects on the composite growth rate, need to be addressed.

2.9 Summary

Although synthesis of ceramic matrix composites by the directed oxidation process offers significant advantages over traditional composite processing routes, the scientific basis for the process is not fully understood. However, it is generally recognized that three distinct stages can be observed in the directed oxidation of Al-Mg alloys. An initial stage of rapid weight gain is followed by incubation which is a period of little weight gain. The end of incubation and the onset of the growth stage corresponds to an increase in the weight gain rate. During growth, bulk oxidation of Al to Al_2O_3 occurs. In the growth stage, an MgO layer is observed on the top surface and is separated from the Al_2O_3 by a thin alloy layer.

On heating of Al-Mg alloys in argon, MgO forms in the initial stage on introduction of oxygen. The amount of MgO formed determines the residual Mg content in the alloy. The onset of alumina formation in the growth stage corresponds to the time required to reduce the Mg composition in the alloy to that at which Al_2O_3 is in equilibrium with the Al-Mg alloy. Thus, it is clear that the amount of MgO which forms in the initial stage and the mechanism of initial stage oxidation are important. It has been claimed that MgO formation

occurs by reaction enhanced vaporization of Mg followed by oxidation of Mg vapor. However, the rationale for justifying this mechanism for initial stage oxidation is not known.

Kinetics of formation of Al_2O_3 in the growth stage has been studied by several investigators. It has been suggested that electronic transport through the outer MgO layer controls the growth rate of Al-Mg-Si alloys. It has also been observed that in the absence of silicon, the mechanism of growth is altered and, electronic transport does not control the growth rate. In view of the crucial difference in the oxidation mechanism of Al-Mg alloys with or without the presence of Si, the role of silicon on the mechanism of composite growth from Al-Mg alloys needs to be investigated in detail.

The poor toughness of ceramics has been a significant deterrent in their use for structural applications. The toughness of $\text{Al}_2\text{O}_3/\text{Al}$ composites is determined by the amount and distribution of the ductile toughening phase, aluminum. However, the dependence of Al distribution in $\text{Al}_2\text{O}_3/\text{Al}$ composites on reaction parameters is not known. Furthermore, an investigation of metal distribution in the composite could provide evidence for metal transport by capillarity (wicking).

The practical utilization of directed melt oxidation is greatly facilitated by the ability to grow the oxidation product of the melt into porous preforms (e.g. Al_2O_3). Analysis of the data reported in literature indicate that Al_2O_3 preforms could provide sites for the epitaxial nucleation of fresh Al_2O_3 and, at the same time, limit liquid metal transport. Thus, the effect of preform particle size on the interplay between secondary nucleation and liquid metal transport, and their effects on the composite growth rate, need to be clearly delineated.

2.10 References

1. M. S. Newkirk, A. W. Urquhart, H.R. Zwicker and E. Breval, "Formation of Lanxide™ Ceramic Composite Materials," *J. Mater. Res.*, **8** [7-8] 879 (1987).
2. C. N. Cochran, D. L. Belitskus and D. L. Kinosz, "Oxidation of Aluminum-Magnesium Melts in Air, Oxygen, Flue Gas, and Carbon Dioxide," *Metall. Trans B.*, **8B** 323-32 (1977).
3. D. L. Belitskus, "Oxidation of Molten Al-Mg Alloy in Air, Air-SO₂, and Air-H₂S Atmospheres," *Oxid. Metals*, **3** [4] 313-17 (1971).
4. M. Drouzy and C. Masacre, "The Oxidation of Liquid Non-Ferrous Metals in Air or Oxygen," *Met. Rev.*, 131 25-46 (1969).
5. M. Drouzy and M. D. Fontaine, "Oxydation de L'aluminium et des alliages Aluminium-Magnesium Liquids," *Revue de Metallurgie*, 771-81 (1970).
6. L. Brouckere, "An Electron Diffraction Study of the Atmospheric Oxidation of Al, Mg and Al-Mg Alloys," *J. Inst. Met.*, **71** 131-47 (1945).
7. G. Wightman and D. J. Fray, "The Dynamic Oxidation of Aluminum and Its Alloys," *Met. Trans. B*, **14B** 625-31 (1983).
8. M. V. Maltsev, Y. D. Chistiakov and M. I. Tsypin, "Electron Diffraction Investigation of Oxide Films Forming on Molten Aluminum and Its Alloys," *Izv. Akad. Nauk. SSSR.*, **20** 747-50 (1956).
9. M. Moskovits, "The Kinetics of Oxidation of Molten Aluminum in Oxidant Streams," *Oxid. Met.*, **5** [1] 1-9 (1972).
10. I. Haginoya and T. Fukasako, "Oxidation of Molten Al-Mg Alloys," *Trans. Jpn. Inst. Met.*, **24** [9] 613-19 (1983).
11. M. S. Newkirk, H. D. Leshner, D. R. White, C. R. Kennedy, A. W. Urquhart, and T. D. Claar, "Ceramic Matrix Composites: Matrix Formation by the Directed Oxidation of Molten Metals," *Ceram. Eng. Sci. Proc.*, **6** [9] 1964-81 (1991).
12. O. Salas, H. Ni, V. Jayaram, K. C. Vlach, C. G. Levi and R. Mehrabian, "Nucleation and Growth of Al₂O₃/Metal Composites by Oxidation of Aluminum Alloys," *J. Mater. Res.*, **6** [9] 1964-81 (1991).

13. O. Salas, V. Jayaram, K. C. Vlach, C. G. Levi and R. Mehrabian, "Early Stages of Composite Formation by Oxidation of Liquid Aluminum Alloys," *J. Am. Ceram. Soc.*, **78** [3] 609-22 (1995).
14. S. Antolin, A. S. Nagelberg and D. K. Creber, "Formation of Al_2O_3 /Metal Composites by Directed Oxidation of Molten Aluminum-Magnesium-Silicon Alloys: Part I, Microstructural Development," *J. Am. Ceram. Soc.*, **75** [2] 447-54 (1992).
15. A. S. Nagelberg, "Observations on the Role of Mg and Si in the Directed Oxidation of Al-Mg-Si Alloys," *J. Mat. Res.*, **7** [2] 265-68 (1992).
16. T. DebRoy, A. Bandhopadhyay and R. Roy, "Oxide Matrix Composite by Directional Oxidation of a Commercial Aluminum-Magnesium Alloy," *J. Am. Ceram. Soc.*, **77** [5] 1296-1300 (1994).
17. K. C. Vlach, O. Salas, H. Ni, V. Jayaram, C. G. Levi and R. Mehrabian, "A Thermogravimetric Study of the Oxidative Growth of Al_2O_3 /Al Composites," *J. Mater. Res.*, **6** [9] 1982-95 (1991).
18. E. T. Turkdogan, P. Grievson and L. S. Darken, "Enhancement of Diffusion-Limited Rates of Vaporization of Metals," *J. Phys. Chem.*, **67** 1647-54 (1963).
19. C. Wagner, "Passivity and Inhibition During the Oxidation of Metals at Elevated Temperatures," *Corr. Sci.*, **5** 751-64 (1965).
20. A. S. Nagelberg, S. Antolin, and A. W. Urquhart, "Formation of Al_2O_3 /Metal Composites by Directed Oxidation of Molten Aluminum-Magnesium-Silicon Alloys: Part II, Growth Kinetics," *J. Am. Ceram. Soc.*, **75** [2] 455-62 (1992).
21. P. Xiao and B. Derby, "Alumina/Aluminum Composites Formed by the Directed Oxidation of Aluminum Using Magnesia as a Surface Dopant," *J. Am. Ceram. Soc.*, **77** [7] 1761-70 (1994).
22. S. C. Khatri, M. J. Koczak, T. Chou and Y. Kagawa, "Theoretical and Experimental Analysis of Al_2O_3 /Al-Si Composites Processed from Al-Si-Zn and Al-Si-Mg by Direct Metal Oxidation," *Ceram. Eng. Sci. Proc.*, 485-93 (1992).
23. A. S. Nagelberg, "Growth Kinetics of Al_2O_3 /Metal Composites From a Complex Aluminum Alloy," *Solid State Ionics*, **32/33** 783-88 (1989).

24. E. Breval, M. K. Aghajanian and S. J. Luszcz, "Microstructure and Composition of Alumina/Aluminum Composites Made by Directed Oxidation of Aluminum," *J. Am. Ceram. Soc.*, **73** [9] 2610-14 (1990).
25. M. Sindel, N. A. Travitsky and N. Claussen, "Influence of Magnesium-Aluminum Spinel on the Directed Oxidation of Molten Aluminum Alloys," *J. Am. Ceram. Soc.*, **73** [9] 2615-18 (1990).
26. C. A. Andersson and M. K. Aghajanian, "The Fracture Toughening Mechanism of Ceramic Composites Containing Adherent Ductile Metal Phases," *Ceram. Eng. Sci. Proc.*, **9** [7-8] 621-26 (1988).
27. L. Sigl, P. Matago, B. J. Dalgleish, R. M. Mcneeking and A. G. Evans, "On the Toughness of Brittle Materials Reinforced with a Ductile Phase," *Acta Metall.*, **36** [4] 945-53 (1988).
28. M. K. Aghajanian, N. H. Macmillan, C. R. Kennedy, S. J. Luszcz and R. Roy, "Properties and Microstructure of Lanxide® Al₂O₃- Al Ceramic Composite Materials," *J. Mat. Sci.*, **24** 658-70 (1989).
29. E. Manor, H. Ni, C. G. Levi and R. Mehrabian, "Microstructure Evolution of SiC/Al₂O₃/Al - Alloy Composites Produced by Melt Oxidation," *J. Am. Ceram. Soc.*, **76** [7] 1777-87 (1993).
30. A. S. Nagelberg, A. S. Fareed and D. J. Landini, "Production of Ceramic Matrix Composites for Elevated Temperature Applications Using the DIMOX™ Directed Metal Oxidation Process," *Processing and Fabrication of Advanced Materials*, V. A. Ravi and T. S. Srivatsan (Eds.), TMS, 1992, pp 127-142.
31. E. Breval and A. S. Nagelberg, "Microstructure of an Al₂O₃/Al Composite Containing an Al₂O₃ Filler Material," *Mat. Res. Soc. Proc.*, **132** 93-98 (1989).
32. A. S. Nagelberg, "The Effect of Processing Parameters on the Growth Rate and Microstructure of Al₂O₃/Metal Matrix Composites," *Mater. Res. Soc. Symp. Proc.*, **155**, 275-282 (1989).
33. T. Watari, K. Mori, T. Torikai, and O. Matsuda, "Growth of Alumina/Metal Composites into Porous Ceramics by the Oxidation of Aluminum," *J. Am. Ceram. Soc.*, **77** [10] 2599-602 (1994).

34. D. D. Upadhyaya, R. Bhat, S. Ramanathan and S. K. Roy, "Effect of Filler Phase Porosity on Directed Oxidation of Al Alloy," *Journal of Alloys and Compounds*, **205** 275-79 (1994).

CHAPTER 3

PROCEDURES

3.1 Description of the Thermogravimetric Set-up

A schematic diagram of the thermogravimetric set-up is shown in Fig. 3.1. The thermogravimetric set-up, used for studying the kinetics of directed oxidation, consisted of a Cahn model 1000 automatic recording electric balance, a high temperature silicon carbide tube furnace, and a gas flow and pressure control system. The balance had a sensitivity of 0.5 microgram and the measurement accuracy was 0.1% of the recorder range. The quartz reaction tube was of 48 mm internal diameter and had a 25 mm equi-temperature zone at the center of the furnace. The furnace was equipped with an electronic temperature controller which regulated the temperature to ± 5 K. The crucible, containing the sample, was suspended by a platinum wire from the balance and positioned within the equi-temperature zone of the furnace. The temperature of the sample was estimated with the help of a Pt/Pt-10%Rh thermocouple.

3.1.1 Pressure and Flow Control System

An Alcatel model 2033 CP+ roughing pump capable of pumping 27 cfm, and achieving a base pressure of 0.1 torr, was used. Since the TGA experiments were carried out at high temperatures, the exhaust gases were hot and caused the oil in the motor to vaporize. To prevent oil vaporization, the gases flowing out of the TGA setup were cooled by passing through a double walled tube, through which cold water was continuously recirculated. The double walled tube was connected to the motor through bellows and high vacuum components. An MKS type 253A throttle valve along with an MKS type 652 self tuning pressure controller was used to control the flow. Prior to each experiment, the

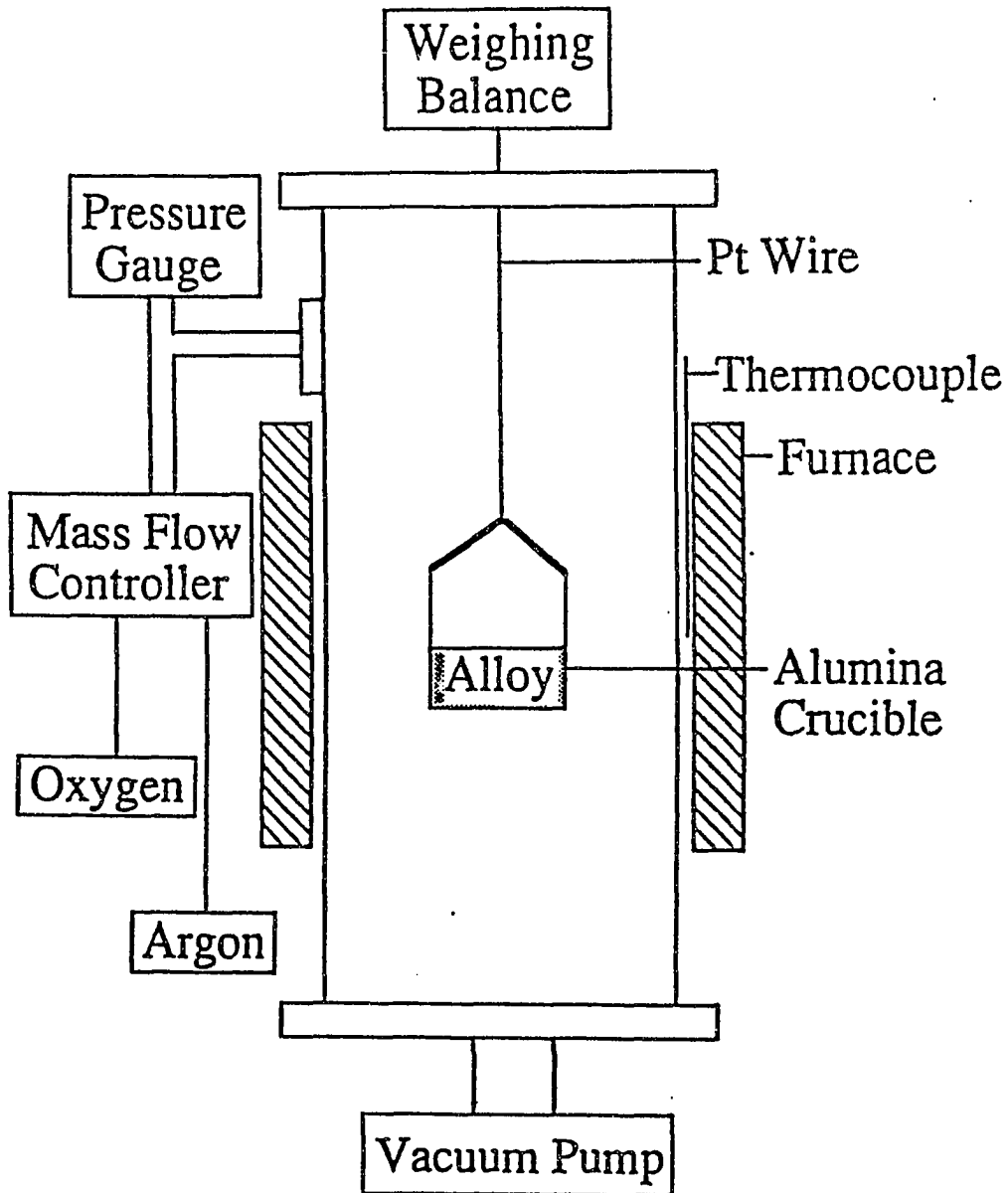


Fig. 3.1 Schematic diagram of the thermogravimetric setup.

thermogravimetric setup was evacuated and the throttle valve was closed. A leak rate of 3 torr/hr was considered adequate enough to proceed with the experiment.

The system pressure was measured down stream with the help of a MKS type 127 baratron pressure measuring unit. The baratron was connected to the pressure controller so that when the system pressure increased above the set point, the opening of the throttle valve was increased, thus reducing the pressure. The flow control system consisted of two 0-500 sccm mass flow controllers and an MKS 247C four channel power supply and readout device. These provided the capability of varying the flow rate of the individual gases and, thus, the composition of the feed gas. The mass flow controllers were calibrated with the help of a Supelco soap bubble meter.

3.2 Initial Stage

3.2.1 Experiments

A cylindrical sample, 14 mm in diameter and 8 mm in length, of an Al 5056 alloy (5 wt% Mg, 0.10 wt% Cu, 0.40 wt% Fe, 0.10 wt% Zn, 0.10 wt% Mn and balance Al) was placed in an alumina crucible, 14.2 mm in diameter and 27 mm in length. Prior to conducting each experiment, the reaction tube was evacuated and purged with argon. The samples were then heated to 1391 K, at a heating rate of 0.33 K/s, in a pure argon atmosphere. A weight loss of 1-5 milligrams is observed during initial heating in argon. When the target temperature was reached, a mixture of ultra high purity oxygen and inert gas, argon or helium, was introduced and the flow rates of oxygen and inert gas were controlled with the help of mass flow controllers to obtain a predetermined gas composition. Oxidation experiments were conducted at various partial pressures of oxygen and reactor pressures. The total gas flow rate was kept constant at 3333 mm³/s STP (298 K and 10130 Pa). Experiments were

repeated to check reproducibility of the weight gain data. A typical scatter of 1-5 % was observed in the weight gain measured during the initial oxidation. The weight of the sample was continuously recorded using a computer data acquisition system. Subsequently, the recorded data were differentiated numerically to obtain the weight gain rate. The internal cross sectional area of the crucible, 154 mm², was used for the calculation of reaction rates. The end of the initial rapid weight gain stage was considered to be the time when there was a sharp drop in the weight gain rate.

3.2.2 Modeling of Heat Transfer and Fluid Flow During the Initial Stage

The velocity, temperature and concentration fields in the gas phase during the initial stage of oxidation were computed by solving equations of conservation of momentum, enthalpy and concentration of magnesium vapor and oxygen which are represented in the following form:

$$\frac{\partial}{\partial t}(\rho\phi) + \frac{\partial}{\partial x_i}(\rho u_i \phi) = \frac{\partial}{\partial x_i}(\Gamma \frac{\partial \phi}{\partial x_i}) + S \quad (3.1)$$

where t is the time, ρ is the density, u_i is the component of velocity in the i direction, ϕ is the dependent variable which can represent velocity components, temperature or concentration, S is the volumetric source term, and Γ is the diffusion coefficient which is given an appropriate meaning depending on the variable considered. The details of the specific equations in cylindrical coordinates are described in standard textbooks [1,2] and are not presented here. The calculations were performed for a two-dimensional, unsteady, laminar flow case considering spatial variation of density and diffusion coefficient. The equations of conservation of mass, momentum and energy, represented by equation (3.1), were expressed in a finite difference form and solved iteratively on a line-by-line basis. The

details of the solution procedure are described elsewhere [2,3]. A non-uniform grid spacing was used for obtaining maximum advantage in the resolution of variables. The calculations were done for the duration of the initial stage of oxidation. The diffusion coefficient of the various species in the gas phase was calculated as shown in Appendix A. The data used for the calculations are presented in Table 3.1. The computational domain for the calculations is shown in Fig. 3.2.

The input to the model included the size and shape of the reactor and its contents, the physical properties, the rate of supply and the composition of the input gas mixture and the heating conditions. The magnesium concentration in the alloy was corrected for the initial vaporization loss. The velocity, temperature and the concentration fields of magnesium vapor and oxygen were obtained from the calculations. The boundary conditions included prescription of the input parabolic velocity distribution at the top of the reactor based on the total gas flow rate. The temperature of the inlet gas stream was prescribed to be room temperature. At the axis of the reactor, the velocity, temperature, Mg vapor and oxygen concentration gradients were taken to be zero based on the symmetry consideration. At the reactor wall, the velocities were assumed to be zero on the basis of no-slip condition and the fluxes of magnesium vapor and oxygen were taken to be zero. At the reactor wall, a temperature of 1391 K was specified in the equi-temperature zone while a measured wall temperature profile was prescribed from the inlet to the equi-temperature zone (Fig. 3.3). At the melt surface, the vapor pressure of Mg is specified as the equilibrium vapor pressure over the alloy, the oxygen concentration is set to zero, the velocities are set to zero and the temperature is specified. At the bottom outflow boundary, the velocity, temperature and concentration fields were assumed to be fully developed.

At the start of the calculations, the equilibrium vapor pressure of magnesium at the melt surface was determined from the initial alloy composition, temperature and the activity

Table 3.1 Data used in the modeling of the initial stage.

Property	Symbol	Value
Pressure	P	1.33×10^4 to 9.33×10^4 Pa
Thermal conductivity	k	4.14×10^{-2} J/(m s K)
Specific heat	C_p	520 J/(Kg K)
Viscosity	μ	4.78×10^{-5} Kg/(m s)
Diffusion coefficient	$D_{O_2 / Ar}$	$3 \times 10^{-4} (700/P) (T/1391)^{1.5}$ m ² /s
	$D_{Mg / Ar}$	$3 \times 10^{-4} (700/P) (T/1391)^{1.5}$ m ² /s
Density*	ρ	$PM/(RT)$ Kg/m ³

* M is the molecular weight of the gas mixture

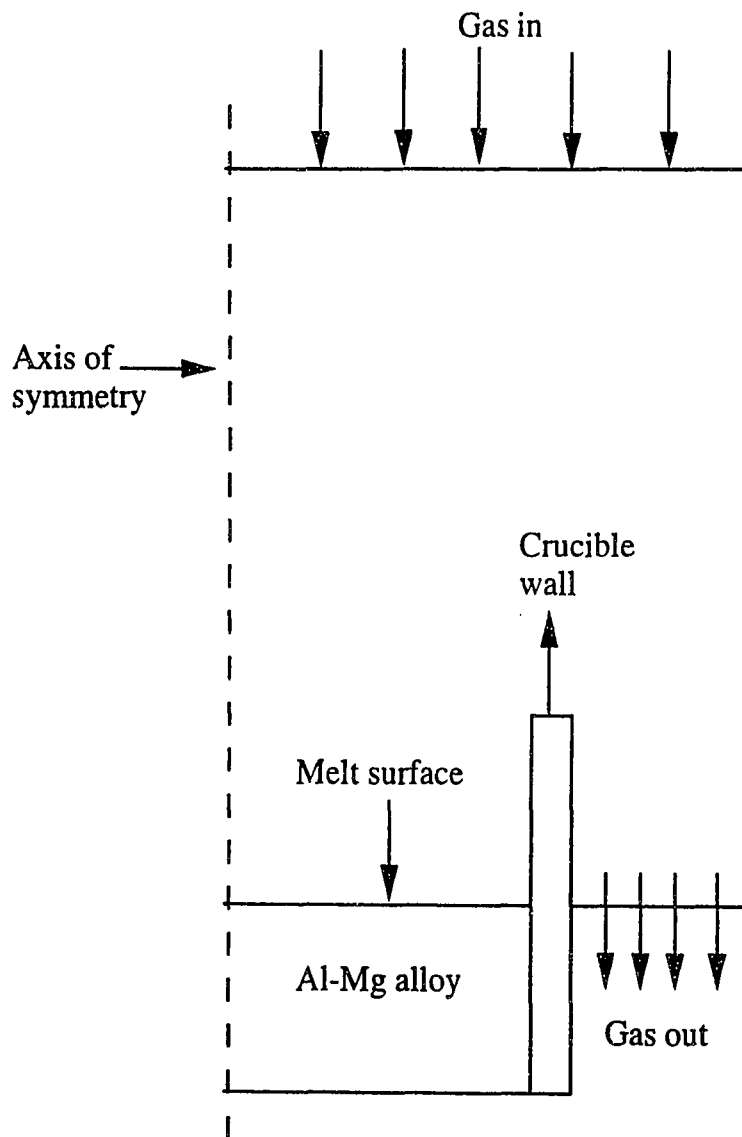


Fig. 3.2 Schematic diagram of computational domain chosen for calculation of velocity, temperature and concentration fields.

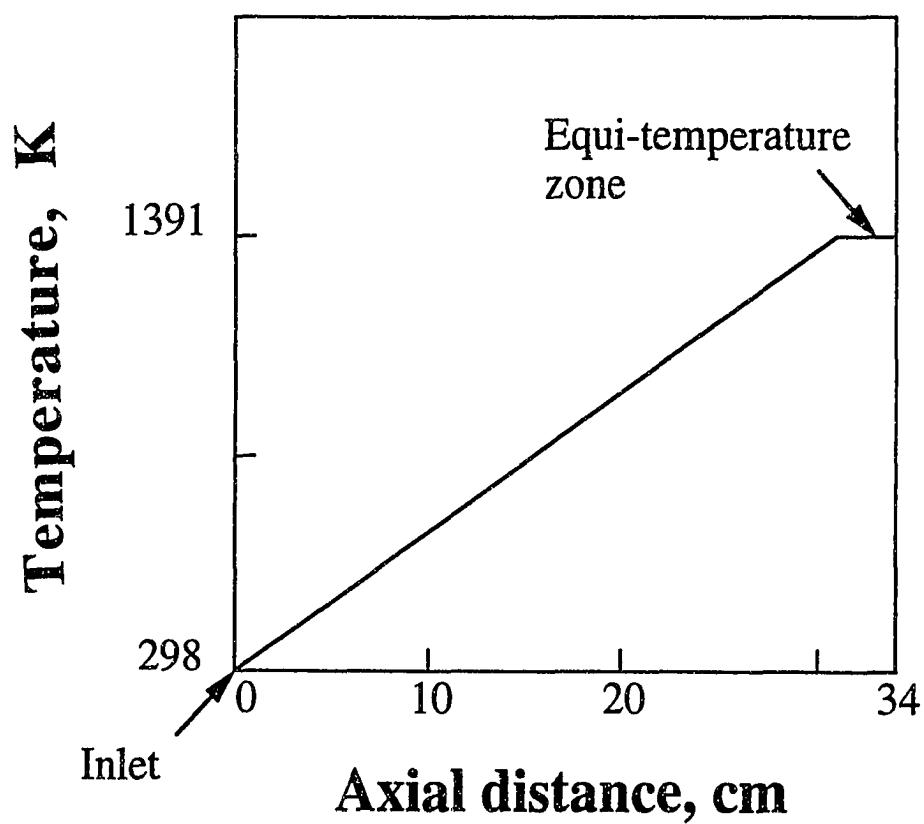


Fig. 3.3 Temperature profile along the wall of the TGA reactor.

coefficient of magnesium in the Al-Mg alloy [4, 5]. Computation of the Mg concentration field in the liquid, for the observed vaporization rates, indicates that sufficient amount of convection occurs to ensure homogenization of Mg in the liquid alloy. Therefore, the Mg concentration at the surface of the Al-Mg alloy melt is taken to be the same as that in the bulk. For this known concentration of magnesium vapor, at the alloy surface, the concentration profiles of magnesium and oxygen in the gas phase were determined. The magnesium flux from the alloy melt into the gas phase and the corresponding weight loss from the Al-Mg melt were calculated from the magnesium vapor concentration profiles. At the next time step, the vapor pressure of magnesium at the melt surface was updated based on the change in magnesium concentration in the alloy melt. Since the reaction of Mg vapor with oxygen to form MgO is rapid (Eq. 3.2), it is assumed that magnesium vapor and oxygen cannot coexist in the gas phase.



If the ratio of the number of moles of magnesium in the gas phase to the number of moles of oxygen is greater than two during any iteration, the oxygen concentration is set to zero and vice versa. It is therefore valid to assume binary diffusion coefficients for each species in the reactive atmosphere. The MgO, formed by the vapor phase reaction of oxygen and Mg vapor, falls back onto the molten alloy surface and is registered as a gain in the weight of the crucible by the automatic recording balance. The adaptation routine, used in conjunction with a general purpose computer program to solve equations of conservation of mass, momentum, and enthalpy, for predicting the velocity, temperature and concentration fields of oxygen and magnesium in the gas phase is presented in Appendix B.

3.3 Growth Stage

3.3.1 Experiments

The growth stage kinetics of Al-Mg and Al-Mg-Si alloys were studied in the TGA setup (Fig. 3.1). In some experiments, SiO₂ powder (99.9 %, -325 mesh) was added to the surface of some of the Al-5056 alloy samples, as a Si source. A previous investigation [6] on the kinetics of reaction between SiO₂ and molten aluminum revealed that SiO₂ gets completely reduced by the aluminum melt during initial heating to the test temperature (>1350 K) which takes about an hour. Thus, SiO₂ additions of 205 mg effectively result in 3.3 mol % Si in the alloy. The nominal composition of the Al-Mg and Al-Mg-Si alloys, used in this study, are shown in Table 3.2. The initial heating and the experiment start-up procedures were similar to those used for the initial stage experiments. However, higher total flow rates (8333 mm³/s STP) were used in the growth stage experiments so that the effect of widely differing oxygen pressures on the growth rate could be studied.

In the directed oxidation of binary Al-Mg alloys, the oxidation product, Al₂O₃, often grew along the crucible walls in the growth stage. The behavior is similar to the preferential growth of alumina on the crucible wall observed by Xiao et al. [7] and Manor et al. [8]. The creeping is not surprising since the MgO, which forms in the gas phase, coats the crucible walls [9]. MgO is unstable in the presence of the Al-5 wt % Mg alloy at the temperatures involved in directed oxidation [4,5,10]. Therefore, there is a net driving force for the reaction between Al and MgO. This causes Al to wet MgO [11], creep along the walls and react with oxygen in the external atmosphere to form alumina. The metal creeping leads to a change in the melt cross sectional area exposed to the oxygen atmosphere with time and complicates study of reaction kinetics. Investigation of initial stage kinetics [9]

Table 3.2 Nominal composition of the alloys used for directed oxidation experiments.

Alloy	X_{Mg} , mole %	X_{Si} , mole %
Al-Mg (Al-5056)	5.5	0
Al-Mg-Si	5.34	3.28

reveals that the higher the oxygen pressure, the lower the total amount of MgO formed in the initial stage. Hence, to minimize creeping in the directed oxidation of binary Al-Mg alloys, the oxygen pressure in the initial stage and in the incubation period was kept at a high value of 85.1 kPa, and the oxygen pressure was subsequently changed in the growth stage.

3.3.2 Estimation of Al-Mg-Si Liquid Solution Thermodynamics

As mentioned previously, the three possible rate controlling steps in the growth of $\text{Al}_2\text{O}_3/\text{Al}$ composites from Al-Mg alloys are: (i) electronic transport through the external MgO layer, (ii) transport of liquid metal by capillarity through the metal channels in the alumina, and (iii) dissociation of MgO and the subsequent transport of oxygen from the MgO/alloy film interface to the $\text{Al}_2\text{O}_3/\text{alloy}$ film interface. It is also known that in the absence of silicon, electronic transport through the MgO layer is no longer the rate controlling mechanism in the growth stage of Al-Mg alloys. Hence, the effect of silicon additions on the various rate processes must be determined. The effect of silicon additions on the rate of oxygen transport across the alloy layer can be determined by calculating the change in the oxygen solubility difference across the alloy layer. It can be seen from Fig. 3.4 that the oxygen solubility at the top of the alloy layer is determined by the Mg activity in the alloy, while the oxygen solubility at the bottom of the alloy layer is determined by the Al activity in the alloy. Si additions could alter the rate of oxygen transport by altering the Mg and Al activities in the alloy film. The effect of Si additions on the activity of Mg and Al in the liquid Al-Mg-Si alloy can be estimated from Al-Mg-Si liquid solution thermodynamics. Unfortunately, thermodynamic data on Al-Mg-Si liquid solutions are not available. On the other hand, the thermodynamics of three limiting binaries (Al-Mg, Mg-Si and Al-Si) is well understood [5,12,13]. The thermodynamics of Al-Mg-Si liquid solutions

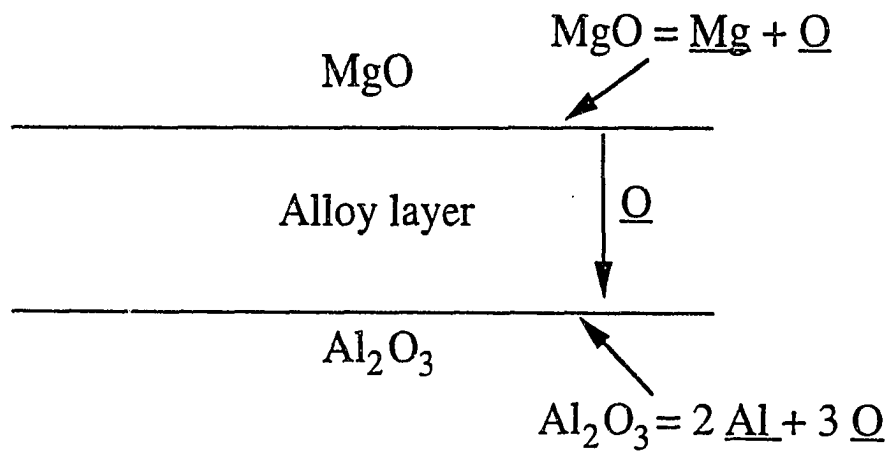


Fig. 3.4 Schematic description of the near surface aluminum alloy layer present in the growth stage of directed oxidation.

can be estimated from the three limiting binaries (Al-Mg, Mg-Si and Al-Si) using the shortest distance composition path [14]. The activity coefficient of magnesium in the Al-Mg-Si liquid solution for the composition A, is deduced from the thermodynamics of Al-Mg, at composition P, Mg-Si at composition Q and Al-Si, at composition R (Fig. 3.5) by the equation:

$$RT \ln \gamma_{Mg} = \frac{X_{Al}^A (X_{Al}^A + X_{Si}^A) \Delta \bar{G}_{Mg/Al-Mg}^{XS}}{(1 - X_{Mg}^P)^2} + \frac{X_{Si}^A (X_{Al}^A + X_{Si}^A) \Delta \bar{G}_{Mg/Mg-Si}^{XS}}{(1 - X_{Mg}^Q)^2} - \frac{X_{Al}^A X_{Si}^A \Delta G_{m/Al-Si}^{XS}}{X_{Al}^R X_{Si}^R} \quad (3.3)$$

where γ_{Mg} denotes the activity coefficient of Mg in the Al-Mg-Si ternary at the composition A, $\Delta \bar{G}_{Mg/Al-Mg}^{XS}$ denotes the excess partial molar free energy of mixing of Mg in the Al-Mg binary at the composition P, $\Delta \bar{G}_{Mg/Mg-Si}^{XS}$ denotes the excess partial molar free energy of mixing of Mg in the Mg-Si binary at composition Q, and $\Delta G_{m/Al-Si}^{XS}$ denotes the excess free energy of mixing of Al-Si binary at composition R.

The primary advantage of this technique, over other empirical techniques used for thermodynamic estimation, is that the binary values used in equation (3.3) correspond to the binary compositions closest to the ternary point A (Fig. 3.5). The excess free energies of mixing for the Al-Mg, Al-Si and Mg-Si binaries can be deduced from experimental data reported in literature [5,12,13] and are shown in Table 3.3.

The activity coefficient of Al in the Al-Mg-Si ternary can be similarly estimated from the limiting binaries using the following equation:

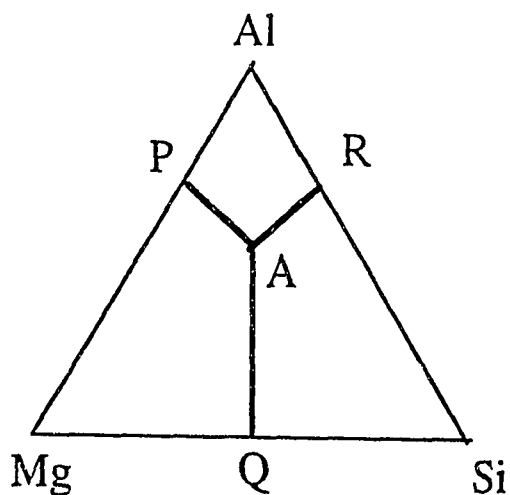


Fig. 3.5 Schematic description of Al-Mg-Si thermodynamics from the limiting binaries using the shortest distance composition path. Al-Mg-Si thermodynamics at composition A, estimated from the thermodynamics of Al-Mg at composition P, of Mg-Si at composition Q, and of Al-Si at composition R, respectively.

Table 3.3 Excess free energies of mixing for Al-Si, Mg-Si and Al-Mg binaries.

$$\Delta G_{m/Al-Si}^{XS} = X_{Si} X_{Al} [A_L + B_L(1 - 2X_{Si}) + C_L(1 - 6X_{Si} + 6X_{Si}^2)] \text{ J/mole [13]}$$

Coefficients	Value
A_L	$-10695.4 - 1.823 T$
B_L	$-4274.5 + 3.044 T$
C_L	$670.7 - 0.460 T$

$$\Delta G_{m/Mg-Si}^{XS} = X_{Si} X_{Mg} \sum_{i=0}^5 [(A_i - B_i T) X_{Si}^i] \text{ J/mole [12]}$$

i	A_i	B_i
0	-1.6735×10^5	-0.99474×10^2
1	0.57976×10^5	0.35266×10^2
2	6.9610×10^5	7.0744×10^2
3	-9.8494×10^5	-12.939×10^2
4	0	5.0384×10^2
5	0	-0.83281×10^2

$$\Delta G_{m/Al-Mg}^{XS} = 4.2(-1630.2 + 1.0292T) \text{ J/mole (for } X_{Mg} < 0.1) [5]$$

$$RT \ln \gamma_{Al} = \frac{X_{Si}^A (X_{Mg}^A + X_{Si}^A) \Delta \bar{G}_{Al/Al-Si}^{XS}}{(1 - X_{Al}^R)^2} + \frac{X_{Mg}^A (X_{Mg}^A + X_{Si}^A) \Delta \bar{G}_{Al/Al-Mg}^{XS}}{(1 - X_{Al}^P)^2} - \frac{X_{Mg}^A X_{Si}^A \Delta G_{m/Mg-Si}^{XS}}{X_{Mg}^Q X_{Si}^Q} \quad (3.4)$$

where γ_{Al} denotes the activity coefficient of Al in the Al-Mg-Si ternary at the composition A, $\Delta \bar{G}_{Al/Al-Mg}^{XS}$ denotes the excess partial molar free energy of mixing of Al in the Al-Mg binary at the composition P, $\Delta \bar{G}_{Al/Al-Si}^{XS}$ denotes the excess partial molar free energy of mixing of Al in the Al-Si binary at composition R, and $\Delta G_{m/Mg-Si}^{XS}$ denotes the excess free energy of mixing of Mg-Si binary at composition Q. For a given ternary composition, A (Fig. 3.5), X_{Al}^P , X_{Mg}^P , X_{Mg}^Q , X_{Si}^Q , X_{Al}^R and X_{Si}^R can be determined as shown below. These, along with the thermodynamic data of the binaries, can then be incorporated into equations (3.3) and (3.4) to determine the activity coefficients of Mg and Al in the Al-Mg-Si ternary.

$$\begin{aligned} X_{Mg}^P &= X_{Mg}^A + \frac{X_{Si}^A}{2} \\ X_{Al}^P &= X_{Al}^A + \frac{X_{Si}^A}{2} \\ X_{Mg}^Q &= X_{Mg}^A + \frac{X_{Al}^A}{2} \\ X_{Si}^Q &= X_{Si}^A + \frac{X_{Al}^A}{2} \\ X_{Al}^R &= X_{Al}^A + \frac{X_{Mg}^A}{2} \\ X_{Si}^R &= X_{Si}^A + \frac{X_{Mg}^A}{2} \end{aligned} \quad (3.5)$$

The symbols X_{Al}^A , X_{Mg}^A and X_{Si}^A denote the molar compositions of Al, Mg and Si respectively, at the point A in the Al-Mg-Si ternary diagram. X_{Al}^P and X_{Mg}^P denote the mole fractions of Al and Mg respectively at composition P, X_{Mg}^Q and X_{Si}^Q denote the mole fractions of Mg and Si respectively at composition Q, and X_{Al}^R and X_{Si}^R denote the mole fractions of Al and Si respectively at composition R. The computer program used to estimate the activity coefficient of Al and Mg in the Al-Mg-Si melt is presented in Appendix C.

3.4 Electrical Conductivity Experiments

3.4.1 Nature of Metal Distribution in Al₂O₃/Al Composite

Cylindrical shaped pellets of an Al₂O₃/Al composite and sintered Al₂O₃-4% MgO were prepared for electrical conductivity measurements. The Al₂O₃/Al composite was prepared by directed oxidation of a 5056 aluminum alloy for 48 hours at 1273 K in air, in the thermogravimetric setup shown in Figure 3.1. The Al₂O₃-MgO pellet was prepared by sintering a mixture of fine powders, 110 μm average particle size, of 96 wt% Al₂O₃ and 4 wt% MgO at 1673 K for 48 hours in an argon atmosphere.

Fig. 3.6 shows the experimental set-up used for measuring the electrical conductivity of the pellets using the two electrode method. The set-up consisted of an electrical conductivity cell, vertical tube furnace and an electrical conductivity measurement unit, Quad Tech RLC Digibridge Model 1689 M. The conductivity cell consisted of a gas tight alumina chamber with gas flow, thermocouple and electrical feedthroughs. The pellet was placed between the platinum foils as shown in Fig. 3.6. Platinum paint was applied on the flat surfaces of the sample to achieve good contact with the electrodes.

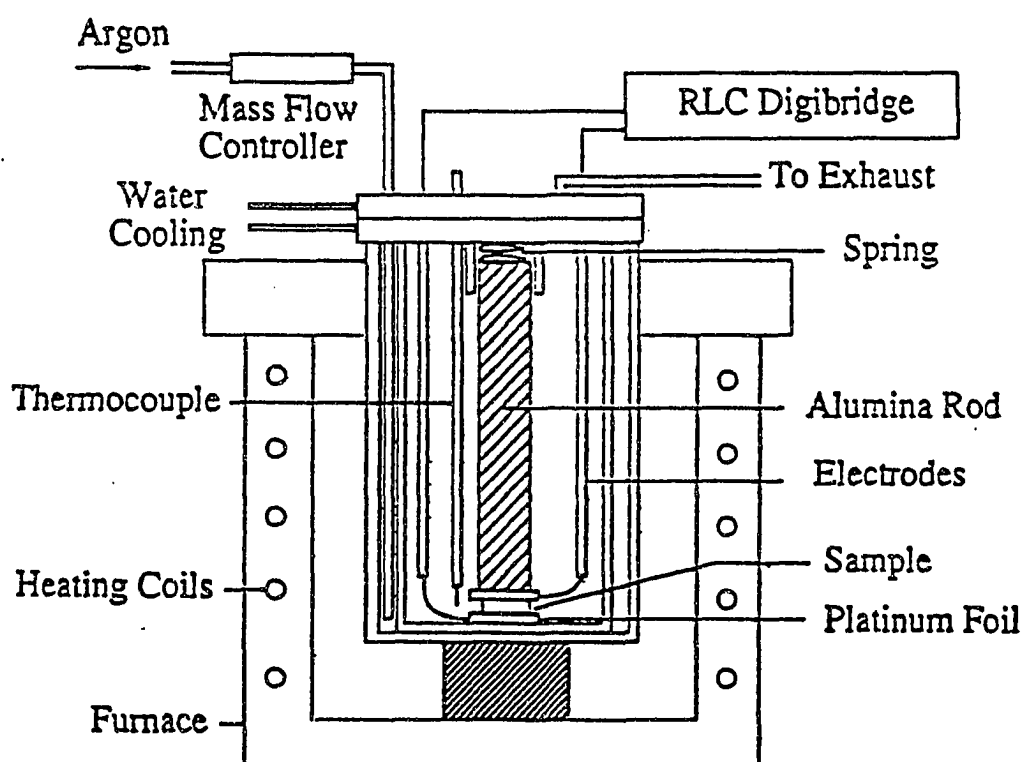


Fig. 3.6 Schematic description of the conductivity setup.

Resistance measurements were made as a function of temperature by heating the samples in argon at atmospheric pressure and a gas flow rate of 500 sccm. A Pt/Pt-10% Rh thermocouple placed in close proximity to the sample was used to measure the sample temperature. The RLC Digibridge was operated at low test frequency, 12 Hz, to improve the accuracy of the readings. Furthermore, the resistance measurements were made during the time interval when no current was flowing to the furnace to minimize inductive effects on the measured impedance.

3.4.2 Dependence of Metal Distribution on Growth Temperature

Al₂O₃/Al composites were grown by directed oxidation of the Al 5056 alloy in the temperature range of 1393 to 1612 K in the thermogravimetric set-up shown in Figure.

3.1. SiO₂ powder was applied to the surface of the alloy to minimize the duration of incubation. In all the experiments, oxidation was carried out till the weight gain recorded was 1000 mg. Electrical conductivity measurements of the composites were conducted in the setup shown in Figure 3.6 to determine the change in metal distribution as a function of the growth temperature. The temperature of conductivity measurements was kept constant at 298 K.

Microstructural characterization of the composites included optical metallography and scanning electron microscopy (SEM). Metallographic samples were sectioned with a low-speed diamond saw, ground and polished with diamond paste. SEM specimens were coated with carbon to eliminate charging under the electron beam. The amount of metal in the composites was determined from the micrographs by image analysis.

3.5 Growth into Preforms

The directed oxidation of Al-Mg alloys (Al-5056) into loosely packed Al_2O_3 preforms was studied in the TGA set-up, shown in Fig. 3.1. The Al-5056 alloy cylinders were placed at the bottom of the Al_2O_3 crucibles, and then covered with Al_2O_3 powder. Powders of average particle sizes, ranging from 0.53 to 110 μm , were used. The directed oxidation experiments were carried out at 1450 K, and at an oxygen pressure of 85092 Pa. For the 8 μm Al_2O_3 preform, composite growth was also carried out at various partial pressures of oxygen. In all experiments, the total weight of the Al_2O_3 powder in the preform was 500 mg. The Al_2O_3 layer thickness was estimated to be 3.5 mm. Composite growth occurs upward, away from the alloy surface, infiltrating the preform from beneath, as shown in Fig. 1.1.

The presence of the Al_2O_3 preform reduces the cross-sectional area of the melt exposed to the oxidizing atmosphere. The reduction in cross-sectional area can be determined from the packing density of the preform. The packing density of the Al_2O_3 preform was estimated, by assuming a random loose packing of monodisperse Al_2O_3 particles in the preform. Hence, the packing density of the Al_2O_3 preform, used in this study, was assumed to be 55 % [15]. Similarly, for random loose packing, the pore size in the Al_2O_3 preform is estimated to be 0.414 times the particle size [16]. The characteristics of the preforms used in this study are given in Table 3.4.

Table 3.4 Description of the characteristics of the alumina preforms used in the directed oxidation of Al-5 wt% Mg alloy.

Particle size, μm	Pore size, μm	Surface area per unit volume $\times 10^{-6}$, m^{-1}
0.53	0.22	1.9
8	3.3	0.125
16	6.6	0.0625
110	45.5	0.0091

3.6 References

1. R. B. Bird, W. E. Stewart and E. N. Lightfoot, *Transport Phenomena*, Wiley, New York, 1960.
2. S. V. Patankar, *Numerical Heat Transfer and Fluid Flow*, McGraw Hill, New York, 1980.
3. S. V. Patankar, Reference Manual for MicroCompact Version 1.1, Innovative Research Inc., Minneapolis, MN, 1988.
4. M. W. Chase, Jr., C. A. Davies, J. R. Bowary, Jr., D. J. Fromp, R. A. McDonald and A. N. Syverud, JANAF Thermochemical Tables, 3rd ed., American Chemical Society, Washington, DC, 1986.
5. B. L. Tiwari, "Thermodynamic Properties of Liquid Al-Mg Alloys Measured by the Emf Method," *Metall. Trans A.*, **18A** 1645-51 (1987).
6. A. E. Standage and M. S. Gani, "Reaction Between Vitreous Silica and Molten Aluminum," *J. Am. Ceram. Soc.*, **50** [2] 101-105 (1967).
7. P. Xiao and B. Derby, "Alumina/Aluminum Composites Formed by the Directed Oxidation of Aluminum Using Sodium Hydroxide as a Surface Dopant," *J. Am. Ceram. Soc.*, **77** [7] 1771-76 (1994).
8. E. Manor, H. Ni, C. G. Levi and R. Mehrabian, "Microstructure Evolution of SiC/Al₂O₃/Al-Alloy Composites Produced by Melt Oxidation," *J. Am. Ceram. Soc.*, **76** [7] 1777-87 (1993).
9. H. Venugopalan, K. Tankala and T. DebRoy, "Probing the Initial Stage of Synthesis of Al₂O₃/Al Composites by Directed Oxidation of Al-Mg Alloys," accepted for publication in *Metallurgical and Materials Transactions*.
10. O. Kubaschewski, C. B. Alcock and P. J. Spencer, *Materials Thermochemistry*, Pergamon Press, 1993.
11. I. Aksay, C. E. Hoge and J. A. Pask, "Wetting under Chemical Equilibrium and Non-Equilibrium Conditions," *J. Phys. Chem.*, **78** [12] 1778-83 (1974).
12. A. A. Nayeb-Hashemi and J. B. Clark, "The Magnesium-Silicon System," *Bull. Alloy. Phase. Diag.*, **5** [6] 584-92 (1984).

13. J. L. Murray and A. J. McAlister, "The Aluminum- Silicon System," *Bull. Alloy. Phase. Diag.*, **5** [1] 74-84 (1984).
14. K. T. Jacob and K. Fitzner, "The Estimation of the Thermodynamic Properties of Ternary Alloys From Binary Data Using the Shortest Distance Composition Path," *Thermochimica Acta*, **18** 197-206 (1977).
15. G. Y. Onoda and E. G. Liniger, "Random Loose Packing of Uniform Spheres and the Dilatancy Onset," *Phys. Rev. Lett.*, **64** 2727-2730 (1990).
16. G. T. Nolan and P. E. Kavanagh, "Octahedral Configurations in Random Close Packing," *Powder Technology*, **83** 253-58 (1995).

CHAPTER 4

RESULTS AND DISCUSSION

4.1 Mechanism of Initial Stage

Fig. 4.1 shows the weight gain of the Al-Mg alloy samples as a function of time for various oxygen partial pressures at a temperature of 1391 K and total pressure of 93303 Pa [1]. It is observed from the figure that both the total weight gain during the initial stage of oxidation and the duration of the initial stage decrease with increasing partial pressure of oxygen. Furthermore, the rate of oxidation increases with increasing oxygen pressure. In all cases, the initial stage of oxidation ends abruptly. In addition, a close examination of the data indicates that the weight gain rate decreases with time at low oxygen pressures and is constant at high oxygen pressures. Several interesting questions arise from a perusal of this data. What is the mechanism of initial stage oxidation of Al-Mg alloys? Why does the weight gain rate decrease with time at low oxygen pressures and why is the rate independent of time at high oxygen pressures? Why is the duration of the initial stage short at high oxygen pressures? Why does the initial stage end abruptly?

The oxidation experiments were terminated at the end of the initial stage and the samples were examined. A loose, fine, white powder was observed on the surface of the sample and on the inner walls of the crucible. X-ray diffraction data of the white powder on the sample and on the walls of the crucible, presented in Fig. 4.2, indicated the powder to be MgO. The presence of MgO on the walls of the crucible confirms that the mechanism of oxidation in the initial stage involves evaporation of magnesium from the melt followed by its oxidation in the vapor phase.

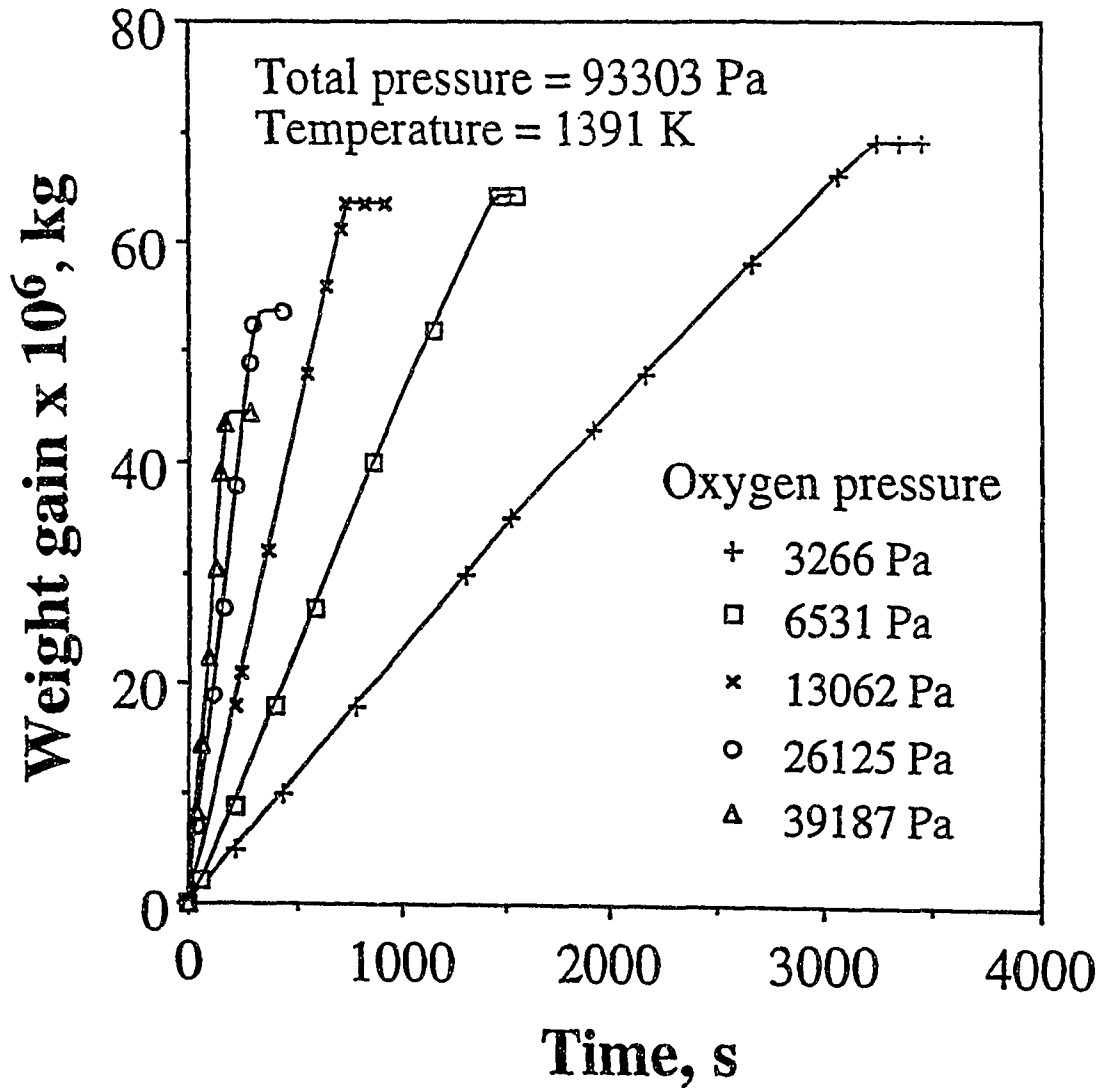


Fig. 4.1 Plot of weight gain vs time in the initial stage for various oxygen pressures.

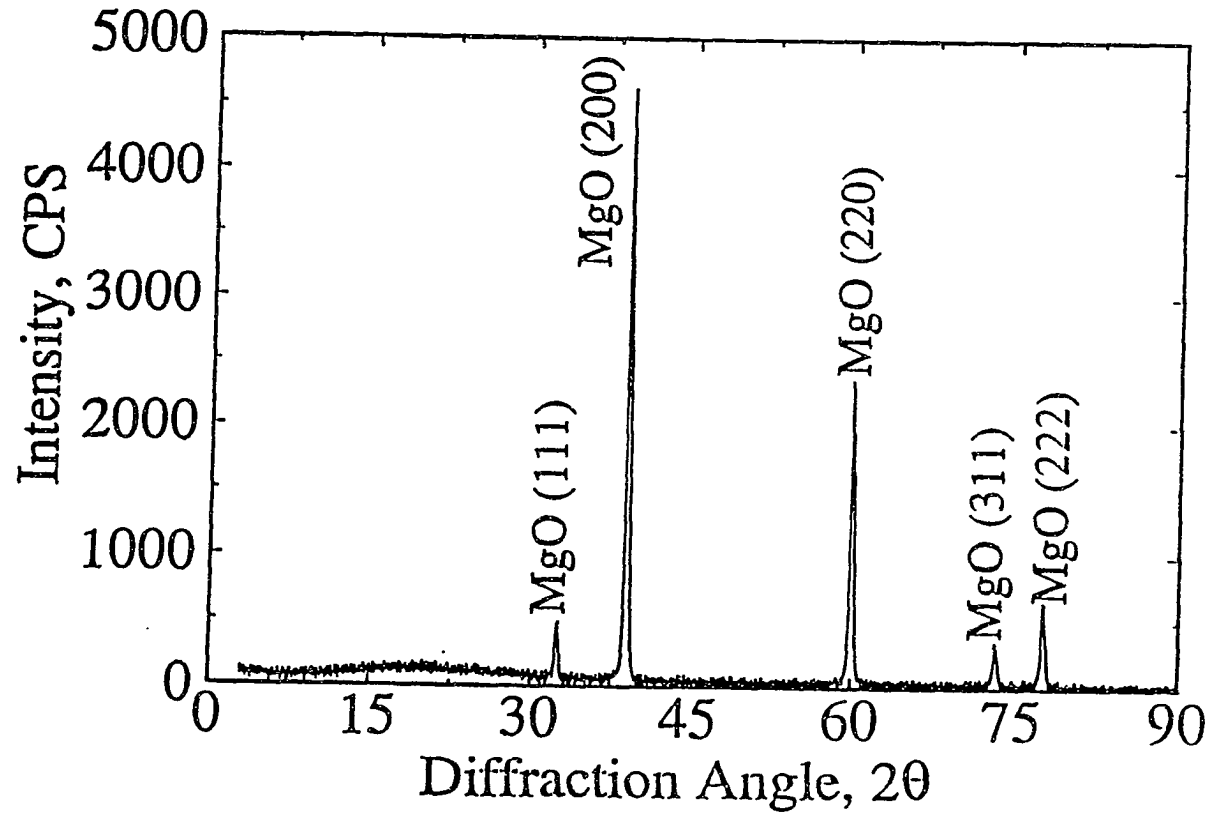


Fig. 4.2 X-ray diffraction pattern of the white powder formed on the crucible walls, during the initial stage of oxidation of Al-Mg alloys.

The velocity, temperature and concentration fields of oxygen and magnesium in the gas phase were computed to understand the vapor phase oxidation of magnesium. Fig. 4.3 shows the computed velocity field and the concentration profiles of magnesium and oxygen in the gas phase at the initiation of oxidation for an oxygen partial pressure of 3266 Pa, a total pressure of 93303 Pa at 1391 K. The calculated velocity field indicates that the velocity of the gas is negligible within the crucible above the melt surface because the gas is confined in this region. The computed concentration field, presented in Fig. 4.3, shows that the concentration profiles within the crucible are parallel to the melt surface indicating that the profiles are established primarily by diffusion and are not influenced by convection. The relative importance of convection and diffusion within the crucible can be examined from the Peclet number for mass transfer which is the ratio of convective mass transfer to diffusive mass transfer. The Peclet number for mass transfer, Pe , is given by $Pe = uL/D$ where u is the velocity, L is the characteristic length, and D is the diffusion coefficient of Mg vapor. Using typical values of 0.0015 cm/s, 3 cm²/s, and 0.8 cm, for u , D , and L respectively, the Peclet number is estimated to be of 4.6×10^{-3} . This indicates that mass transfer in the gas phase occurs primarily by diffusion. Thus, the concentration profiles are consistent with the calculated Peclet number for mass transfer.

The velocity and concentration profiles, presented in Fig. 4.3, indicate that a diffusion boundary layer is established within the crucible. A counter diffusion of Mg vapor and O₂ gas in argon takes place. At a short distance from the surface of the alloy, Mg vapor reacts with oxygen forming an MgO mist according to reaction (4.1).



The concentration profile indicates that the reaction of Mg vapor and oxygen to form MgO in the gas phase occurs within the confines of the crucible. Hence all the MgO formed by

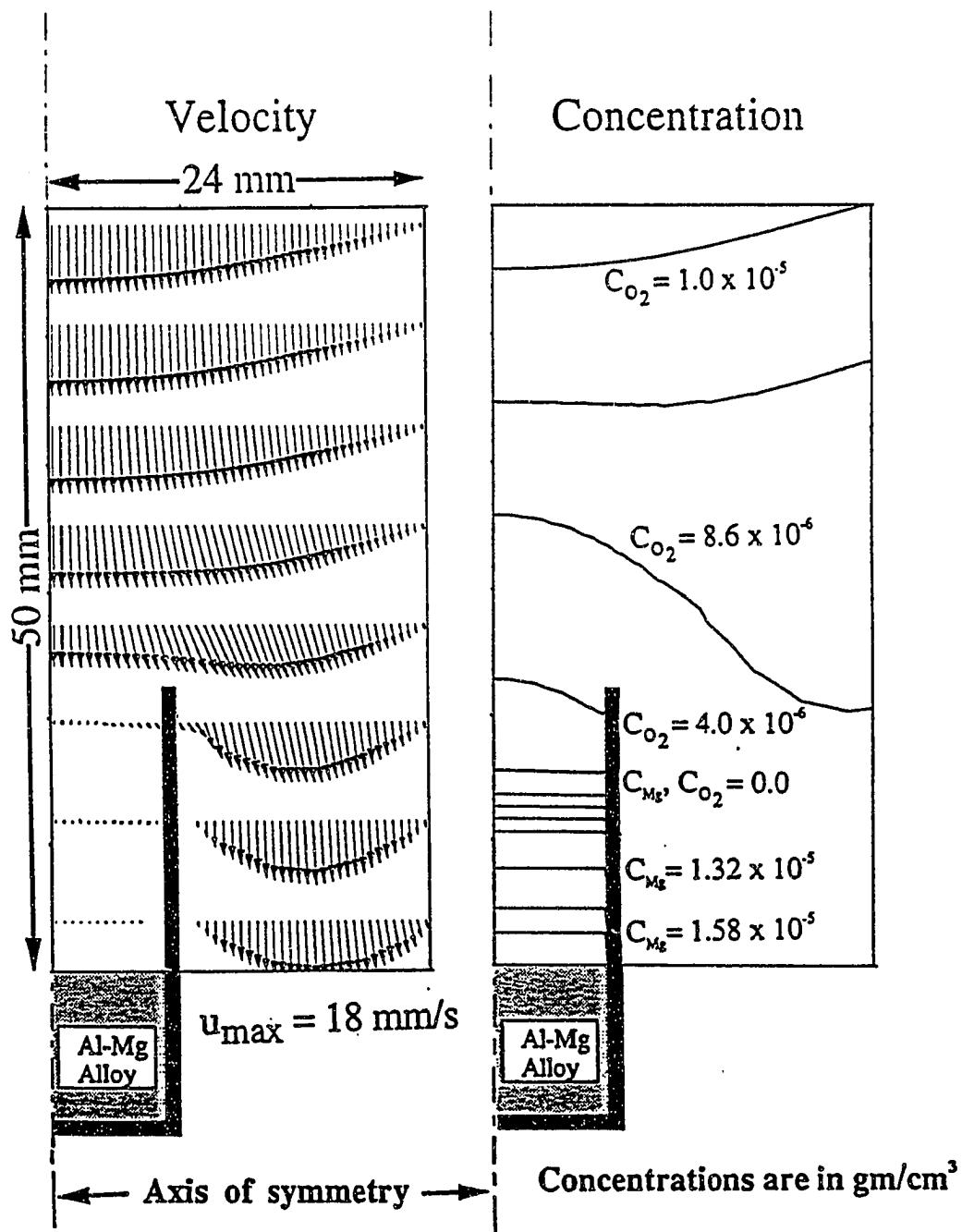


Fig. 4.3 Computed velocity and concentration profiles of magnesium and oxygen in the gas phase, for an oxygen pressure of 3266 Pa, total pressure of 93303 Pa at 1391 K, at the initiation of the experiment. (Note: $1 \text{ gm/cm}^3 = 10^3 \text{ kg/m}^3$)

the vapor phase oxidation fell back on to the crucible and was registered as a weight gain by the balance. Since the formation of MgO requires one mole of oxygen for every two moles of Mg vapor, the Mg vaporization rate, calculated from the model, can be used to determine the corresponding weight gain rate and compared with the experimentally observed rate.

It is observed from Fig. 4.3 that the gas phase is divided into two distinct zones, a magnesium vapor-argon region close to the melt surface and an oxygen-argon region above this region. A schematic diagram showing this division of the boundary layer and the formation of an MgO mist is presented in Fig. 4.4. At any given instant, the molar fluxes of magnesium vapor, J_{Mg} , and oxygen, J_{O_2} , are given by:

$$J_{Mg} = \frac{D_{Mg}(p_{Mg} - p_{Mg}^i)}{\delta RT} \quad (4.2)$$

$$J_{O_2} = \frac{D_{O_2}(p_{O_2} - p_{O_2}^i)}{(\Delta - \delta)RT} \quad (4.3)$$

where D_{Mg} is the interdiffusivity of the Mg(g)-Ar pair, D_{O_2} is the interdiffusivity of the Ar-O₂ pair, δ is the distance between the alloy surface and the location in the vapor phase where MgO forms, Δ is the sum of the thicknesses of Mg and O₂ boundary layers, T is the temperature, p_{Mg} is the vapor pressure of Mg at the surface of the alloy, p_{Mg}^i and $p_{O_2}^i$ are the partial pressure of magnesium and oxygen at the reaction interface, respectively, and p_{O_2} is the partial pressure of oxygen at a distance Δ from the surface of the alloy. Since p_{Mg}^i and $p_{O_2}^i$ are much smaller than p_{Mg} and p_{O_2} , respectively, they can be neglected in equations (4.2) and (4.3). From the stoichiometry of reaction (4.1) we obtain:

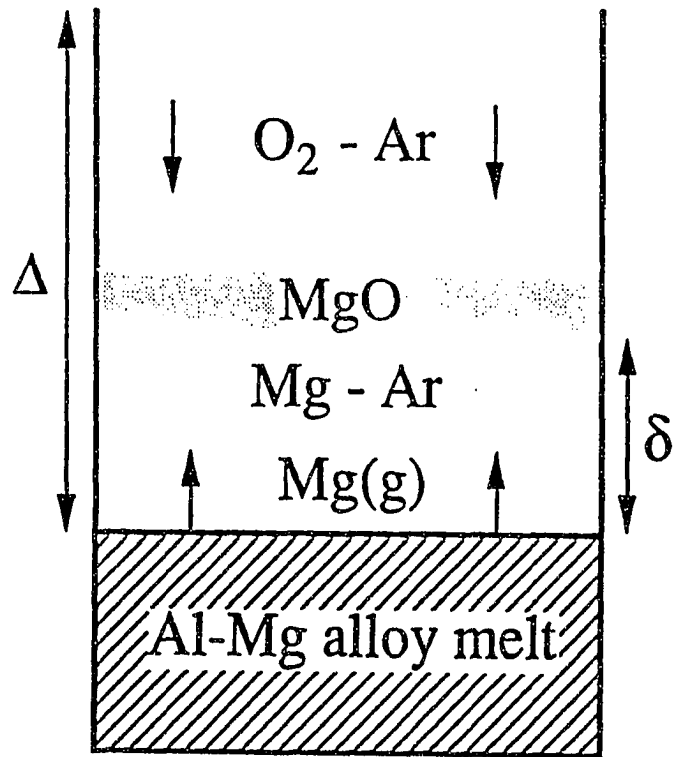


Fig. 4.4 Schematic diagram showing the magnesium and oxygen boundary layers formed in the gas phase above the melt and within the crucible during the initial stage of oxidation of Al-Mg alloys.

$$J_{Mg} = 2J_{O_2} = \frac{2D_{O_2}P_{O_2}}{(\Delta - \delta)RT} \quad (4.4)$$

For non-zero values of p_{O_2} and p_{Mg} , we can rearrange equations (4.2) through (4.4) to obtain:

$$J_{Mg} = \frac{2D_{O_2}P_{O_2}}{\Delta RT} \left[1 + \frac{D_{Mg}P_{Mg}}{2D_{O_2}P_{O_2}} \right] \quad (4.5)$$

and the weight gain rate, R , based on the stoichiometry of the reaction is given by:

$$R = 0.5M_{O_2}J_{Mg} = \frac{M_{O_2}D_{O_2}P_{O_2}}{\Delta RT} \left[1 + \frac{D_{Mg}P_{Mg}}{2D_{O_2}P_{O_2}} \right] \quad (4.6)$$

Furthermore, since $D_{Mg} \approx D_{O_2}$, we have:

$$R = 0.5M_{O_2}J_{Mg} = \frac{M_{O_2}D_{O_2}P_{O_2}}{\Delta RT} \left[1 + \frac{P_{Mg}}{2P_{O_2}} \right] \quad (4.7)$$

The vapor pressure of Mg over the melt for the starting alloy composition of 5 wt% Mg is 5838 Pa. It is seen from equation (4.7) that for an oxygen pressure of 3266 Pa, the second term within the bracket is of comparable magnitude to the first term which is one. Therefore, both the terms within the bracket have an equal influence on the weight gain rate. As Mg concentration in the melt decreases with time due to vaporization, the Mg vapor pressure over the melt decreases, and hence, less oxygen is consumed in the reaction. Thus, p_{Mg} and, consequently, the weight gain rate change with time. Fig. 4.5(a) shows a comparison of the experimental and calculated weight gain with time for an oxygen partial pressure of 3266 Pa. It is observed that the calculated weight gain is in good agreement

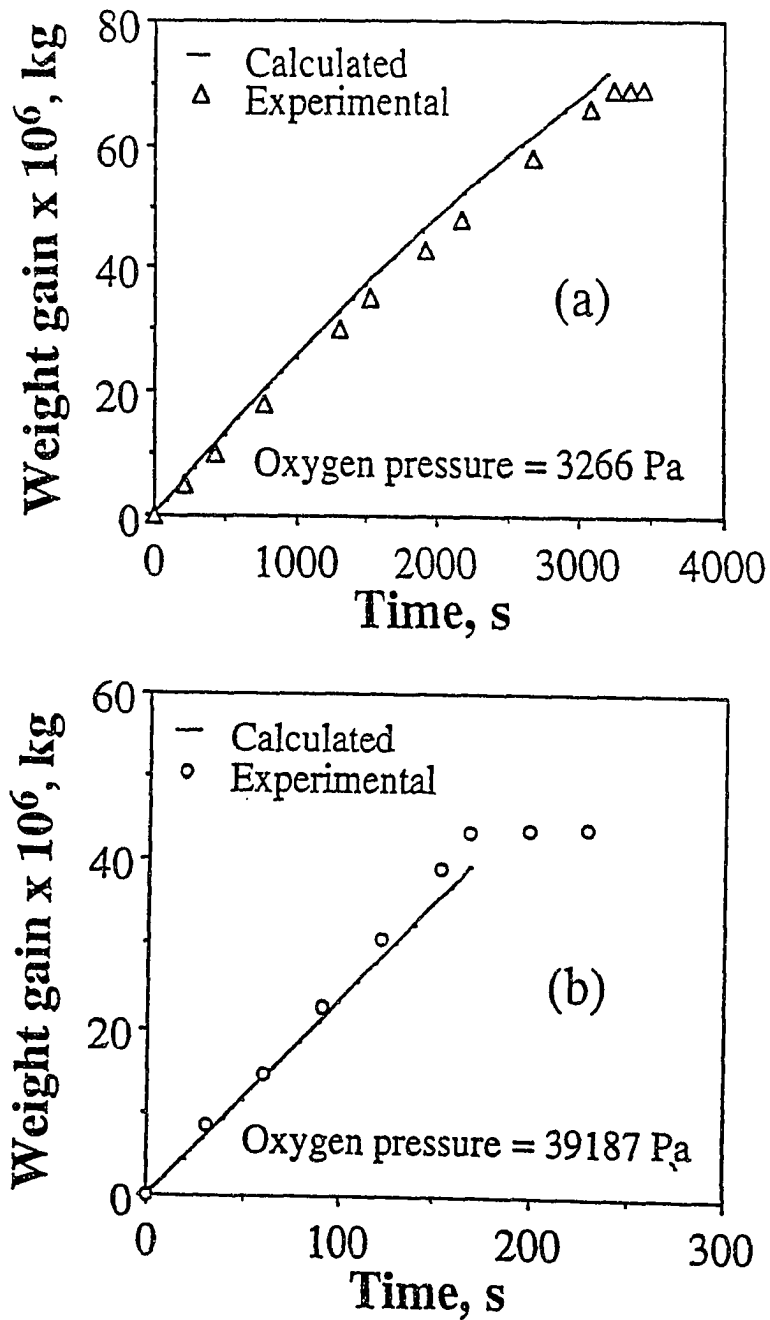


Fig. 4.5 Comparison of experimental and calculated weight gain vs time for oxygen pressures of (a) 3266 Pa and (b) 39187 Pa. Experiments were done at 1391 K and 93303 Pa total pressure.

with experimental data. Furthermore, the slope of the weight gain curve decreases with time indicating a decrease in the weight gain rate from start to finish of the initial stage of oxidation. Thus, the model explains the decrease in weight gain rate with time at low oxygen partial pressures.

At an oxygen pressure of 39187 Pa, the second term in equation (4.7) is of much smaller magnitude than the first term (which is one) within the bracket. Therefore, any decrease in the second term due to a decrease in Mg vapor pressure with time does not change the values of the terms within the square bracket significantly. At high oxygen pressures, the rate of reaction enhanced vaporization of a volatile constituent of an alloy is mildly dependent on the vapor pressure of the constituent and strongly dependent on the oxygen partial pressure. This nearly constant weight gain rate with time at high oxygen pressures is clearly seen in Fig. 4.5(b) for an inlet oxygen pressure of 39187 Pa where the weight gain rate changes by 5% from the start to the end of the initial stage while the Mg composition in the alloy changes from 5.5 mole% to 2.93 mole%. Thus, the model predictions are consistent with the observed trends in weight gain rate at both low and high oxygen pressures.

4.1.1 Effect of Diffusivity on the Oxidation Rate

Equation (4.7) indicates that the weight gain rate is influenced by the diffusivity of oxygen in the gas phase. If the vaporization of magnesium is diffusion limited, a change in diffusion coefficient would result in a corresponding change in the weight gain rate. Two sets of experiments were conducted to confirm the reaction enhanced, gaseous diffusion limited, vaporization of magnesium. In one set, the oxidation was carried out keeping the total pressure and the partial pressure of oxygen constant. The diffusivities of O₂ and Mg(g) were varied by changing the type of inert diluent gas, argon or helium, mixed with

oxygen. Fig. 4.6 is a plot of the observed weight gain versus time in O₂-Ar and O₂-He atmospheres for a total pressure of 93303 Pa and an oxygen partial pressure of 13062 Pa. It is observed that the initial weight gain rate in helium is much higher than that in argon. The higher rate in He is consistent with the higher diffusivities of Mg(g) and O₂ in He (from Appendix A) as compared to that in Ar and is consistent with the prediction of equation (4.7). In a second set, experiments were conducted at various total pressures for a constant oxygen partial pressure of 6531 Pa at 1391 K. Fig. 4.7(a) is a plot of the observed weight gain versus time for different total pressures. The results show that the weight gain rate increases with decreasing total pressure. Since the binary diffusivity of gases is inversely proportional to the total pressure, a decrease in the total pressure results in an increase in the diffusivities of O₂ and Mg(g) in argon and should result in an increase in weight gain rate. Fig. 4.7(b) shows the variation in weight gain rate with diffusivity of oxygen. The results show a good correlation between weight gain rate and diffusivity and are consistent with the predictions of equation (4.7). Thus, the results support the model of diffusion limited vaporization of magnesium during the initial stage of oxidation of Al-Mg alloys.

4.1.2 Termination of the Initial Stage

Figs. 4.1, 4.6 and 4.7(a) show that the culmination of the initial stage of composite growth and the start of the incubation period is characterized by a sharp decrease in the weight gain rate. According to Vlach et al. [2], this sharp decrease in the rate occurs due to the formation of a dense spinel layer which prevents magnesium vaporization and its subsequent oxidation. For alloy compositions between 0.2 and 10.4 mole% Mg, the magnesium aluminate spinel is thermodynamically more stable than MgO at 1400 K [3,4]. The spinel layer can form at the melt surface by one of the following reactions:

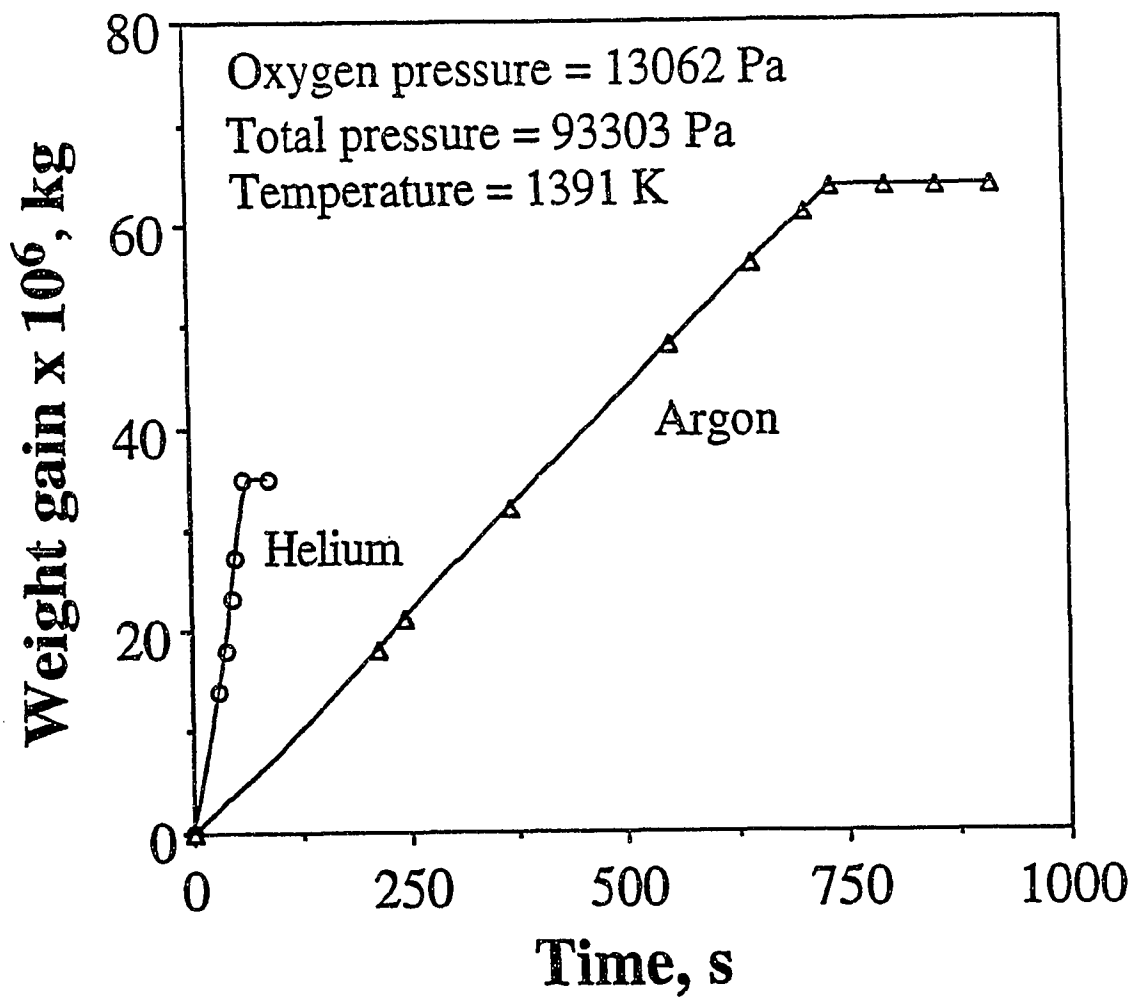


Fig. 4.6 Weight gain vs time during initial stage of oxidation of Al-Mg alloys in O₂-Ar and O₂-He atmospheres.

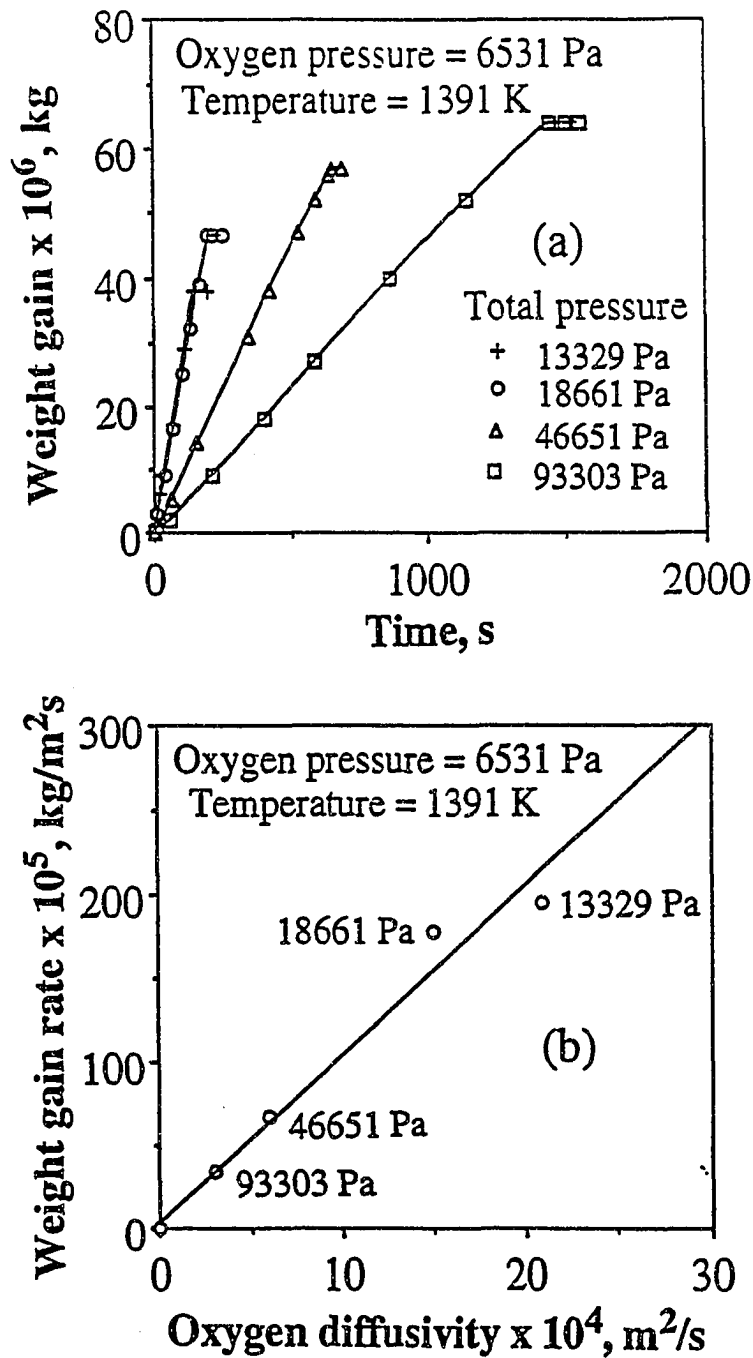


Fig. 4.7 (a) Weight gain vs time in the initial stage of oxidation for different total pressures. (b) Weight gain rate in the initial stage vs oxygen diffusivity in the reactive atmosphere.



Formation of spinel by reaction (4.8) involves reaction of MgO with the alloy. Since MgO starts forming as soon as oxygen is introduced into the reactor, there is no reason to believe that the spinel formation should not start at the same time. If the spinel formation were to start as MgO forms, the cross-section of the melt exposed to the oxygen atmosphere would decrease. However, the model does not take into account the decrease in the cross-section of the melt surface, and yet, there is excellent agreement between the experimental observations and model predictions of weight gain vs time. If spinel formation occurs by way of reaction (4.8), the end of initial stage would correspond to a critical amount of MgO necessary to form an impervious spinel layer of certain thickness to stop further Mg vaporization. This entails that the same amount of MgO form at the end of the initial stage, irrespective of the experimental conditions of oxygen pressure and total pressure. However, it is observed that the weight gain at the end of the initial stage, which is a measure of the amount of MgO formed, is different for different oxygen pressures, and total pressures, as evidenced from Figures 4.1 and 4.7(a), respectively. This suggests that the formation of spinel does not occur by reaction (4.8) at a sufficiently rapid rate in the initial phase of oxidation.

The experimental results and the preceding discussion indicate that spinel formation involves the presence of oxygen at the melt surface. Fig. 4.8 indicates that at the start of initial stage of oxidation, the oxygen front is located far away from the surface and hence the spinel formation cannot occur during the initial stage of oxidation. However, Fig. 4.8 also indicates that the oxygen front moves closer to the surface of the melt owing to a decrease in the magnesium vapor pressure as the initial stage progresses. Furthermore, Fig.

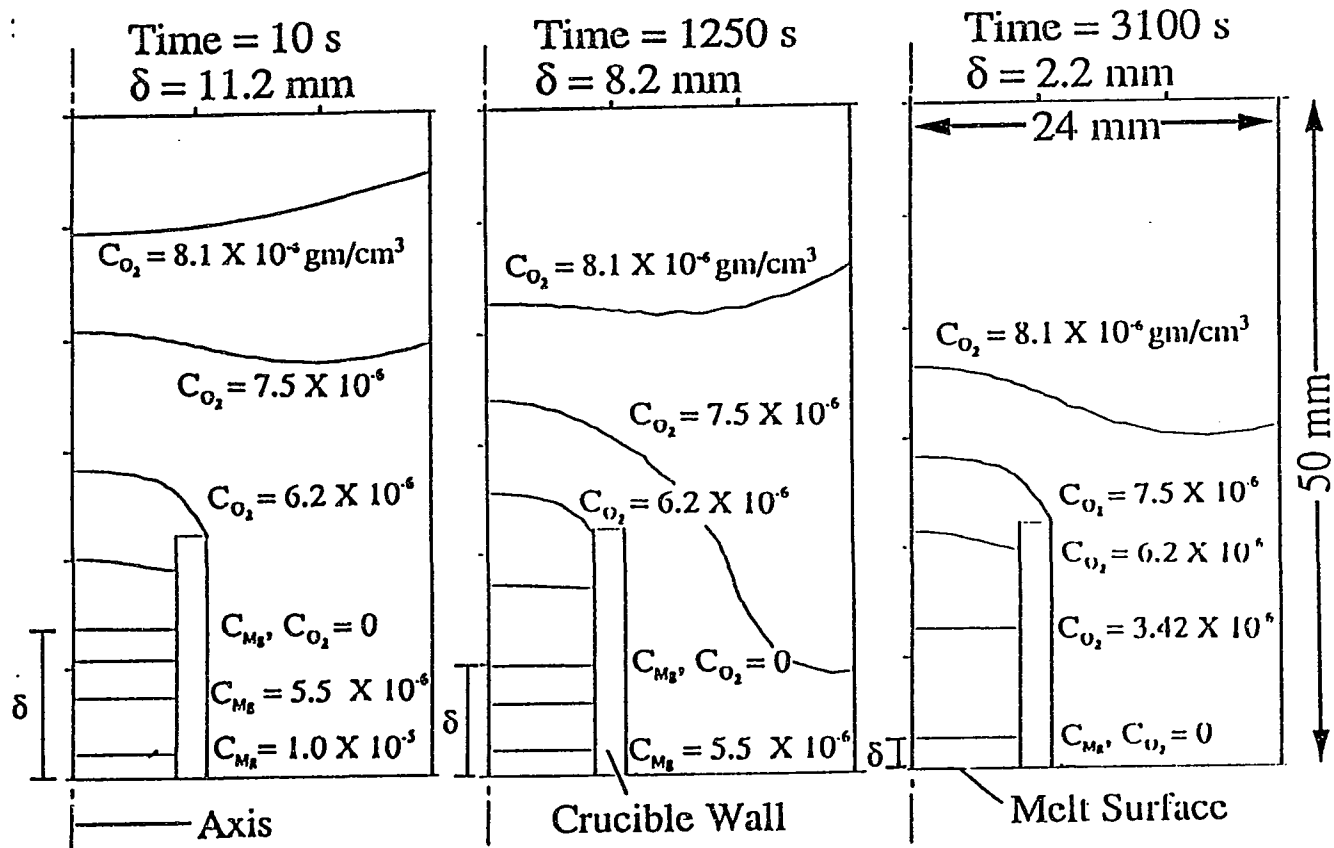


Fig. 4.8 Computed concentration profiles of magnesium and oxygen in the gas phase for an oxygen pressure of 3266 Pa, total pressure of 93303 Pa, at 1391 K. The profiles show the movement of the oxygen front towards the melt surface with time. (Note: 1 gm/cm³ = 10³ kg/m³)

4.9 shows that at the end of the initial stage the thickness of the magnesium boundary layer, δ , is reduced to a small value and the oxygen front is present very close to the surface of the melt. The duration of the initial stage corresponds to the time required for the thickness of the magnesium vapor-inert gas layer, δ , to become sufficiently small so that oxygen can reach the melt surface and react with the alloy to form spinel.

4.2 Growth Stage Kinetics of Al-Mg Alloys

A typical weight gain vs time curve observed in the directed oxidation of Al-Mg alloys is shown in Figure 1.2 in the chapter on introduction in page 7. The process starts with a rapid but limited oxidation event upon introduction of oxygen in the furnace. The initial oxidation, corresponding to the formation of MgO, ends abruptly with the formation of an MgAl₂O₄ film on the alloy surface. This event is followed by an incubation period where the weight gain is small. The onset of bulk growth is marked by a substantial increase in the oxidation rate. The kinetics and mechanism of growth stage of composite synthesis from Al-Mg alloys, with or without silicon, are discussed in the following sections.

Figure 4.10 is a plot of weight gain vs time for Al-Mg alloys for oxygen pressure of 85.1 kPa in the initial and incubation stages and varying oxygen pressures in the growth stage [5]. It is observed that the oxidation rate in the growth stage decreases with time and, within experimental uncertainty, remains practically independent of oxygen pressure. Similarly, weight gain, as a function of time, was measured at various temperatures (1373 - 1450 K) for an oxygen pressure of 85.1 kPa. The weight gain rates, at a weight gain of 300 mg, were measured from the slopes and plotted as a function of temperature in Fig. 4.11. The activation energy is found to be 361 kJ/mole. Several important questions arise from the perusal of the rate data. Why does the weight gain rate decrease with time? Why is

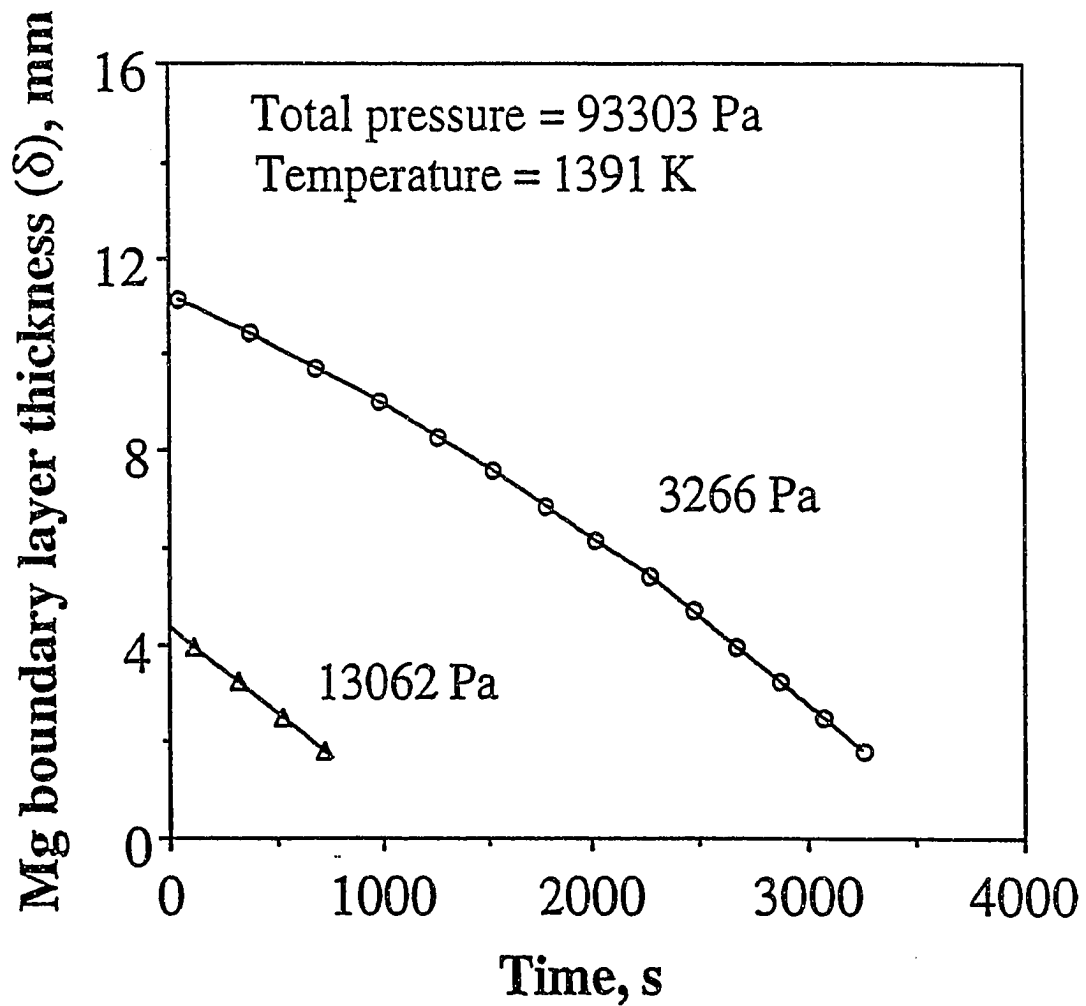


Fig. 4.9 Computed variation in the thickness of the Mg boundary layer (δ) during the initial stage of directed oxidation as a function of time for two different partial pressures of oxygen.

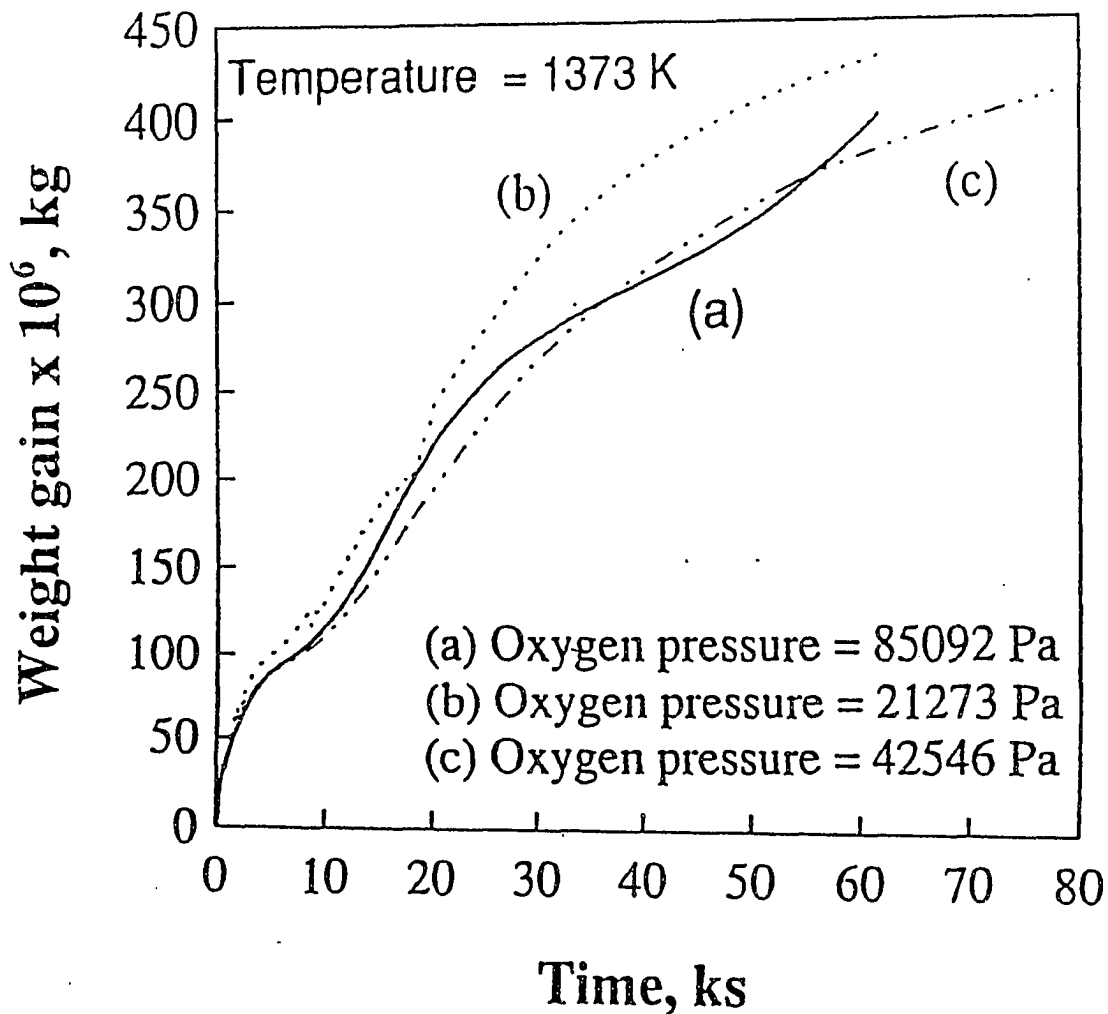


Fig. 4.10 Weight gain vs time for the Al-Mg alloy at different oxygen pressures in the growth stage: (a) 85092 Pa, (b) 21273 Pa, and (c) 42546 Pa. The oxygen pressure was initially maintained at 85092 Pa and subsequently changed in the growth stage. The total pressure, temperature and the total gas flow rate were maintained constant at 93303 Pa, 1373 K and 8333 mm³/s STP, respectively.

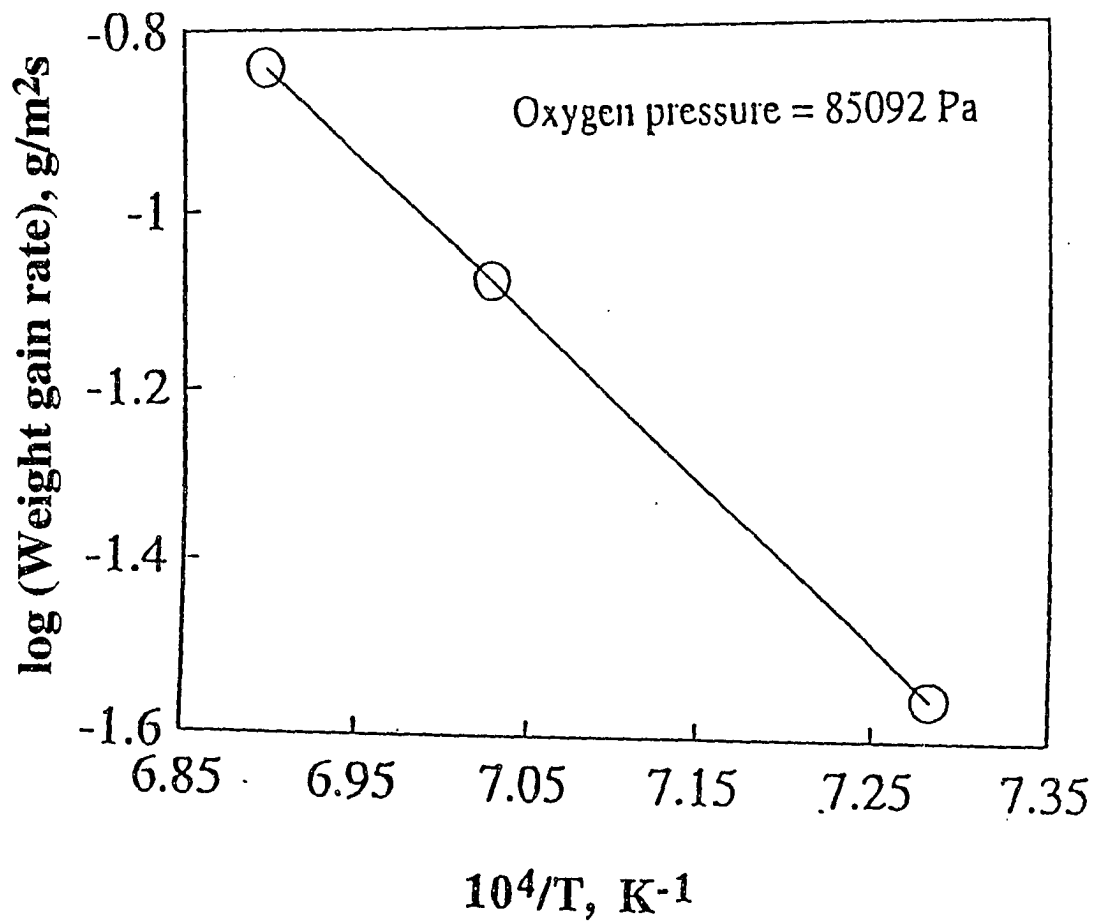


Fig. 4.11 Weight gain rate vs temperature for Al-Mg alloy for an oxygen pressure of 85092 Pa. The total pressure and the total gas flow rate were maintained constant at 93303 Pa and 8333 mm³/s STP, respectively.

the weight gain rate practically independent of oxygen pressure? What is the rate controlling mechanism in the growth stage of directed oxidation of Al-Mg alloys?

As shown in Fig. 1.3, the composite structure near the growth surface [6-7] consists of a continuous Al_2O_3 -doped MgO layer on top of the alumina matrix with a thin aluminum alloy film separating the two layers. At the MgO/Al alloy film interface, MgO dissociates and the oxygen dissolves in the alloy film and is transported to the Al_2O_3 /Al alloy film interface where composite growth takes place epitaxially. The magnesium ions formed by the dissociation of MgO diffuse through the MgO layer to the MgO/air interface where they are oxidized to regenerate MgO. This ionic transport is accompanied by electronic conduction (holes or electrons) to maintain charge neutrality and is taken to be the rate limiting process in the regeneration of MgO [8]. The supply of liquid aluminum to the alloy film/alumina interface is sustained by wicking of metal through channels in the alumina. Thus, the three possible rate controlling steps in the growth of Al_2O_3 /Al composites from Al-Mg alloys are: (i) electronic transport through the external MgO layer, (ii) transport of liquid metal by capillarity through the interconnected metal channels in the alumina, and (iii) dissociation of MgO and the subsequent transport of oxygen from the MgO/alloy film interface to the Al_2O_3 /alloy film interface.

The existence of long columns of composite containing Al_2O_3 grains of similar orientation [6,7] disqualifies any process involving repeated nucleation of grains. This indicates that the growth process is continuous. Indeed, it can be observed from the composite macrostructure (Fig. 4.12) that the growth surface on the whole is macroscopically smooth. Hence, an one-dimensional model can be used to theoretically estimate the rates of the various transport processes involved in Al_2O_3 growth. The experimental results in Figures 4.10 and 4.11 are analyzed below in detail to determine which of the transport

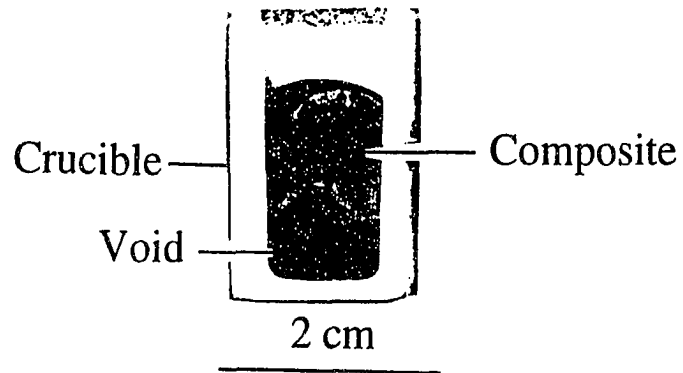


Fig. 4.12 Macrostructure of composite (top of crucible) grown from Al- 5 wt% Mg alloy (bottom of crucible).

steps are consistent with the observed growth rate and its dependence on time, oxygen pressure, and temperature.

4.2.1 Electronic Transport through MgO

Since MgO is unstable for the alloy compositions typically used in directed oxidation [3-4], MgO dissociates at the alloy film/MgO interface to provide dissolved oxygen in the alloy which is subsequently transported to the Al₂O₃/alloy film interface. The MgO could be regenerated either by the outward diffusion of magnesium ions to the external surface or by the inward diffusion of oxygen ions from MgO/air interface to the MgO/alloy film interface (Fig. 1.3). According to Nagelberg et al. [8], transport through the MgO layer is controlled by grain boundary diffusion of magnesium ions. This ionic transport is accompanied by electronic conduction (holes or electrons) to maintain charge neutrality and is taken to be the rate limiting process. Near the external surface, in the Al₂O₃-doped MgO, electron holes are the dominant electronic defects and their concentration is proportional to $P_{O_2}^{1/4}$, where P_{O_2} is the partial pressure of oxygen in the reaction chamber [8]. This behavior follows from the following defect reactions for the dissolution of alumina and oxygen in MgO:



where $V_{Mg}^{''}$ denotes a magnesium ion vacancy, Al_{Mg}^{\bullet} represents the dissolved aluminum concentration in MgO, and h indicates a hole. Similarly, for the low oxygen pressures near the alloy film, the concentration of electrons in MgO would be high.



Thus, the outward transport of magnesium ions in the MgO towards the external surface is accompanied by the transport of holes near the external surface and electrons near the alloy film to maintain electrical neutrality. From reaction (4.11), the hole concentration, p , is given as:

$$p = \left[\frac{K}{V_{Mg}''} \right]^{\frac{1}{2}} P_{O_2}^{\frac{1}{4}} \quad (4.13)$$

where K is the equilibrium constant of reaction (4.12).

From charge neutrality, we have:

$$V_{Mg}'' = \frac{1}{2} Al_{Mg}^{\bullet} \quad (4.14)$$

The flux of magnesium ions and the corresponding flux of oxygen is proportional to the hole concentration, p [8]. Following the procedure of Nagelberg et al. [8], the oxygen flux, J , in gm/(cm² sec), at 1373 K, is given as:

$$J \propto \left[\frac{K}{V_{Mg}''} \right]^{\frac{1}{2}} P_{O_2}^{\frac{1}{4}} = 3.15 \times 10^6 P_{O_2}^{\frac{1}{4}} \exp\left(\frac{-310 \times 10^3}{RT}\right) \quad (4.15)$$

where P_{O_2} is the partial pressure of oxygen in atmospheres, R is the gas constant in J/(mole K), and T is the temperature in K. The activation energy for the process is 310 kJ/mole which corresponds to the mobility of holes in MgO (Table 4.1).

Table 4.1 Characteristics of various events in the growth stage.

Event	Oxygen pressure dependence of growth rate	Time dependence of growth rate	Activation energy, kJ/mole	Weight gain rate, mg/cm ² hr, at 1373 K
Magnesium ion flux	$\frac{1}{P_{O_2}}$	Independent of time	310 [8]	17.44
Liquid metal transport	Independent of oxygen pressure	Decreases with time	6.1 [This study]	6415
Oxygen transport through alloy film	Independent of oxygen pressure	Decreases with time	243.6 [This study]	53.17 *
Experimental growth rate	Independent of oxygen pressure	Decreases with time	361 [This study]	12.75

* For an alloy layer thickness of 12 μm , rate of oxygen transport is 13.39 mg/cm²hr.

4.2.1.1 Oxygen Pressure and Time Dependencies

It is seen from equation (4.15) that if the magnesium ion flux through MgO were rate limiting, the oxygen flux (growth rate) would exhibit a $P_{O_2}^{1/4}$ dependence. Thus, equation (4.15) predicts that for a change in oxygen pressure from 21.3 kPa to 85.1 kPa, the weight gain rate would increase by 41.4 %. However, a 6.5 % decrease in the weight gain rate is observed in the average experimental growth rate (Fig. 4.10) when the oxygen pressure is changed from 21.3 kPa to 85.1 kPa. Equation (4.15) also predicts that the oxygen flux should be independent of time. Experimentally, however, the weight gain rate (growth rate) decreases with time. Thus, this mechanism cannot explain either the manner in which the rate varies with time or the observed effect of oxygen pressure on the growth rate. Therefore, this event is ruled out as a rate limiting step.

4.2.2 Liquid Metal Transport

The reaction of Al with oxygen to form Al_2O_3 requires the continued supply of aluminum to the Al alloy film/ Al_2O_3 interface. This is believed to occur via convective flow of metal by wicking (capillary action) through the thickening Al_2O_3 reaction product via the interconnected metal channels. If liquid metal transport through metal channels is rate controlling, the total metal flow through the channels would determine the composite growth rate. Furthermore, the growth rate will show the same dependence on time and P_{O_2} as capillary flow. Therefore, the time and P_{O_2} dependencies of metal flow rate and the corresponding oxygen weight gain rate need to be analyzed. As shown in Appendix D, the weight gain rate per unit area, J , is given by:

$$J = \frac{48 f \rho_{Al} R \gamma_{LV} \cos \theta}{54 \cdot 4 \mu x} = \frac{48 f \rho_{Al}}{54 \cdot 4} \left[\frac{2R \gamma_{LV} \cos \theta}{\mu t} \right]^{\frac{1}{2}} \quad (4.16)$$

where f is the total metal channel area per unit area of the composite, ρ_{Al} is the density of molten aluminum alloy, R is the radius of the channel, γ_{LV} is the surface tension of the molten alloy, θ is the contact angle between the molten alloy and alumina, μ is the viscosity of the molten alloy, x is the thickness of the composite, and t is the time of oxidation.

4.2.2.1 Oxygen Pressure and Time Dependencies

It is seen from equation (4.16) that if liquid metal transport is rate controlling, the growth rate would be independent of oxygen pressure and decrease with time. The experimentally observed oxygen pressure and time dependencies of rate (Fig. 4.10) are qualitatively consistent with that predicted by equation (4.16) for liquid metal transport. If the predicted growth rate is also in good agreement with the experimentally observed growth rate for the Al-5 wt % Mg alloy, transport of liquid metal can then be considered as the rate controlling step in the growth of Al_2O_3/Al composites.

4.2.2.2 Predicted Rate vs the Experimental Growth Rate

The experimental results (Fig. 4.10) indicate that the weight gain rate decreases with time and is independent of the oxygen pressure. These trends are consistent with a situation where the transport of liquid metal controls the oxidation rate (equation (4.16)). However, the calculated weight gain rate needs to be compared with the experimentally observed value to confirm that the transport of liquid metal through the oxide matrix controls the oxidation rate. The value of $\gamma_{LV} \cos \theta$ in equation (4.16) is deduced, as shown in Appendix

D. The data used in the calculation of rate based on equation (4.16) are shown in Table 4.2. For a weight gain of 300 mg, which corresponds to a composite thickness of 0.13 cm, the weight gain rate is predicted to be 6415 mg/(cm² hr) based on equation (4.16), while the experimentally observed weight gain rate is found from Fig. 4.10 to be 10.8 mg/(cm² hr). It is seen that the experimentally observed weight gain rate is about two orders of magnitude lower than the lowest estimate of the predicted weight gain rate (Table 4.1). Furthermore, the theoretical activation energy for the liquid metal transport corresponds to the temperature sensitiveness of viscosity of the liquid aluminum alloy (equation 4.16) and is about 6.1 kJ/mole [11], while the experimentally observed value is 361 kJ/mole. Thus, liquid metal transport through the metal channels does not control the rate of oxidation of Al to Al₂O₃ in the growth stage.

4.2.3 Oxygen Transport Through Alloy Film

4.2.3.1 Flux of Oxygen

The flux of dissolved oxygen from the MgO/Al alloy interface to the Al₂O₃/Al alloy interface can be estimated using Fick's law as:

$$J = \frac{16D_o(X_o^I - X_o^{II})}{LV_m} \quad (4.17)$$

where J denotes the flux of oxygen, D_O is the diffusion coefficient of oxygen in molten aluminum, X_o^I is the mole fraction of dissolved oxygen in the alloy film at the MgO/alloy film interface, X_o^{II} is the mole fraction of dissolved oxygen in the alloy film at the Al₂O₃/alloy film interface, L is the thickness of the alloy film, and V_m is the molar volume of the alloy. The value of X_o^I can be estimated from the MgO/Al alloy equilibrium:

Table 4.2 Data used for the calculation of rate of liquid metal transport.

Property	Symbol	Value	Reference
Total metal channel area per unit area of the composite	f	10^{-5}	[1]
Density of aluminum, kg/m ³	ρ_{Al}	2300	[10]
Channel radius, m	R	3×10^{-6}	[6]
Viscosity of molten aluminum, Ns/m ²	μ	6.21×10^{-4}	[11]
Vapor pressure of magnesium, N/m ²	P_c	5019	[3-4]
Gravitational pressure, N/m ²	P_g	2955 *	[This study]
Capillary pressure, N/m ²	P_v	6.3×10^5	[Appendix A]

* For a composite thickness of 0.00131 m. This corresponds to a weight gain of 3×10^{-4} kg.



where $\underline{\text{Mg}}$ and $\underline{\text{O}}$ denote magnesium and oxygen dissolved in the alloy film respectively.

From reaction (4.18) we get:

$$X_o^I = \frac{\exp(-\Delta G_m^\circ / RT)}{100 \gamma_{\text{Mg}} X_{\text{Mg}}} \quad (4.19)$$

where ΔG_m° is the standard free energy change of reaction (4.18), X_{Mg} is the mole fraction of magnesium in the aluminum alloy, and γ_{Mg} is the activity coefficient for magnesium in liquid aluminum. A similar expression can be derived for X_o^{II} from the $\text{Al}_2\text{O}_3/\text{Al}$ alloy equilibrium :



$$X_o^{II} = \frac{\exp(-\Delta G_A^\circ / 3RT)}{100 [\gamma_{\text{Al}} (1 - X_{\text{Mg}})]^{\frac{2}{3}}} \quad (4.21)$$

where ΔG_A° is the standard free energy change of reaction (4.20) and γ_{Al} is the activity coefficient of aluminum in the alloy. It can be seen from equations (4.19) and (4.21) that an increase in the Mg concentration leads to a decrease in the dissolved oxygen concentration at the MgO/alloy interface and an increase in the dissolved oxygen concentration at the Al_2O_3 /alloy interface. As a result, the rate of oxygen transport across the alloy film decreases (Equations 4.17, 4.19 and 4.21). Thus, with increasing Mg concentration in the alloy film, oxygen transport across the alloy film becomes an important transport step in the growth stage of directed oxidation of Al-Mg alloys.

4.2.3.2 Oxygen Pressure and Time Dependencies

If the Al-Mg alloy in the composite channels attains equilibrium with $\text{Al}_2\text{O}_3/\text{MgAl}_2\text{O}_4$ [8,13,14], the equilibrium alloy composition is 0.19 mol % Mg at 1373 K based on the available thermodynamic data [3-4]. The Al-Mg alloy wicks through the metal channels, reacts with the dissolved oxygen and forms fresh alumina epitaxially on the existing alumina. The solubility limit for Mg in Al_2O_3 is 0.012 mol % at 2073 K [15] and the solubility decreases rapidly with decreasing temperature. As the aluminum in the alloy gets oxidized to alumina, the concentration of magnesium in the alloy film tends to increase to values higher than 0.19 mol % Mg. The build up of magnesium concentration in the alloy film continues with time unless magnesium back diffusion down the metal channels into the bulk alloy occurs at appreciable rates. Since liquid metal transport through the channels to the reaction interface is fairly rapid, the solute enrichment is likely to continue. It can be seen from equations (4.19) and (4.21) that when the magnesium concentration in the alloy increases, the equilibrium oxygen concentration at the MgO/alloy interface decreases. At the same time, the dissolved oxygen concentration at the Al_2O_3 /alloy interface increases. Thus, the increase of magnesium concentration in the alloy film leads to a lower oxygen concentration gradient across the film. As a result, the rate of oxygen transport in the near surface alloy layer decreases with time. Furthermore, it is observed from equation (4.17) that the rate is independent of oxygen pressure. These trends are consistent with the experimentally observed dependence of growth rate on time and oxygen pressure.

As the growth stage progresses, continued Mg enrichment in the near surface alloy film can lead to the precipitation of MgAl_2O_4 spinel, between the MgO and the underlying metal, as observed by several investigators [2,7,16]. MgAl_2O_4 forms beneath the MgO rather than on top of Al_2O_3 due to nucleation considerations [16]. The spinel subsequently demixes

due to the presence of the oxygen gradient across the alloy film, exposing the film to MgO. A fresh nucleation of Al_2O_3 occurs on the existing alumina layer [7,16]. This is consistent with the proposed mechanism for the growth stage. The oxygen required for alumina formation is supplied by dissociation of MgO. The observed continuing decrease in the growth rate with time [2] is consistent with our proposed model.

4.2.3.3 Predicted Rate vs the Experimental Growth Rate

The data used in equation (4.17) for the calculation of the maximum rate of oxygen transport are presented in Table 4.3. Note that the oxygen transport rate would be maximum at the start of the growth stage when the Mg concentration in the alloy film corresponds to about 0.19 mol %, i.e., the Mg concentration in the alloy corresponding to the $\text{MgAl}_2\text{O}_4/\text{Al}_2\text{O}_3$ equilibrium at 1373 K. The maximum rate of oxygen transport at 1373 K is estimated to be 53.17 $\text{mg}/(\text{cm}^2\text{hr})$. This value is within an order of magnitude of the experimentally observed maximum growth rate of 12.75 $\text{mg}/(\text{cm}^2\text{hr})$. The estimated rate of oxygen transport would be exactly equal to the experimental growth rate for a metal layer thickness of about 12 μm . This value of thickness of the metal layer is higher than the values of 1 to 3 μm reported by Antolin et al. [6]. However, this value is probably not unreasonable in view of the uncertainties involved in the calculation, and the possibility that the metal layer thickness during the reaction may be higher than that observed after cooling to room temperature. The experimentally determined rate values are consistent with the possibility that oxygen transport through the metal layer is the rate limiting step in the composite growth stage.

Table 4.3 Data used in the calculation of oxygen transport through the near surface alloy layer.

Property	Symbol	Value	Reference
Diffusivity of oxygen in molten aluminum*, m ² /sec	D_o	1.3×10^{-8}	[11]
Thickness of alloy layer, m	L	3×10^{-6}	[7]
Oxygen concentration in the alloy film at the MgO/film interface**, mole fraction	X_o^I	2.5×10^{-5}	[3,4,17]
Oxygen concentration in the alloy film at the Al ₂ O ₃ /film interface**, mole fraction	X_o^{II}	1.1×10^{-6}	[3,4,17]

* Tracer diffusivity of oxygen in molten aluminum is approximated by the diffusivity of aluminum in molten aluminum at 1373 K.

** Oxygen concentrations calculated at 1373 K for a Mg concentration of 0.19 mol % in the alloy film.

4.2.3.4 Activation Energy for Oxygen Transport

Since the oxygen concentration at the MgO/alloy film interface is much higher than the dissolved oxygen concentration at the Al₂O₃/alloy film interface (Table 4.3), equation (4.17) can be approximated as:

$$J = \frac{16D_o X_o^1}{LV_m} \quad (4.22)$$

Using equation (4.19) in (4.22) we get:

$$J = \frac{16D_o \exp(-\Delta H_m^0 / RT) \exp(\Delta S_m^0 / R)}{100\gamma_{Mg} X_{Mg} LV_m} \quad (4.23)$$

where ΔH_m^0 is the standard enthalpy change for reaction (4.18) and ΔS_m^0 is the standard entropy change for reaction (4.18). The activation energy for oxygen diffusion in liquid aluminum is small (6.1 kJ/mole) [11]. Therefore, the variation of D_o is insignificant over the temperature range of 1373 - 1450 K examined in this study. The activation energy for oxygen transport is deduced from equation (4.23) as ΔH_m^0 , and is equal to 243.6 kJ/mole [3,4,17]. Thus, the observed activation energy and weight gain rate in the growth stage are in fair agreement with that predicted for oxygen transport through the near surface alloy layer. Considerations of the liquid metal transport through channels in the composite or magnesium ion transport through the MgO layer cannot explain the observed oxidation behavior. The predictions of the oxygen transport model are consistent with the observations of Vlach et al. [2] and Xiao et al. [13] who reported parabolic oxidation kinetics in the growth stage and an activation energy of around 270 kJ/mole. Thus, the transport of oxygen through the near surface alloy layer is the rate controlling event in the

growth stage of directed oxidation of Al-Mg alloys in the temperature range 1373 to 1450 K.

The proposed model for growth stage kinetics of Al-Mg alloys can be used to predict the effect of additional alloying elements on the growth rate. It is known that Ni additions to Al-Mg alloys refines the composite microstructure [18]. The effect of Ni additions on the composite growth rate can be predicted with the help of the oxygen transport model. There is a strong interaction between Ni and Al as indicated by the highly negative heat of formation of Ni-Al intermetallics [12]. Therefore, Ni additions to the Al-Mg alloy would be expected to reduce the activity coefficient of Al in the melt. On the other hand, Ni does not form highly stable intermetallics with Mg [12]. As a result, Ni would not be expected to influence the Mg activity coefficient in the Al melt. Therefore, it can be seen from equations (4.17), (4.19) and (4.21), that Ni additions to an Al-Mg alloy would reduce the growth rate, in addition to refining the composite microstructure [18].

4.3 Growth Stage Kinetics of Al-Mg-Si Alloys

Figure 4.13 is a plot of weight gain vs time at various temperatures (1393-1612 K) for an oxygen pressure of 93.3 kPa [19]. The weight gain rates are plotted as a function of temperature in Fig. 4.14 and the activation energy is found to be 218 kJ/mole. Weight gain rates were also measured at different oxygen pressures at a temperature of 1612 K (Table 4.4). The experimental results indicate that the oxidation rate in the growth stage is independent of time and varies as $P_{O_2}^{\frac{1}{4}}$. These trends are consistent with a situation where electronic transport through MgO controls the oxidation rate. This is consistent with the observation of Nagelberg et al. [8] that electronic transport controlled the growth rate of Al-Mg-Si alloys. Several important questions arise from the analysis of the data. How does

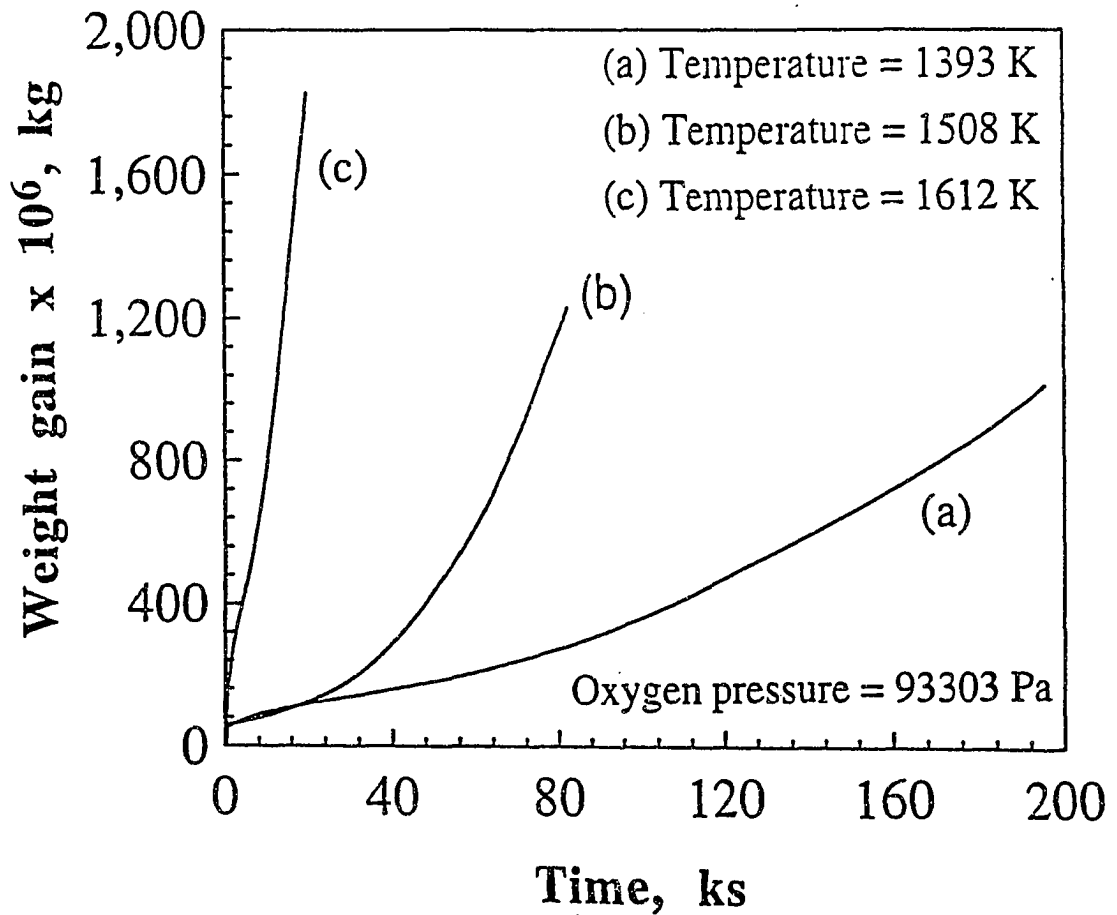


Fig. 4.12 Weight gain vs time for the Al-Mg-Si alloy at different temperatures: (a) 1393 K, (b) 1508 K, and (c) 1612 K. The total pressure, oxygen pressure and the total gas flow rate were maintained constant at 93303 Pa, 93303 Pa, and 8333 mm³/s STP, respectively.

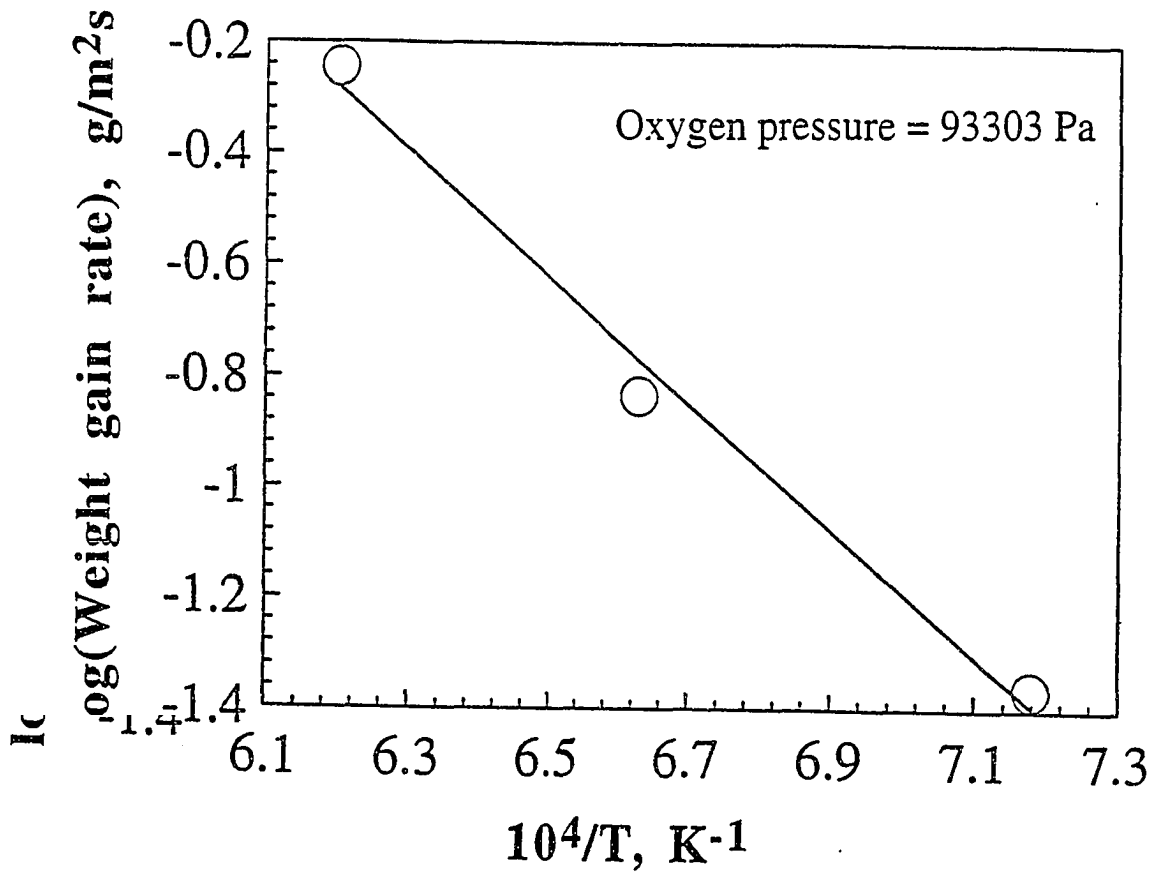


Fig. 4.14 Weight gain rate vs temperature for Al-Mg-Si alloy for an oxygen pressure of 93303 Pa. The total pressure and the total gas flow rate were maintained constant at 93303 Pa and 8333 mm³/s STP, respectively.

Table 4.4 Average growth rate of Al-Mg-Si alloy as a function of oxygen pressure at 1612 K.

Oxygen pressure, kPa	Growth rate, g/m ² s
93.3	0.567
46.6	0.522
23.3	0.439

silicon additions to Al-Mg alloy shift the oxidation mechanism from oxygen transport through the near surface alloy layer to electronic transport through MgO?

4.3.1 Influence of Silicon on Oxygen Transport through the Alloy Layer

Formation of Mg-Si clusters in binary Mg-Si liquid solutions [20] indicates that silicon additions to Al-Mg alloys could affect the activity of magnesium. The change in the activity of magnesium in the near surface alloy layer, observed in directed oxidation, would affect the solubility of oxygen at the MgO/Al alloy interface (Eqn. 4.19). Silicon could also affect the Al activity in the alloy layer. Thus silicon additions are expected to alter the oxygen solubility gradient across the alloy film and thereby affect the rate of oxygen transport (Eqn. 4.17). The effect of silicon additions on the activities of Mg and Al in the near surface alloy layer can be estimated from Al-Mg-Si ternary liquid solution thermodynamics. Al-Mg-Si liquid solution thermodynamics is estimated following the method outlined in the "Procedures" section. Figures 4.15 and 4.16 show the effect of Si on the oxygen solubility gradient across the alloy film for Al-Mg and Al-Mg-Si alloys respectively. It can be observed that the presence of silicon in the melt reduces the oxygen solubility gradient in the alloy film from the MgO/Al alloy interface to the Al₂O₃/Al alloy interface. For the Al-Mg alloy used in this study, SiO₂ additions result in a silicon content in the alloy of 3.3 mol %. Thermodynamic calculations indicate that for a Mg composition of 5.5 mol %, silicon addition of 3.3 mol % reduces the activity of Mg in Al-Mg-Si solution by a factor of 0.67 at a temperature of 1393 K. However, silicon additions do not affect the activity of Al in Al-Mg-Si significantly. Equation (4.23) indicates that the rate of oxygen transport is inversely proportional to the activity of Mg in the near surface alloy layer. Thus, for the alloy used in this study, silicon additions accelerate the rate of oxygen transport by a factor of 1.5 at

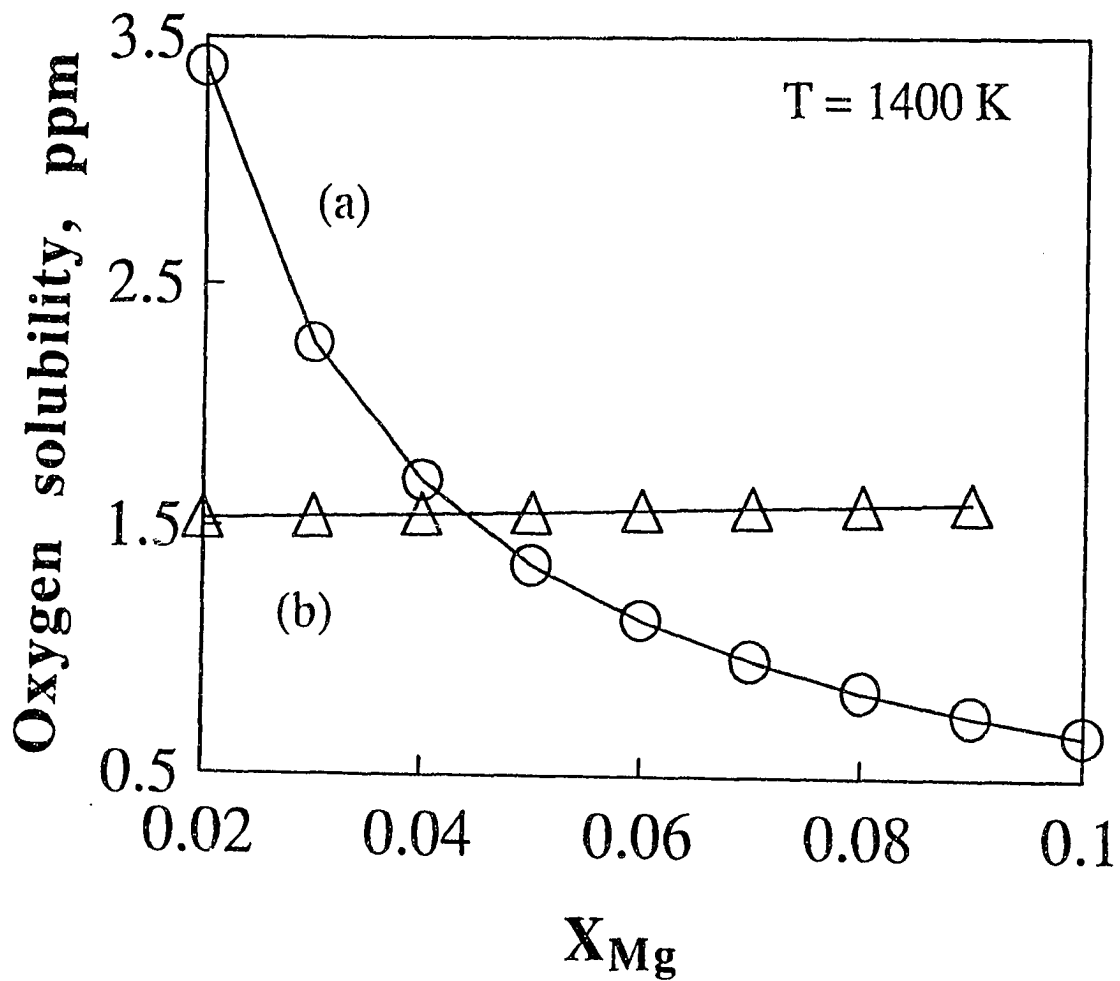


Fig. 4.15 Calculated equilibrium oxygen solubility in the Al-Mg alloy film, at 1400 K, at (a) the MgO/alloy film interface, and (b) the Al_2O_3 /alloy film interface, for varying magnesium contents.

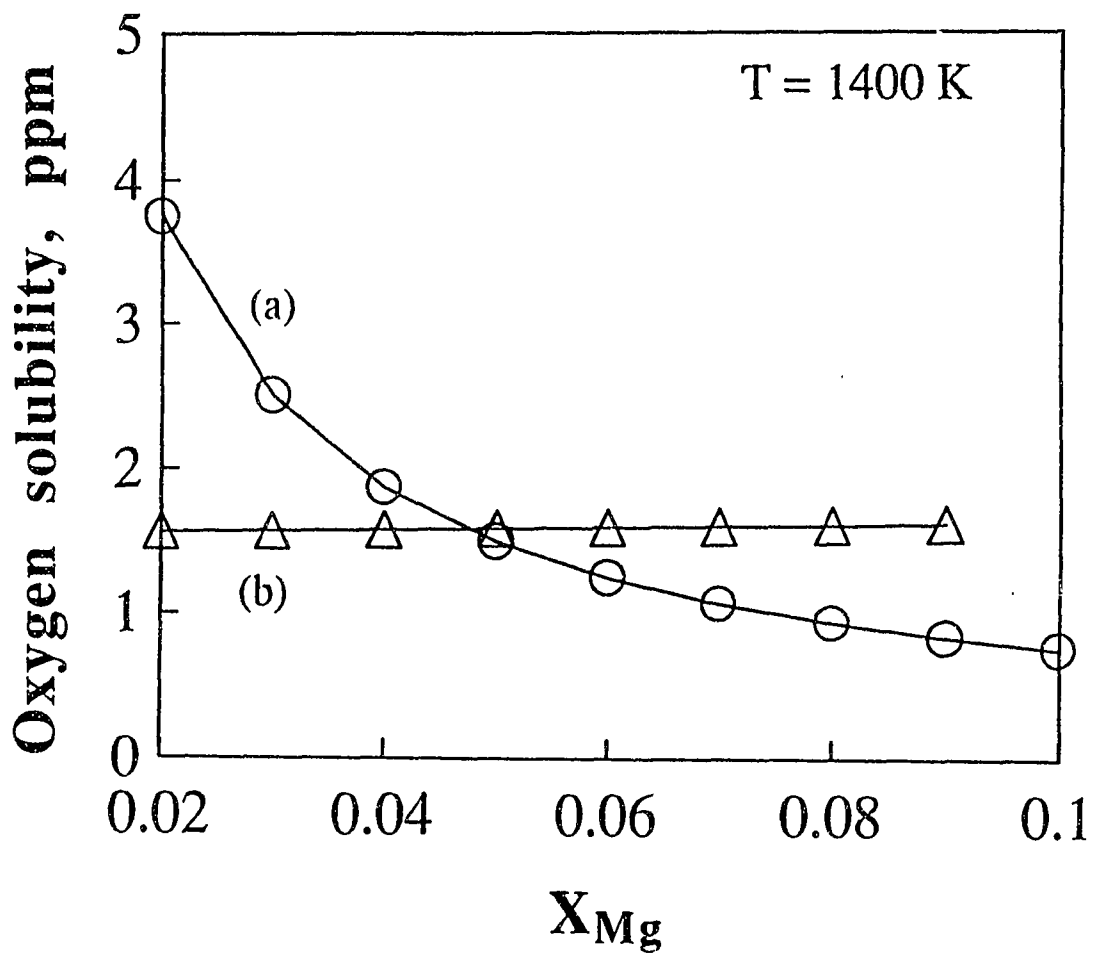


Fig. 4.16 Calculated equilibrium oxygen solubility in the Al-Mg-3.3 mol% Si alloy film, at 1400 K, at (a) the MgO/alloy film interface, and (b) the Al₂O₃/alloy film interface, for varying magnesium contents.

1393 K. As a result of the enhanced oxygen transport, this step becomes less important in the oxidation of Al-Mg-Si alloys than that of Al-Mg alloys.

4.3.2 Influence of Silicon on Electronic Transport through MgO

Since silicon is present in the melt, a small proportion would be incorporated into the MgO which is present on top of the near surface alloy melt. The dissolution of silicon in MgO would increase the concentration of magnesium ion vacancies according to the equation:

$$V_{\text{Mg}}'' = \frac{1}{2} \text{Al}_{\text{Mg}}' + \text{Si}_{\text{Mg}}'' \quad (4.24)$$

where Si_{Mg}'' represents the dissolved silicon concentration in MgO. It is seen from equation (4.24) that silicon additions increase V_{Mg}'' . Since the hole concentration, p , is inversely proportional to V_{Mg}'' (Eqn. (4.13)) silicon additions would, thus, decrease p . It is known that the rate of electronic transport in MgO is proportional to the hole concentration, p (Eqn. 4.15) [8]. As a result, silicon additions to Al-Mg alloys decrease the rate of electronic transport through MgO.

Thus, it is seen that silicon additions to Al-Mg alloys increase the rate of oxygen transport through the alloy film and decrease the rate of electronic transport through MgO, respectively. As a result of the reduced rate of electronic transport through MgO, this step becomes more important in the oxidation of Al-Mg-Si alloys than that of Al-Mg alloys. The experimental results on the oxygen pressure and time dependencies of the growth rate of Al-Mg-Si alloys are consistent with the characteristics of an oxidation reaction controlled by electronic transport through MgO i.e. growth rate independent of time and proportional to $P_{\text{O}_2}^{\frac{1}{4}}$. Thus, the addition of 3.3 mol % Si to Al-5.5 mol % Mg shifts the oxidation

mechanism from oxygen transport through the near surface alloy layer to electronic transport through MgO.

4.4 Metal Distribution in Alumina/Aluminum Composites

4.4.1 Nature of Metal Distribution

In order to understand the distribution of aluminum metal in the $\text{Al}_2\text{O}_3/\text{Al}$ composite, electrical conductivities of $\text{Al}_2\text{O}_3/\text{Al}$ and sintered Al_2O_3 -4% MgO were compared. The matrix of the $\text{Al}_2\text{O}_3/\text{Al}$ composite typically has a few percent of spinel [21] and some magnesium dissolved in the alumina [16]. Thus, the sintered Al_2O_3 -4% MgO pellet is considered to be more representative of the composite matrix than a pure alumina pellet. The measured conductivities at various temperatures are presented in Fig. 4.17. The results indicate that the conductivity of the $\text{Al}_2\text{O}_3/\text{Al}$ composite is six to seven orders of magnitude higher than that of sintered Al_2O_3 -MgO pellet. The $\text{Al}_2\text{O}_3/\text{Al}$ composite differs from the sintered Al_2O_3 -MgO pellet primarily in that the composite has some aluminum metal in it. Thus, the observed higher conductivity of $\text{Al}_2\text{O}_3/\text{Al}$ composite can be attributed to the presence of aluminum, either as a random dispersion or in the form of interconnected channels in the alumina matrix.

The conductivity of a sintered Al_2O_3 -4% MgO pellet containing a random dispersion of uniform sized aluminum spheres (20 vol %), σ , can be estimated, from the conductivity of the sintered oxide pellet without the metal dispersion, σ_m , using Maxwell's relation [22-23]:

$$K_m = \frac{\sigma}{\sigma_m} = \frac{K_d + 2 - 2f(1 - K_d)}{K_d + 2 + f(1 - K_d)} \quad (4.25)$$

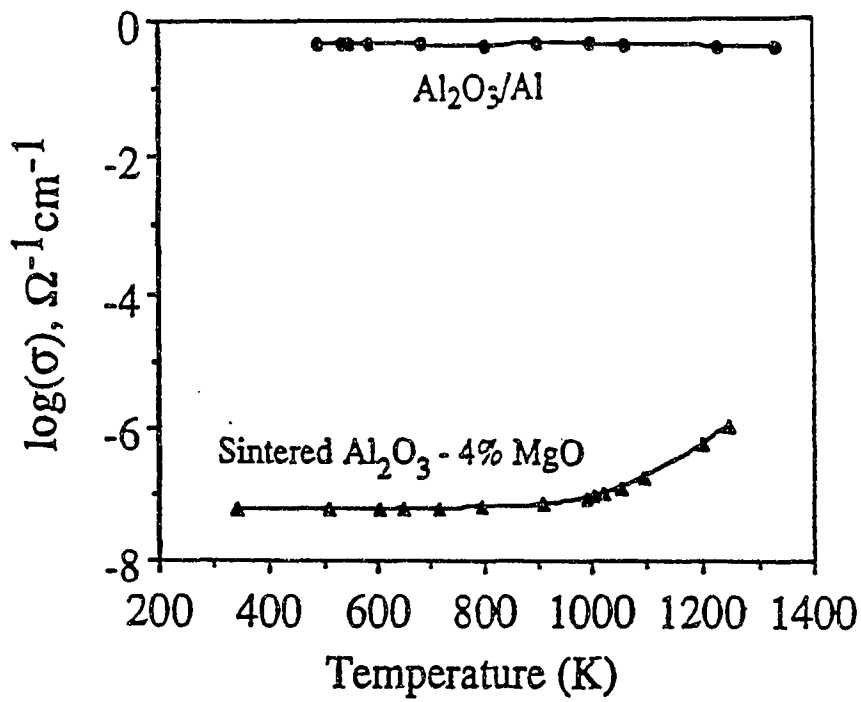


Fig. 4.17 Electrical conductivity of $\text{Al}_2\text{O}_3/\text{Al}$ composite and sintered Al_2O_3 -4 wt% MgO at various temperatures. Measurements were made in argon at 1-atm pressure and a gas flow rate of 500 sccm.

where

$$K_m = \frac{\text{conductivity of the oxide medium with dispersion}}{\text{conductivity of the oxide medium without dispersion}} \quad (4.26)$$

$$K_d = \frac{\text{conductivity of the dispersed phase (aluminum)}}{\text{conductivity of the oxide medium without dispersion}} \quad (4.27)$$

and f is the volume fraction of the dispersed phase, aluminum in this case. Since the conductivity of aluminum [10] is 12 orders of magnitude greater than the conductivity of sintered $\text{Al}_2\text{O}_3\text{-MgO}$, i.e. $K_d \gg 1$, equation (4.25) reduces to

$$K_m = \frac{(1 + 2f)}{(1 - f)} \quad (4.28)$$

Breval et al. [21] have reported that alumina matrix composites produced by directed metal oxidation of aluminum alloys contain up to 20 vol % aluminum. Equation (4.28) predicts that a random dispersion of 20 vol % aluminum in sintered $\text{Al}_2\text{O}_3\text{-MgO}$ would enhance the conductivity by a factor of 1.75. Thus, a random distribution of aluminum in the composite cannot explain the six to seven orders of magnitude higher conductivity of $\text{Al}_2\text{O}_3/\text{Al}$ composite compared to that of sintered $\text{Al}_2\text{O}_3\text{-MgO}$. The result indicates the presence of aluminum as continuous channels extending through the entire thickness of the $\text{Al}_2\text{O}_3/\text{Al}$ composite. These metal channels provide a low resistance electrical path in an otherwise high resistance oxide matrix, resulting in the observed high conductivity of the composite.

Since $\text{Al}_2\text{O}_3/\text{Al}$ composites have continuous aluminum channels, the composites should have high electrical conductivity. It is shown in Appendix E that if the aluminum

channels in the composite are assumed to be of roughly equal length and cross-sectional area, the conductivity of the composites, σ_c , is given by:

$$\sigma_c = \frac{\sigma_{Al} f_m}{\tau} \quad (4.29)$$

where σ_{Al} is the conductivity of aluminum. It is observed from Fig. 4.17 that the measured conductivity of a Al_2O_3/Al composite sample at 1000 K is $4.3 \times 10^{-1} \text{ ohm}^{-1} \text{ cm}^{-1}$. The conductivity of liquid aluminum at 1000 K is $4.0 \times 10^4 \text{ ohm}^{-1} \text{ cm}^{-1}$ [10]. Thus, there is a five orders in magnitude difference in the conductivity of Al_2O_3/Al composite and aluminum. If the metal channels are assumed to be straight, i.e., $\tau = 1$, the fractional metal channel area, f_m , is found to be 1.1×10^{-5} . Since the estimated area fraction is unrealistically low, the assumptions that the channels are straight and all channels extend over the entire thickness of the Al_2O_3/Al composite must be examined closely. In the Al_2O_3/Al composite, the metal is present as tortuous channels and not all channels extend through the entire thickness of the composite. Assuming a very high tortuosity factor of 100, a fractional channel area, f_m , of 1.1×10^{-3} is obtained. Thus, the tortuosity of the channels alone cannot explain the low area fraction. Therefore, the low conductivity of the composite in comparison with aluminum must be attributed to a composite structure where only a small fraction of the metal channels extend through the entire thickness of the composite.

A comparison of the conductivity of the composite and aluminum metal at 500 K yields a fractional channel area of 2.3×10^{-6} which is about five times lower than that calculated at 1000 K. This decrease in the fractional channel area with decrease in

temperature can be explained on the basis of the large difference in the thermal expansion coefficients of aluminum and alumina. The coefficients of linear thermal expansion of solid and liquid aluminum are $30 \times 10^{-6} \text{ K}^{-1}$ and $41 \times 10^{-6} \text{ K}^{-1}$ [24] respectively, while that of alumina is $10 \times 10^{-6} \text{ K}^{-1}$ [28]. Furthermore, aluminum shrinks by 6% on solidification [24]. On cooling, this volume shrinkage and the difference in the coefficients of thermal expansion of aluminum and alumina can cause (a) reduction in the cross-sectional area of the channels and (b) discontinuities in the metal channels reducing the number of the channels that extend through the entire thickness of the composite. Although the conductivity of aluminum increases with decrease in temperature, the effect is compensated, at least in part, by the reduction in the number and cross-sectional area of the channels. The observed insensitivity of the conductivity with changes in temperature of the $\text{Al}_2\text{O}_3/\text{Al}$ composite is consistent with these two opposing effects.

4.4.1.1 Activation Energy for Diffusion

Once the bulk metal is completely exhausted, further oxidation of the metal in the channels would be expected to occur by ionic diffusion through the Al_2O_3 matrix. The determination of the activation energy of this process and the nature of the dominant charge carrier in the oxide matrix is therefore of interest. The presence of continuous aluminum channels in the $\text{Al}_2\text{O}_3/\text{Al}$ composites precludes the determination of the dominant charge carrier in the oxide matrix from the measured electrical conductivity of the composite. Since the matrix in the $\text{Al}_2\text{O}_3/\text{Al}$ composite is similar in chemical composition to the sintered Al_2O_3 -4% MgO pellet, the nature of the charge carrier in the alumina matrix can be examined using the electrical conductivity data for sintered Al_2O_3 -4% MgO presented in Fig. 4.17. Conductivity data of sintered Al_2O_3 -4% MgO,

in the temperature range 1080 K to 1250 K, were used to determine the activation energy for the diffusion of the dominant charge carrier. At lower temperatures, because of the very low bulk conductivity of Al_2O_3 -4% MgO, surface and/or gas phase conduction can result in inaccurate bulk conductivities [26]. Hence, meaningful activation energy data can not be derived from the conductivities at temperatures lower than 1000 K. Figure 4.18 is a plot of $\ln\sigma T$ vs $1000/T$, commonly used to determine the activation energy for the diffusion of the dominant charge carrier [27]. An activation energy of 1.36 eV for the diffusion of the dominant charge carrier in Al_2O_3 -4% MgO is obtained from the slope of the line in Fig. 4.18. The measured activation energy of 1.36 eV is in fair agreement with a value of 1.6 eV obtained by Yee et al. [28] for a MgO doped polycrystalline Al_2O_3 sample and represents the activation energy for diffusion through Al_2O_3 .

Yee et al. [28] have shown that in the temperature range of interest and for $P_{\text{O}_2} < 10^{-4}$ atm, the transference number of ions, i.e. the ratio of the ionic conductivity and the total conductivity, is close to unity. Hence, this activation energy would correspond to the activation energy of diffusion of an ionic species. The magnesium in sintered Al_2O_3 -4% MgO would be in saturated solid solution in alumina and hence extrinsic ionic defects are expected to dominate. Therefore, the observed activation energy represents the migration energy of the dominant extrinsic defect in sintered Al_2O_3 -4% MgO. Several investigators [29-37] have attempted to identify the nature of the dominant extrinsic defect in acceptor (Mg, Fe) dominated Al_2O_3 . However, there is significant controversy as to whether aluminum ion interstitials [30-33] or oxygen ion vacancies [34-37] are the dominant extrinsic defects. The activation energy, for the diffusion of the dominant charge carrier in Al_2O_3 -4% MgO, measured in this study could be

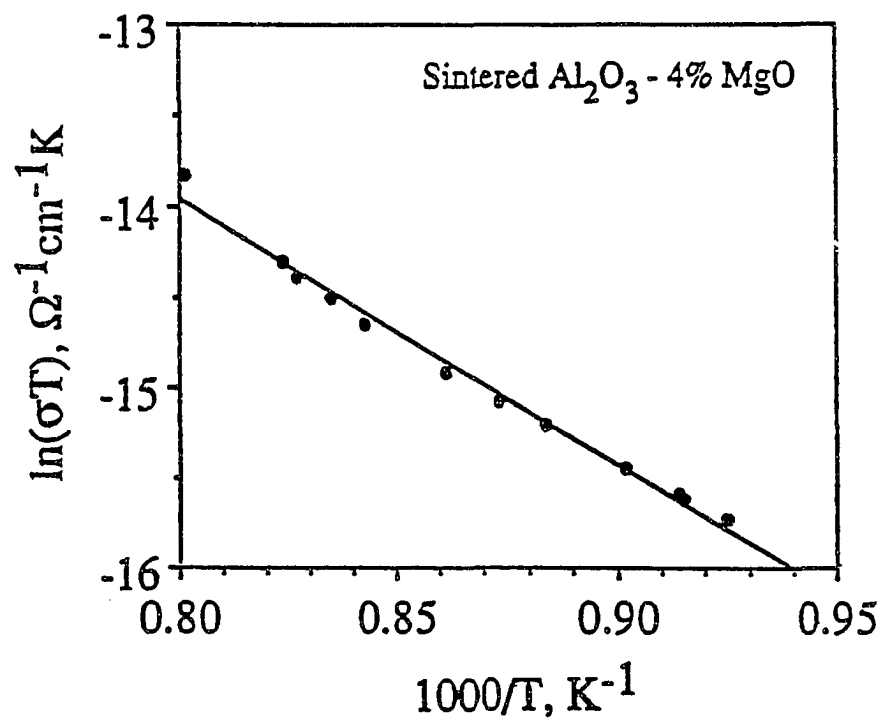


Fig. 4.18 Arrhenius plot of $\ln(\sigma T)$ vs $1000/T$ for determination of the activation energy for the diffusion of the dominant charge carrier in sintered Al_2O_3 -4 wt% MgO.

interpreted as the migration energy of either aluminum ion interstitials or oxygen ion vacancies.

4.4.2 Dependence of Metal Distribution in Al₂O₃/Al Composites on Growth Temperature

Electrical conductivities of Al₂O₃/Al composites, grown at different temperatures, are shown in Figure 4.19 [38]. The conductivity measurements were carried out at 298 K. It can be seen that the electrical conductivity and, correspondingly, the degree of interconnection of the aluminum channels, decrease with increase in the growth temperature. SEM micrographs of the composites, grown at different temperatures, are shown in Figure 4.20. EDS (Energy dispersive X-ray spectroscopy) analysis indicates that the dark gray areas are essentially Al, while the light gray areas are Al₂O₃. The black areas are pores. It is observed from Fig. 4.20 that the number of pores increases with increasing growth temperature. This is consistent with the observations of Aghajanian et al. [39]. The amount of metal in the composites was measured by image analysis of the micrographs. Table 4.5 shows that the volume fraction of metal in the composite decreases with increasing growth temperature. It is noted from Table 4.5 that the proportion of metal in the Al₂O₃/Al composites could vary by as much as $\pm 6\%$. A similar scatter was observed by Manor et al. [40]. Thus, it is observed that both the amount of metal and the extent of metal interconnection decrease with increasing growth temperature. These experimental observations can be rationalized based on interfacial energy considerations as discussed below.

As shown in Figure 4.21, when Al metal penetrates through a alumina grain boundary and forms a channel, an alumina/alumina interface (grain boundary) is replaced by two

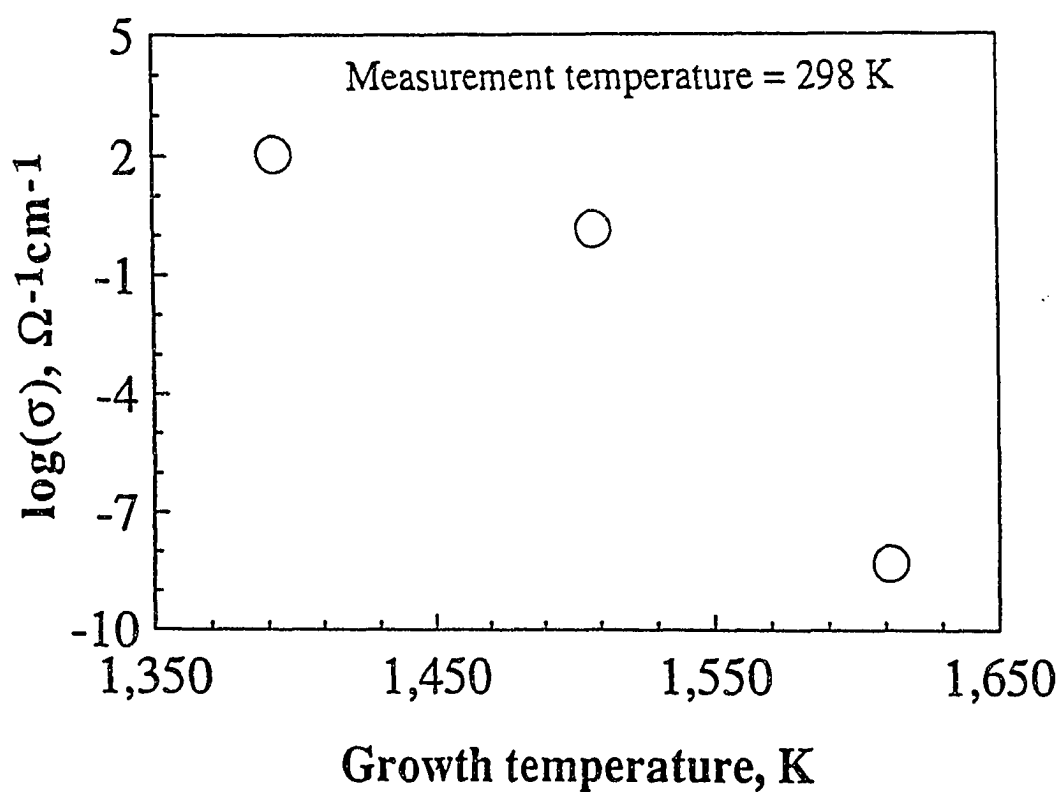


Fig. 4.19 Electrical conductivity of $\text{Al}_2\text{O}_3/\text{Al}$ as a function of the growth temperature. Measurements were made at 298 K in argon at 1-atm pressure and a gas flow rate of 500 sccm.

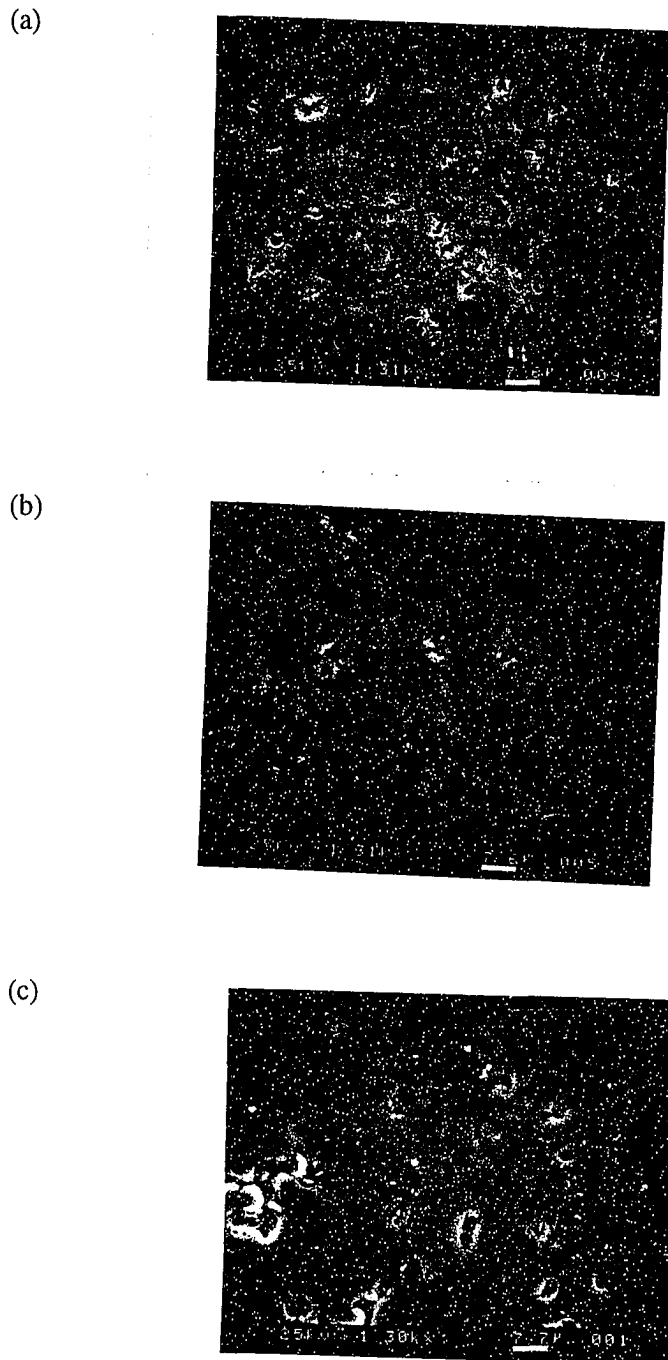


Fig. 4.20 SEM micrographs showing the general microstructural features of composites produced by melt oxidation of Al-5056 alloy at different temperatures (a) 1393 K, (b) 1508 K, and (c) 1612 K.

Table 4.5 Volume fraction of Al metal in Al₂O₃/Al composites as a function of the growth temperature.

Growth temperature, K	Volume fraction of metal, %
1393	19.5 ± 6
1508	14.0 ± 4.5
1612	7.7 ± 3

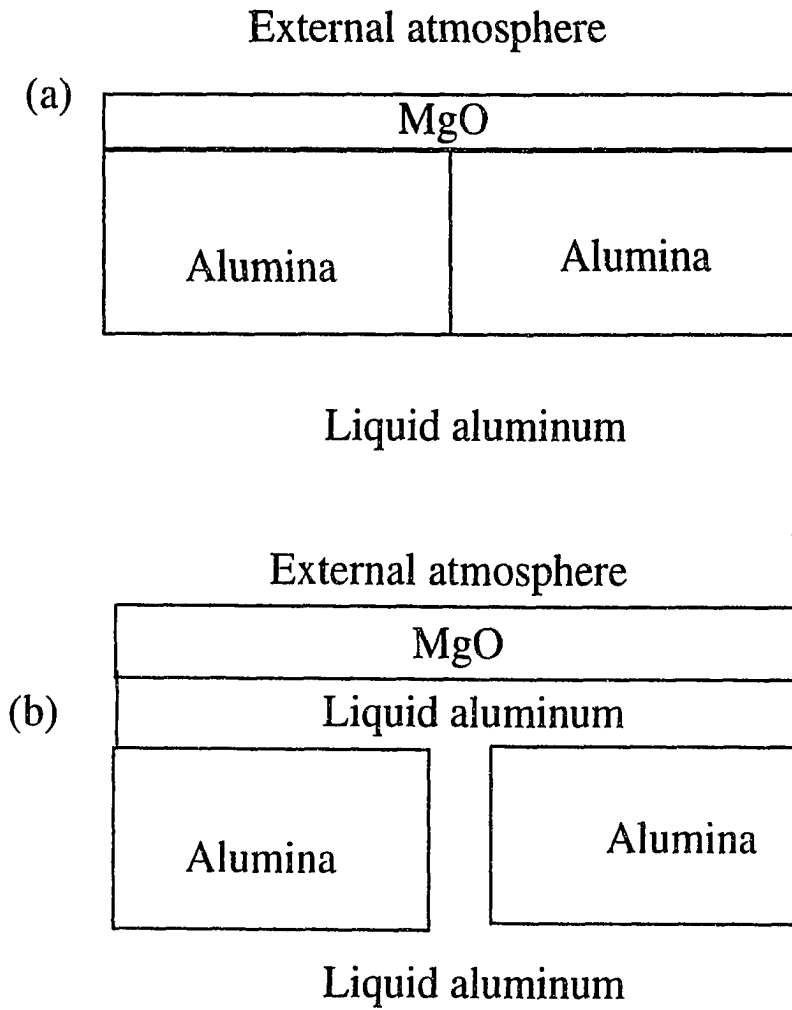


Fig. 4.21 Schematic description of condition for formation of metal channels. (a) Metal channels cannot form ($\gamma_{SS} < 2\gamma_{SL}$). (b) Metal channels can form in the grain boundary ($\gamma_{SS} > 2\gamma_{SL}$).

liquid aluminum/alumina interfaces. For this microstructure to be stable, it is necessary that:

$$\gamma_{SS} > 2\gamma_{SL} \quad (4.30)$$

where γ_{SS} is the energy of a grain boundary of alumina and γ_{SL} is the interfacial energy between the molten aluminum and the solid alumina. While interfacial energies are less dependent on orientation, the energy of a grain boundary generally increases with increasing mis-orientation [42]. Equation (4.30) indicates that Al_2O_3 grains in the composite could be interconnected along low angle grain boundaries. In addition, metal channels would separate Al_2O_3 grains along high angle grain boundaries. Indeed, transmission electron microscopy studies [21,43] reveal that low angle Al_2O_3 - Al_2O_3 grain boundaries are free of second phases. It was also observed by Newkirk et al. [42] that high-angle grain intersections contained thin channels of Al metal separating neighboring Al_2O_3 crystals rather than a high angle Al_2O_3 - Al_2O_3 grain boundary. Since Al_2O_3 crystals produced by directed oxidation grow with their c-axis nearly parallel to the growth direction [21], grain boundaries nearly parallel to the c-axis must be considered. As the number of such boundaries that satisfy equation (4.30) increase, the number of metal channels and correspondingly, the electrical conductivity of the $\text{Al}_2\text{O}_3/\text{Al}$ composite would increase. Values for γ_{SL} can be obtained from experimental data [44-45]. Several grain boundary orientations are possible for which the grain boundary is nearly parallel to the c-axis [46]. However, experimental values for all these orientations is not available. For a $\Sigma 11$ grain boundary in alumina ($[2110]$ 35.2° tilt boundary mis-orientation), experimental value of γ_{SS} is available. High resolution

transmission electron microscopy studies of Hoche et al. [47] reveal that γ_{SS} is 1.7 J/m² at 1893 K. By extrapolation, γ_{SL} is 0.549 J/m² at a temperature of 1893 K [44-45]. Thus, at 1893 K, it can be seen that $\gamma_{SS} > 2 \gamma_{SL}$ for the $\Sigma 11$ boundary, and hence, metal would be expected to penetrate along $\Sigma 11$ boundary.

The experimentally observed changes in the electrical conductivity with growth temperature can be explained if metal interconnection decreases with temperature i.e., γ_{SS} decreases faster relative to $2 \gamma_{SL}$, for a number of grain boundaries with increase in growth temperature. Thus, more ceramic-ceramic grain boundaries would become stable as the growth temperature increases. The decrease in the number of alumina grain boundaries through which aluminum can penetrate would explain the decrease in the amount and interconnection of metal in the composite with increasing growth temperature. However, energy data for various grain boundaries in alumina (parallel to the c-axis) and their dependence on temperature are not available. It is proposed that γ_{SS} decreases faster than $2 \gamma_{SL}$ with increase in temperature though experimental data on grain boundary energies in alumina are yet to be obtained. Similar interfacial energy arguments have been used to explain the temperature dependence of grain boundary microstructures in diverse systems such as WC-Co, WC-Cu, Si₃N₄-glass and SiC-Si [48-50].

4.5 Oxidation into Preforms

The weight gain vs time curves for directed oxidation of the Al - 5 wt% Mg alloy (Al-5056 alloy) into alumina preforms of varying particle sizes are depicted in Fig. 4.22.

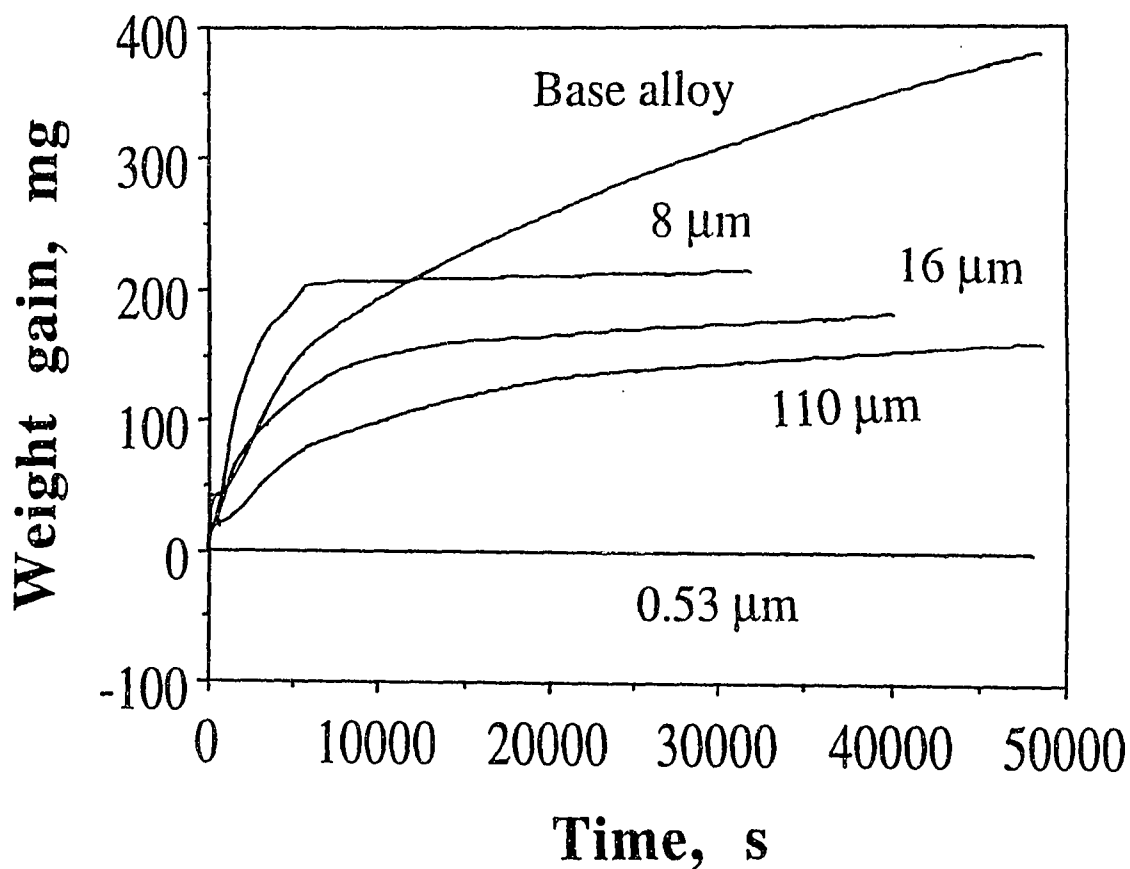


Fig. 4.22 Weight gain vs time for directed oxidation of Al-Mg alloy at 1450 K into Al_2O_3 preforms of different particle sizes. The weight gain vs time plot for the base alloy is also shown. The oxygen pressure, total pressure and the total gas flow rate were maintained constant at 85092 Pa, 93303 Pa and 8333 mm^3/s STP, respectively.

The weight gain vs time plot for the base alloy and for the composites containing alumina preforms were normalized by the net cross-sectional area normal to the macroscopic growth direction (Fig. 4.23). For the base alloy, without any preform, this area corresponds to the internal cross-sectional area of the crucible (1.54 cm^2). For the case of the preforms, this area essentially corresponds to the void space between the alumina particles. For random loose packing, the void area fraction is ≈ 0.45 [51]. Assuming random loose packing, for the case of the preforms, the cross-sectional area of the void space is $0.45 \times 1.54 = 0.693 \text{ cm}^2$. If the preform had no effect other than to reduce the net area available for growth of the reaction product, the normalized weight gain curves in Fig. 4.23 should, in principle overlap. However, it is clear that the composites grown into Al_2O_3 preforms (except for preform of $0.53 \text{ }\mu\text{m}$ particle size) exhibit a weight gain per unit area, corrected for the presence of particles, higher than that of the base alloy alone. Thus, the differences in the oxidation rates of Al-Mg alloys, with and without preforms, cannot be completely attributed to the reduction in the melt area exposed to oxidation. The differences in the normalized weight gain vs time curves in Fig. 4.23 are analyzed below.

4.5.1 Initial Stage

The weight gain vs time plots in the initial stage, for oxidation of the base alloy in free space, and oxidation of the base alloy into preforms, are shown in Fig. 4.24. The data show that when a bed of $0.53 \text{ }\mu\text{m}$ particle size is used, no significant oxidation is detected. When the particle size is increased to $8 \text{ }\mu\text{m}$ or larger, the initial stage oxidation rates with or without the preform exhibit minor differences only. As discussed in section 4.1, the weight gain rate in the initial stage corresponds to the rate of reaction

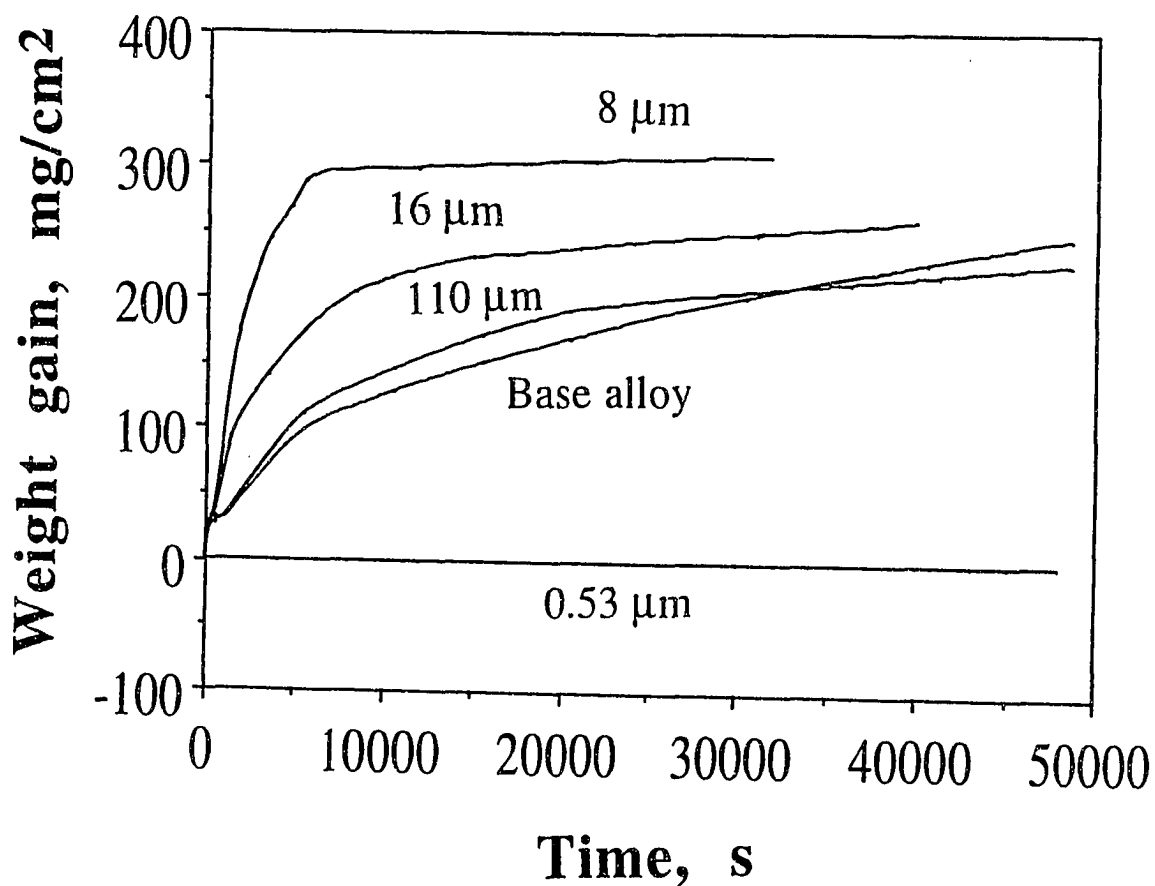


Fig. 4.23 Weight gain per unit area vs time for directed oxidation of Al-Mg alloy at 1450 K into Al₂O₃ preforms of different particle sizes. The weight gain per unit area vs time plot for the base alloy is also shown. The oxygen pressure, total pressure and the total gas flow rate were maintained constant at 85092 Pa, 93303 Pa and 8333 mm³/s STP, respectively.

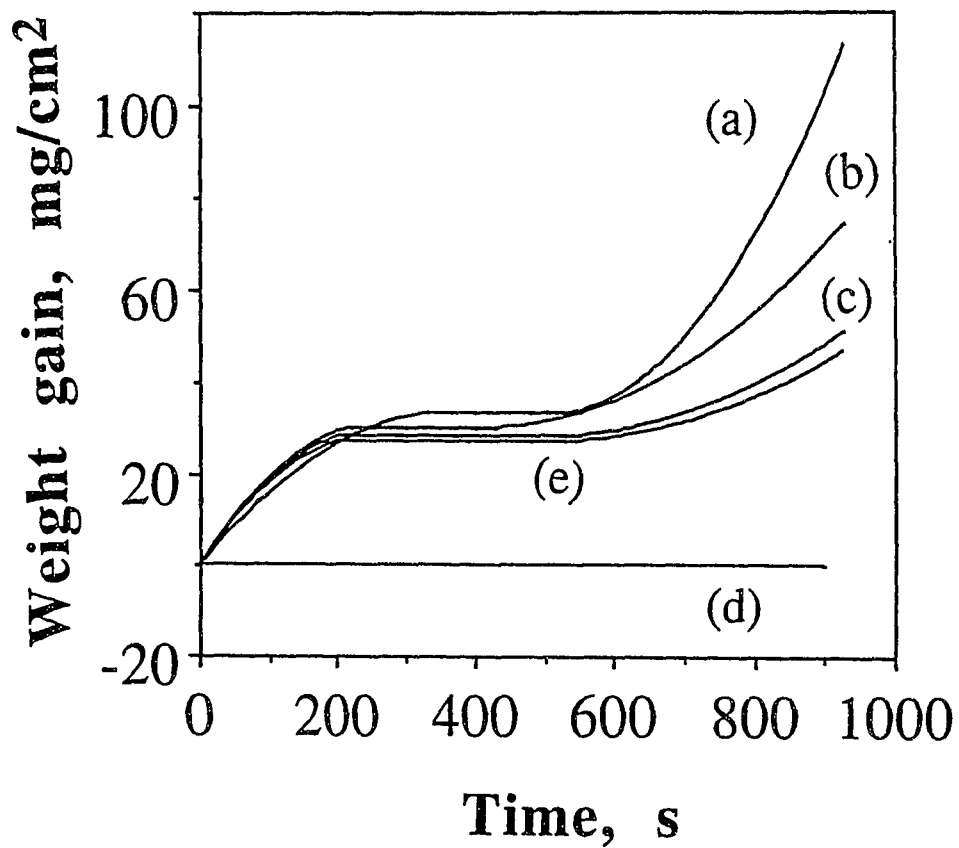


Fig. 4.24 Weight gain per unit area vs time in the initial stage of directed oxidation of Al-Mg alloy at 1450 K into Al_2O_3 preforms of different particle sizes: (a) 8 μm , (b) 16 μm , (c) 110 μm , and (d) 0.53 μm . The weight gain per unit area vs time plot in the initial stage for the base alloy (e) is also shown. Data correspond to the initial stage in Fig. 4.23.

enhanced vaporization of Mg. The rate of reaction enhanced vaporization is, in turn, proportional to the diffusivity of Mg vapor (Equation 4.2). As the alumina particle size in the preform decreases, the pore size would also correspondingly decrease (Table 3.4). The increase in the total number of particles per unit volume could cause an increase in pore tortuosity (τ). The diffusivity of Mg vapor through the porous preform (D_{eff}) would be given by the expression [52]:

$$D_{\text{eff}} = D \frac{\varepsilon}{\tau} \quad (4.31)$$

where D is the diffusivity of Mg vapor in free space, ε is the volume fraction of pores in the preform. According to equation (4.31), an increase in pore tortuosity for the 0.53 μm preform would significantly reduce the diffusivity of Mg vapor and, correspondingly, the rate of Mg vaporization. This would reduce the weight gain in the initial stage (amount of MgO formed).

Formation of a continuous MgO layer is essential for bulk formation of Al_2O_3 to take place. The inability to form a continuous MgO layer at the top surface would prevent continuous formation of Al_2O_3 in the growth stage for the 0.53 μm preform which is consistent with the absence of weight gain with increasing oxidation times (Fig. 4.21). This observation is in agreement with that reported by Sindel et al. [53] and Upadhyaya et al. [54]. These investigators [53-54] observed that composite formation did not occur satisfactorily for infiltration into Al_2O_3 preforms of particle size less than 2 μm .

4.5.2 Growth Stage

The weight gain rate in the growth stage for directed oxidation of Al-5056 alloy into alumina preforms of various particle sizes, can be estimated from the slopes of the weight gain vs time curves in Fig. 4.24. It is observed that the weight gain rate continuously decreases with time. For parabolic kinetics, the weight gain per unit area, w_t , would depend on oxidation time, t , as:

$$(w_t)^2 = ct \quad (4.32)$$

where c is the rate constant. The value of c indicates the rate controlling mechanism. It follows from equation (4.32) that the rate constant (c) can be obtained from the slope of a plot of $(w_t)^2$ versus t as shown in Fig. 4.25. It is observed that the curves for directed oxidation into preforms have two rate constants. The rate constant in the initial period increases with decreasing particle size. In addition, the change in rate constant occurs at earlier times for infiltration into the finer preforms. Furthermore, no change in the rate constant, in the growth stage, occurs for the directed oxidation of the base alloy. The presence of pre-existing Al_2O_3 particles introduces two effects which could alter the growth kinetics of Al-Mg alloys: (a) It could provide sites for preferential nucleation of Al_2O_3 (b) It could limit liquid metal transport to the growth surface.

Weight gain for directed oxidation of the Al-Mg alloy into an alumina preform of 8 μm particle size, was also measured as a function of time at different oxygen pressures (Fig. 4.26). It is seen from figures 4.22 and 4.26 that the weight gain rate decreases with time and is independent of oxygen pressure. The growth kinetics of the Al- 5 wt% Mg alloy into alumina preforms are analyzed below.

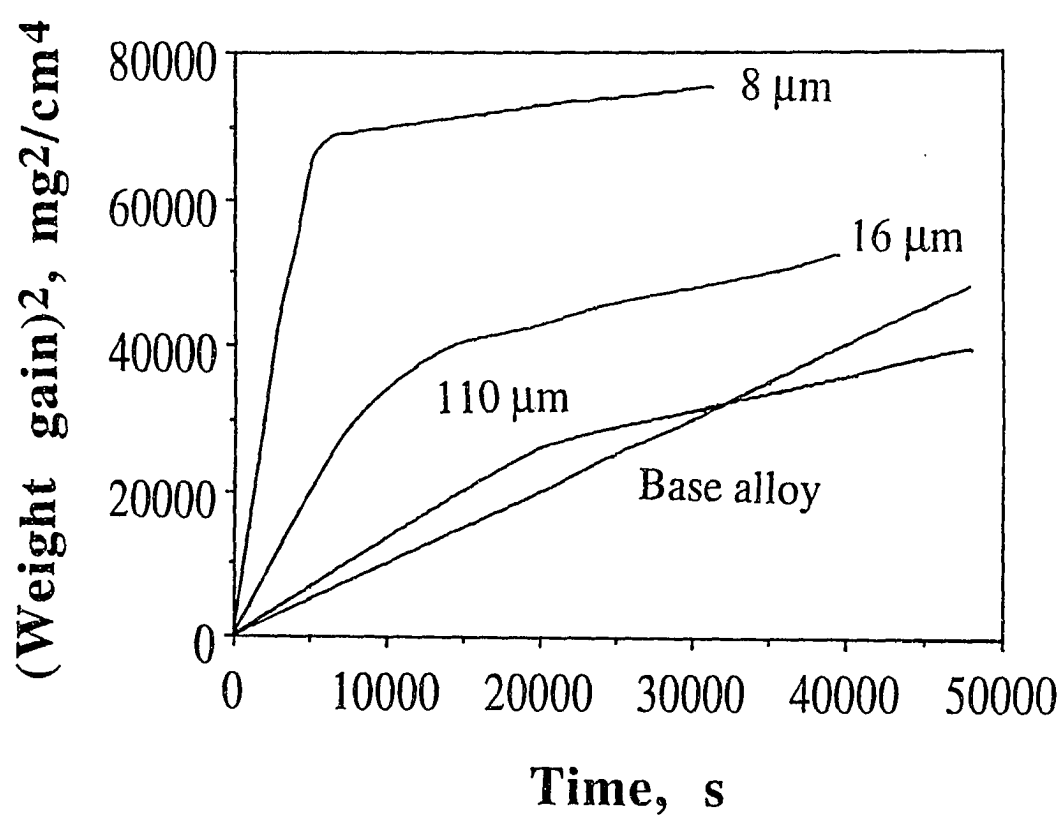


Fig. 4.25 Parabolic kinetics in the growth stage of directed oxidation of Al-Mg alloy at 1450 K into Al_2O_3 preforms of different particle sizes. Data correspond to the growth stage in Fig. 4.22.

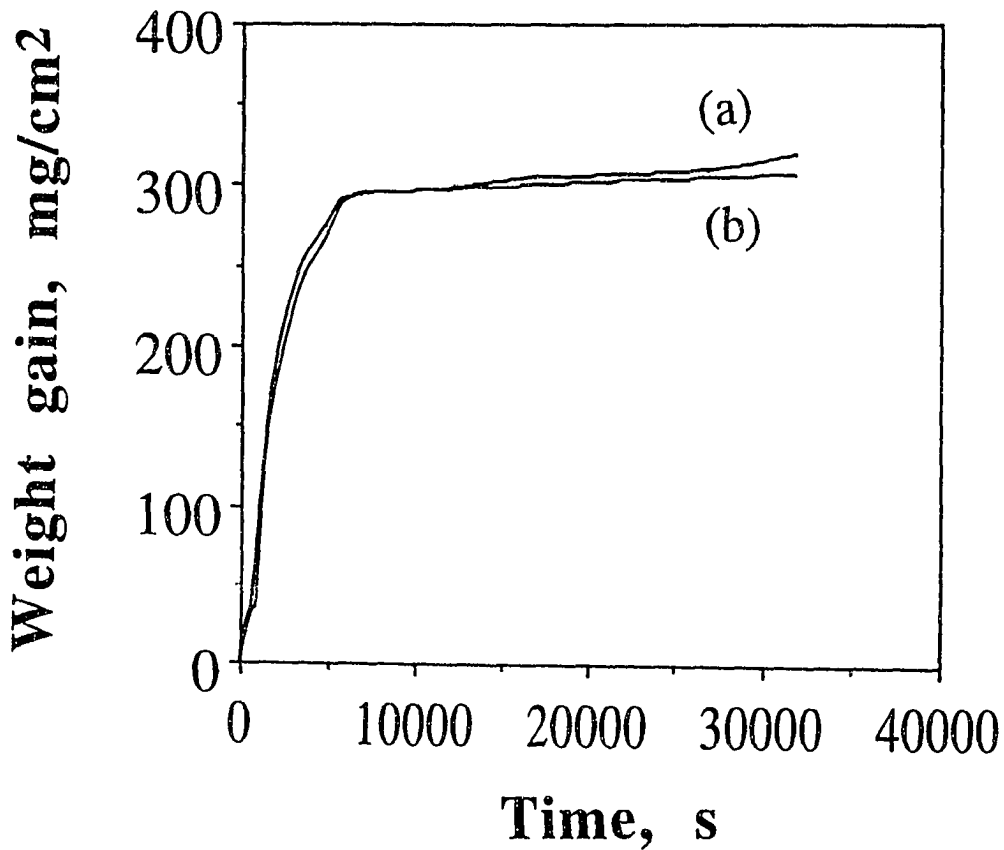


Fig. 4.26 Weight gain per unit area vs time for directed oxidation of Al-Mg alloy at 1450 K into Al₂O₃ preform of 8 μm particle size at different oxygen pressures: (a) 21273 Pa, and (b) 85092 Pa. The total pressure and the total gas flow rate were maintained constant at 93303 Pa and 8333 mm³/s STP, respectively.

4.5.2.1 Oxygen Transport

In the initial portion of the growth stage, the mechanism of oxidation into alumina preforms would correspond to the mechanism of oxidation of the base alloy. From section 4.2, it is observed that the growth kinetics of Al-Mg alloys is controlled by oxygen transport through the near-surface alloy layer. This is consistent with a situation where the weight gain rate decreases with time and is independent of oxygen pressure. From equation (4.17), the weight gain rate per unit area (J) for oxygen transport controlled oxidation rate in free space is given by the expression:

$$J = \frac{W}{A} = \frac{16D_o(X_o^I - X_o^{II})}{LV_m} \quad (4.33)$$

where W denotes the weight gain rate, A denotes the area, D_o is the diffusion coefficient of oxygen in molten aluminum, X_o^I is the mole fraction of dissolved oxygen in the alloy film at the MgO/alloy film interface, X_o^{II} is the mole fraction of dissolved oxygen in the alloy film at the Al₂O₃/alloy film interface, L is the thickness of the alloy film, and V_m is the molar volume of the alloy.

For directed oxidation of Al-Mg alloy alone, A denotes the cross-sectional area of the melt and is equal to 1.54 cm². In the case of oxidation into a Al₂O₃ preform, A corresponds to the void space between the alumina particles (A_{void}) and is estimated to be 0.693 cm² (in the absence of wetting). Wetting between the Al-melt and the Al₂O₃ particles would increase the cross-sectional area from A_{void} to A_w by an amount proportional to the surface area per unit volume of the particle ($3/R$ for spherical particles). A_w would then be given by the expression:

$$A_w = k \times \frac{3}{R} \quad (4.34)$$

where k is a measure of the volume associated with the oxidation interface, and R denotes the Al_2O_3 particle size. The rate of oxygen transport across the alloy layer, for directed oxidation into an alumina preform can then be estimated from Equation (4.33) as:

$$J_{\text{pre}} = \frac{W_{\text{pre}}}{A_w} = \frac{16D_o(X_o^I - X_o^{II})}{LV_m} \quad (4.35)$$

where J_{pre} denotes the weight gain rate per unit area for infiltration into an Al_2O_3 preform and W_{pre} denotes the corresponding weight gain rate. Equation (4.35) can be re-written as:

$$\frac{W_{\text{pre}}}{A_{\text{void}}} = \frac{A_w}{A_{\text{void}}} \times \frac{16D_o(X_o^I - X_o^{II})}{LV_m} \quad (4.36)$$

The maximum value of $W_{\text{pre}}/A_{\text{void}}$ can be determined, for each particle size, from the initial slope of each curve in Fig. 4.23 in the growth stage and are given in Table 4.6. Values for D_o , X_o^I , X_o^{II} , L , and V_m are given in Table 4.7. Using these values in equation (4.36), A_w and k can be estimated for various particle sizes and are shown in Table 4.8. In the initial period of the growth stage, A_w increases with decreasing particle size as can be observed from Table 4.8. This indicates that wetting of the Al_2O_3 particles by the Al melt (or secondary nucleation of Al_2O_3 on the existing Al_2O_3 particles) occurs in the initial portion of the growth stage. However, wetting alone cannot extend the oxidation front unless the melt is accompanied by the surface MgO and the underlying Al_2O_3 product. It is also seen from Table 4.8 that k decreases with

Table 4.6 Maximum weight gain rate as a function of Al₂O₃ particle size, for infiltration of Al-Mg alloy into Al₂O₃ preforms at 1450 K.

Al ₂ O ₃ particle size, μm	Maximum weight gain rate, $\text{mg}/\text{cm}^2\text{sec}$
8	0.0872
16	0.06
110	0.0192
Base alloy	0.016

Table 4.7 Data used in the calculation of oxygen transport through the near surface alloy layer.

Property	Symbol	Value	Reference
Diffusivity of oxygen in molten aluminum*, m ² /sec	D_o	1.3×10^{-8}	[11]
Thickness of alloy layer, m	L	4.7×10^{-6}	[7]
Oxygen concentration in the alloy film at the MgO/film interface**, mole fraction	X_o^I	4.4×10^{-5}	[3,4,17]
Oxygen concentration in the alloy film at the Al ₂ O ₃ /film interface**, mole fraction	X_o^{II}	2.0×10^{-6}	[3,4,17]

* Tracer diffusivity of oxygen in molten aluminum is approximated by the diffusivity of aluminum in molten aluminum at 1450 K.

** Oxygen concentrations calculated at 1450 K for a Mg concentration of 0.22 mol % in the alloy film.

Table 4.8 A_w as a function of Al_2O_3 particle size, for infiltration of Al-Mg alloy into Al_2O_3 preforms at 1450 K.

Al_2O_3 particle size, μm	A_w, cm^2	$k \times 10^4, cm^3$
8	3.8	10.1
16	2.6	13.9
110	0.8	30.5

decreasing particle size. This indicates that the volume associated with the extended interface decreases with particle size. Since pore size decreases with decreasing particle size, the interparticle spaces can be filled in a shorter time by the composite growing from the particle surfaces, and hence k would decrease with decreasing particle size. This decrease in k with decreasing particle size partially counteracts the increase in surface area per unit volume. Hence, though the weight gain rate (Table 4.6) increases with decreasing particle size, it does not scale to the surface area per unit volume of the particle.

The case for secondary nucleation and growth from the Al_2O_3 particles is further supported by observations of the grain structure in the final composite. It is well established that oxidation in the absence of a preform leads to columnar grains tens of micrometers across, growing with the same crystallographic orientation over hundreds of micrometers [7,21]. In contrast, the Al_2O_3 composite grown into an Al_2O_3 preform exhibits the same orientation over smaller regions ($\sim 10\text{-}50\ \mu\text{m}$) [55]. In addition, the grain sizes of the alumina and the metal are refined [55]. Furthermore, one third to one half of the surfaces of each Al_2O_3 particle is directly bonded to the matrix Al_2O_3 [55]. These observations strongly support the role of Al_2O_3 particles in the preform in increasing the weight gain rate by aiding secondary nucleation of Al_2O_3 .

4.5.2.2 Liquid Metal Transport

It is observed from Fig. 4.25 that, for oxidation into alumina preforms, there is a change of rate constant with increasing oxidation time. In addition, this change of rate constant occurs earlier as the Al_2O_3 particle size decreases. However, no change of rate constant occurs for the directed oxidation of the base alloy (Fig. 4.25). This change of

rate constant indicates that oxygen transport is no longer the rate controlling mechanism for oxidation into preforms. As oxidation proceeds into the preform, the oxidation front becomes more extended and convoluted (Fig. 4.27). This, in turn, would slow down the rate of liquid metal transport to the oxidation front. If rate of liquid metal transport decreased sufficiently, it would become the rate controlling mechanism and would correspond to the experimentally measured weight gain rate.

Weight gain rates for the various particle sizes, were measured at a time of 30,000s (slope change has occurred) and are given in Table 4.9. From equation (11) in Appendix D, the rate of liquid metal transport (J) is given by the expression:

$$J \propto \left[\frac{r}{t} \right]^{\frac{1}{2}} \propto \left[\frac{R}{t} \right]^{\frac{1}{2}} \quad (4.37)$$

where r denotes the pore radius and t denotes the time of oxidation. It is seen from equation (4.37) that the rate of liquid metal transport is proportional to the square root of the particle size. It is seen from Table 4.9 that though the weight gain rate slightly increases with particle size, the increase is not proportional to the square root of the particle size. This indicates that at longer oxidation times, liquid metal transport is not the only rate controlling factor. It is seen from Table 4.6 that the rate of oxygen transport increases with decreasing particle size. A mixed control mechanism involving oxygen transport in the metal layer and liquid metal transport through the composite would explain the particle size dependence of the weight gain rate at extended oxidation times. It needs to be noted, however, that the weight gain rates in the second period of the growth stage are small. Therefore, the change in the mechanism cannot be defined conclusively.

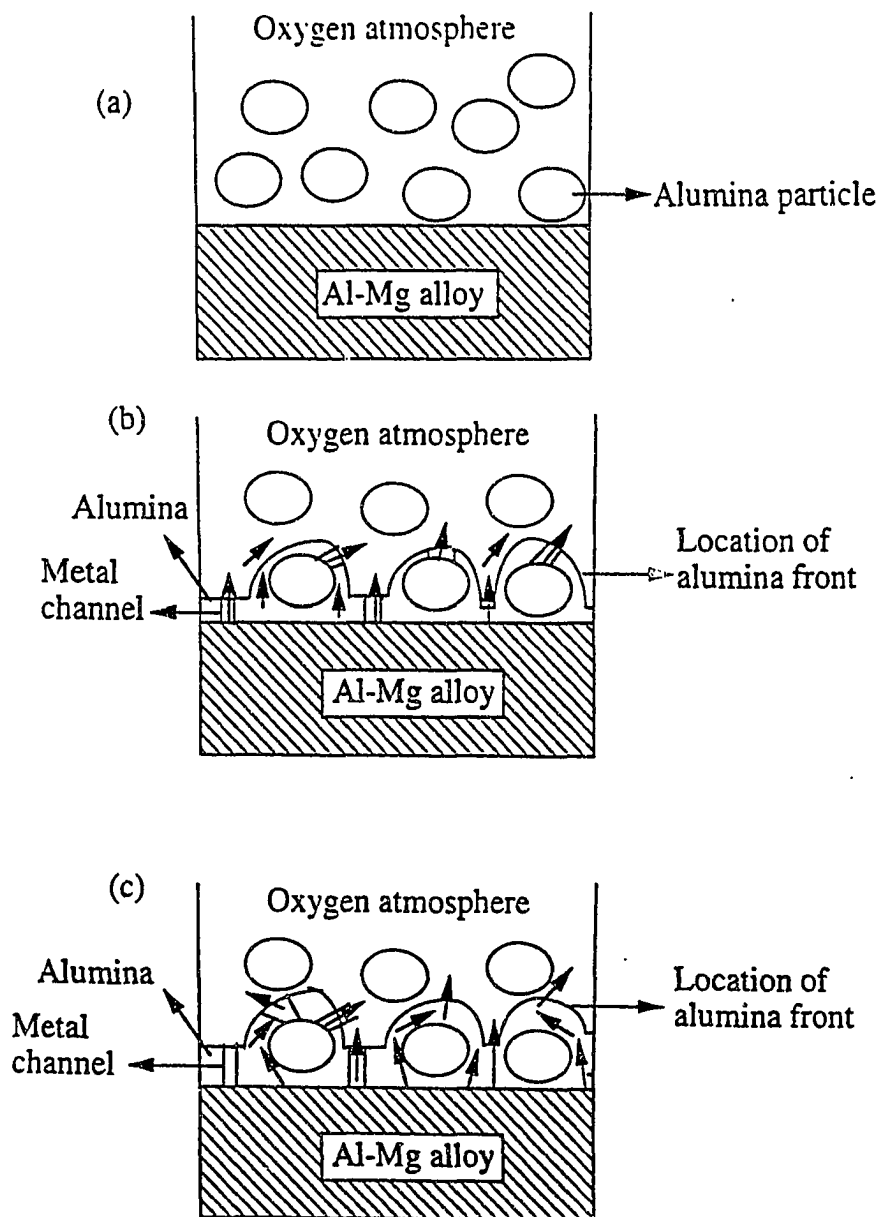


Fig. 4.27 Schematic diagram showing the movement of the oxidation front from (a) to (c), as directed oxidation of Al-Mg alloy proceeds through an Al_2O_3 preform.

Table 4.9 Weight gain rate as a function of Al₂O₃ particle size, at 30000 s, for infiltration of Al-Mg alloy into Al₂O₃ preforms at 1450 K.

Al ₂ O ₃ particle size (R), μm	R ^{1/2} , (μm) ^{1/2}	Weight gain rate, mg/cm ² sec
8	2.83	0.0015
16	4	0.0018
110	10.5	0.0019

Thus, the presence of an Al_2O_3 preform produces two effects on the rate of directed oxidation of Al-Mg alloys. Initially, the mechanism of oxidation of Al-Mg alloy into the alumina preforms is similar to the mechanism of the oxidation of the Al-Mg alloy into free space. The weight gain rate is controlled by oxygen transport through the surface alloy layer and increases with increasing secondary nucleation of Al_2O_3 on the Al_2O_3 particles. In this regime, the weight gain rate decreases with increasing Al_2O_3 particle size. With increasing oxidation time, liquid metal transport to the oxidation front slows down. The weight gain rate data in this regime seem to be consistent with mixed transport control involving oxygen transport in the metal layer and liquid metal transport through the composite.

4.6 References

1. H. Venugopalan, K. Tankala and T. DebRoy, "Probing the Initial Stage of Synthesis of $\text{Al}_2\text{O}_3/\text{Al}$ Composites by Directed Oxidation of Al-Mg Alloys," accepted for publication in *Metallurgical and Materials Transactions*.
2. K. C. Vlach, O. Salas, H. Ni, V. Jayaram, C. G. Levi and R. Mehrabian, "A Thermogravimetric Study of the Oxidative Growth of $\text{Al}_2\text{O}_3/\text{Al}$ Composites," *J. Mater. Res.*, **6** [9] 1982-95 (1991).
3. B. L. Tiwari, "Thermodynamic Properties of Liquid Al-Mg Alloys Measured by the Emf Method", *Metallurgical Transactions A* **18A**,1645-1651 (1987).
4. M. W. Chase, Jr., C. A. Davies, J. R. Bowary, Jr., D. J. Fromp, R. A. McDonald and A. N. Syverud, *JANAF Thermochemical Tables*, 3rd ed., American Chemical Society, Washington, DC, 1986.
5. H. Venugopalan, K. Tankala and T. DebRoy, "Kinetics of Oxidation of Al-Mg Alloys in the Initial and Final Stages of Synthesis of $\text{Al}_2\text{O}_3/\text{Al}$ Composites," submitted for publication.
6. S. Antolin, A. S. Nagelberg and D. K. Creber, "Formation of $\text{Al}_2\text{O}_3/\text{Metal}$ Composites by the Directed Oxidation of Molten Aluminum-Magnesium-Silicon Alloys: Part I, Microstructural Development," *J. Am. Ceram. Soc.*, **75** [2] 447-54 (1992).
7. O. Salas, H. Ni, V. Jayaram, K. C. Vlach, C. G. Levi and R. Mehrabian, "Nucleation and Growth of $\text{Al}_2\text{O}_3/\text{Metal}$ Composites by Oxidation of Aluminum Alloys," *J. Mater. Res.*, **6** [9] 1964-81 (1991).
8. A. S. Nagelberg, S. Antolin and A. W. Urquhart, "Formation of $\text{Al}_2\text{O}_3/\text{Metal}$ Composites by the Directed Oxidation of Molten Aluminum-Magnesium-Silicon Alloys: Part II, Growth Kinetics," *J. Am. Ceram. Soc.*, **75** [2] 455-462 (1992).
9. H. Venugopalan, K. Tankala and T. DebRoy, "Electrical Conductivity of Alumina/Aluminum Composites Synthesized by Directed Metal Oxidation," *J. Am. Ceram. Soc.*, **77** [11] 3045-47 (1994).
10. E. A. Brandes and G. B. Brook (Eds.), *General Physical Properties: Smithells Metals Reference Handbook*, 7th ed; p. 14-10, Butterworth Heinemann, London, UK, 1992.

11. F. S. Levin, "Polytherms of the Viscosity and Self-Diffusion of Molten Aluminum," *Izv. Akad. Nauk SSSR, Met.*, **5**, 72-78, Sept.-Oct. (1971).
12. O. Kubaschewski, C. B. Alcock and P. J. Spencer, *Materials Thermochemistry*, Pergamon Press, 1993.
13. P. Xiao and B. Derby, "Alumina/Aluminum Composites Formed by the Directed Oxidation of Aluminum Using Magnesia as a Surface Dopant," *J. Am. Ceram. Soc.*, **77** [7] 1761-70 (1994).
14. M. Sindel, N. A. Travitsky and N. Claussen, "Influence of Magnesium-Aluminum Spinel on the Directed Oxidation of Molten Aluminum Alloys," *J. Am. Ceram. Soc.*, **73** [9], 2615-18 (1990).
15. K. Ando and M. Momoda, "Solubility of MgO in Single Crystal Al_2O_3 ," *J. Ceram. Soc. Jpn, Int. Ed.*, **95**, 343-47 (1987).
16. O. Salas, V. Jayaram, K. C. Vlach, C. G. Levi and R. Mehrabian, "Banded Microstructures in $\text{Al}_2\text{O}_3/\text{Al}$ Composites Produced by Oxidation of Molten Al-Mg Alloys," in *Processing and Fabrication of Advanced Materials for High Temperature Applications*, V. A. Ravi and T. S. Srivatsan (Eds.), TMS, 1992.
17. S. Otsuka and Z. Kozuka, "Thermodynamic Study of Oxygen in Liquid Elements of Group Ib to VIb," *Trans. J. Inst. of Met.*, **22** [8], 558-566 (1981).
18. A. S. Nagelberg, A. S. Fareed and D. J. Landini, "Production of Ceramic Matrix Composites for Elevated Temperature Applications Using the DIMOX™ Directed Metal Oxidation Process," *Processing and Fabrication of Advanced Materials*, The Minerals, Metals and Materials Society, 1992, pp 127-142.
19. H. Venugopalan and T. DebRoy, "Growth Stage Kinetics in the Synthesis of $\text{Al}_2\text{O}_3/\text{Al}$ Composites by Directed Oxidation of Al-Mg and Al-Mg-Si Alloys," submitted for publication.
20. A. A. Nayeb-Hashemi and J. B. Clark, "The Magnesium-Silicon System," *Bull. Alloy. Phase. Diag.*, **5**, [6] 584-92 (1984).
21. E. Breval, M. K. Aghajanian and S. J. Luszcz, "Microstructure and Composition of Alumina/Aluminum Composites Made by Directed Oxidation of Aluminum," *J. Am. Ceram. Soc.*, **73** [9] 2610-2614 (1990).

22. R. E. Meredith and C. W. Tobias, *Adv. Electrochem. Electrochemical Engng.*, **2**, p. 15, Interscience, New York, 1962.
23. L. K. H. Von Beek, *Prog. Dielect.*, **7**, p. 69, Heywood, London, 1965.
24. A. R. Ubbelohde, *The Molten State of Matter*, p. 239, Wiley, New York, 1978.
25. W. D. Kingery, H. K. Bowen and D. R Uhlmann, *Introduction to Ceramics*, 2nd ed; p. 593, Wiley, New York, 1976.
26. A. J. Moulson and P. Popper, "Problems Associated with the Measurement of Volume Resistivity of Insulating Ceramics at High Temperatures," *Proc. Brit. Ceram. Soc.*, **10**, 41-50 (1968).
27. P. Kofstad, *Nonstoichiometry, Diffusion and Electrical Conductivity in Binary Metal Oxides*, p. 87, Wiley-Interscience, New York, 1972.
28. J. Yee and F. A. Kroger, "Measurements of Electromotive Force in Al_2O_3 - Pitfalls and Results," *J. Am. Ceram. Soc.*, **56** [4] 189-191 (1973).
29. F. A. Kroger, "Experimental and Calculated Values of Defect Parameters and the Defect Structure of α - Al_2O_3 "; pp 100-118 in *Structure and Properties of MgO and Al_2O_3 Ceramics*. American Ceramic Society, Columbus, OH, 1984.
30. B. V. Dutt and F. A. Kroger, "High-Temperature Defect Structure of Iron-Doped α - Al_2O_3 ," *J. Am Ceram. Soc.*, **58** [11-12] 474-476 (1975).
31. M. M. El-Aiat, L. D. Hou, S. K. Tikku, H. A. Wang and F. A. Kroger, "High-Temperature Conductivity and Creep of Polycrystalline Al_2O_3 Doped with Fe and/or Ti," *J. Am. Ceram. Soc.*, **64** [3] 174-182 (1981).
32. G. W. Hollenberg and R. S. Gordon, "Effect of Oxygen Partial Pressure on the Creep of Polycrystalline Al_2O_3 Doped with Cr. Fe and Ti," *J. Am. Ceram. Soc.*, **56** [3] 140-147 (1973).
33. R. T. Cox, "Chemical Reactions and Mass Transport Processes in Donor and Acceptor Doped Al_2O_3 Crystals," *J. Phys. (Paris). Colloq.*, **34** [9] 333-335 (1973).

34. B. J. Pletka, T. E. Mitchell, and A. H. Heuer, "Dislocation Sub-Structures in Doped Sapphire (α - Al_2O_3) Deformed by Basic Slip," *Acta Metall*, **30** [1] 147-156 (1982).
35. W. Raja Rao and I. B. Cutler, "Effect of Iron Oxide on the Sintering Kinetics of Al_2O_3 ," *J. Am. Ceram. Soc.*, **56** [11] 588-593 (1973).
36. S. K. Mohapatra, S. K. Tiku and F. A. Kroger, "Defect Structure of Unintentionally Doped α - Al_2O_3 Crystals," *J. Am. Ceram. Soc.*, **62** [1-2] 50-57 (1979).
37. K. Kitzawa and R. L. Coble, "Electrical Conduction in Single - Crystal and Polycrystalline Al_2O_3 at High Temperatures," *J. Am. Ceram. Soc.*, **57** [6] 245-250 (1974).
38. H. Venugopalan and T. DebRoy, "Metal Distribution in Alumina/Aluminum Composites by Directed Metal Oxidation," submitted for publication.
39. M. K. Aghajanian, N. H. Macmillan, C. R. Kennedy, S. J. Luszcz and R. Roy, "Properties and Microstructure of Lanxide® Al_2O_3 -Al Ceramic Composite Materials," *J. Mat. Sci.*, **24** 658-670 (1989).
40. E. Manor, H. Ni, C. G. Levi and R. Mehrabian, "Microstructure Evolution of SiC/ Al_2O_3 /Al-Alloy Composites Produced by Melt Oxidation," *J. Am. Ceram. Soc.*, **76** [7] 1777-87 (1993).
41. G. A. Chadwick and D. A. Smith, *Grain Boundary Structure and Properties*, Academic Press, London, 1976.
42. W. Bollmann, *Crystal Defects and Crystalline Interfaces*, Springer, Berlin, 1970.
43. M. S. Newkirk, A. W. Urquhart, H.R. Zwicker and E. Breval, "Formation of Lanxide™ Ceramic Composite Materials," *J. Mater. Res.*, 1 81-89 (1986).
44. V. Laurent, D. Chatain, C. Chatillon and N. Eustathopoulos, "Wettability of Monocrystalline Alumina by Aluminum Between Its Melting Point and 1273 K," *Acta Metall.*, **36** [7] 1797-1803 (1988).
45. L. D. Lucas, *Techniques de l'Ingenieur*, M67 Paris (1984).

46. H. Grimmer, R. Bonnet, S. Lartigue and L. Priester, "Theoretical and Experimental Description of Grain Boundaries in Rhombohedral α -Alumina," *Philos. Mag.*, **A61**, 493-509 (1990).
47. T. Hoche, P. R. Kenway, H. J. Kleebe, M. Ruhle and P. A. Morris, "High-Resolution Transmission Electron Microscopy Studies of a Near $\Sigma 11$ Grain Boundary in α -Alumina," *J. Am. Ceram. Soc.*, **77** [2] 339-48 (1994).
48. D. R. Clarke and G. Thomas, "Grain Boundary Phases in a Hot-pressed MgO Fluxed Silicon Nitride," *J. Am. Ceram. Soc.*, **60** [11-12] 491-95 (1977).
49. W. P. Minnear, "Interfacial Energies in the Si/SiC system and the Si+C Reaction," *J. Am. Ceram. Soc.*, **65**, C-10 (1982).
50. N. M. Parikh and M. Humenik, "Cermets: II, Wettability and Microstructure Studies in Liquid-Phase Sintering," *J. Am. Ceram. Soc.*, **40** [9] 315-320 (1957).
51. G. T. Nolan and P. E. Kavanagh, "Computer Simulation of Random Packing of Hard Spheres," *Powder Technology*, **72** 149-155 (1992).
52. J. Szekely, J. W. Evans and H. Y. Sohn, *Gas-Solid Reactions*, Academic Press, New York, NY, 1976.
53. M. Sindel and N. Claussen, *Emerging Materials by Advanced Processing*, W. A. Kaysser and J. Weber (eds.), KFA, Julich, 1989.
54. D. D. Upadhyaya, R. Bhat, S. Ramanathan and S. K. Roy, "Effect of Filler Phase Porosity on Directed Oxidation of Al Alloy," *Journal of Alloys and Compounds*, **205** 275-79 (1994).
55. E. Breval and A. S. Nagelberg, "Microstructure of an Al_2O_3 /Metal Composite Containing an Filler Material," *Mat. Res. Soc. Symp. Proc.*, **132** 93-98 (1989).

CHAPTER 5

SUMMARY AND CONCLUSIONS

The initial stage of directed oxidation of Al-Mg alloys has been investigated both experimentally and theoretically. The weight gain with time during the initial stage was measured for different oxygen pressures. The oxygen pressures were established using inert gas-oxygen mixtures. The effect of diffusivity of oxygen and magnesium on the weight gain rate was examined by varying the external pressure and the nature of the inert gas while maintaining the oxygen pressure constant. In the initial stage, MgO forms by vapor phase oxidation of Mg(g) and falls back on the crucible. A mathematical model was developed for the vaporization of Mg from the Al-Mg alloy in a reactive oxygen-inert gas atmosphere. The model calculates the velocity, temperature and concentration profiles in the reactor through numerical solutions of the equations of conservation of momentum, enthalpy and concentrations of Mg(g) and O₂. The magnesium vaporization rate and the corresponding oxygen weight gain rate are calculated from the concentration profiles as a function of time. The predictions of the model are compared with experimental data to seek an improved understanding of the initial stage of composite growth.

The predicted variation of the weight gain with time in the initial stage of oxidation agreed well with the experimental data. It is seen that at low oxygen pressures comparable to the equilibrium vapor pressure over the Al-Mg alloy, the weight gain rate in the initial stage decreases with time, while the weight gain rate is independent of time at high oxygen pressures. The weight gain in the initial stage also increases with increase in oxygen pressure and oxygen diffusivity. These results confirm the reaction enhanced, gaseous diffusion limited, vaporization of Mg in the initial stage of oxidation of Al-Mg alloys. The thickness of the magnesium boundary layer decreases continuously with time as the alloy

composition changes owing to magnesium vaporization. It is shown that the end of the initial stage corresponds to the time when the oxygen front essentially collapses on to the alloy surface.

The oxidation rates in the growth stage of directed oxidation of Al-Mg and Al-Mg-Si alloys have been investigated. The weight gain rate in the growth stage of Al-Mg alloys decreased with time and was independent of oxygen pressure. The activation energy for the growth process was found to be 361 kJ/mole. The oxygen pressure, time and temperature dependencies of the growth rate of Al-Mg alloys are consistent with the characteristics of an oxidation reaction controlled by oxygen transport through the near surface alloy layer.

The weight gain rate in the growth stage of Al-Mg-Si alloys was independent of time and proportional to $P_{O_2}^{\frac{1}{4}}$. Analysis of the influence of silicon on the various steps in the growth stage indicates that silicon additions increase the rate of oxygen transport through the alloy layer and decrease the rate of electronic transport through the MgO layer. As a result, electronic transport through the outer MgO layer controls the growth stage mechanism in the directed oxidation of Al-Mg-Si alloys which is consistent with the experimental results. Thus, silicon additions to Al-Mg alloys alter the oxidation mechanism from oxygen transport through the near surface alloy layer to electronic transport through the MgO layer.

Electrical conductivities of Al₂O₃/Al composite and Al₂O₃-MgO pellets were used to understand the distribution of aluminum metal in the Al₂O₃/Al composite and the activation energy for the migration of the dominant charge carrier in the alumina matrix. The conductivity of Al₂O₃/Al composite was found to be six to seven orders of magnitude higher than that of sintered Al₂O₃-4% MgO. A small fraction of the aluminum channels

extend over the entire thickness of the composite. Activation energy of migration of the dominant charge carrier in the sintered Al_2O_3 -4% MgO was found to be 1.36 eV.

The electrical conductivity of the $\text{Al}_2\text{O}_3/\text{Al}$ composite and the amount of metal in the composite were studied as a function of the growth temperature to understand the temperature dependence of metal distribution in the composite. The results indicate that both the quantity and interconnection of the Al phase in the $\text{Al}_2\text{O}_3/\text{Al}$ composite decrease with increasing growth temperature. The observed changes in microstructure with temperature can be explained if γ_{SS} decreases faster relative to $2 \gamma_{\text{SL}}$, for a number of grain boundaries in Al_2O_3 , as the growth temperature increases.

The kinetics of growth of Al-Mg alloys into Al_2O_3 preforms has been investigated as a function of oxygen pressure, and preform particle size. The weight gain rate decreased with time and was independent of oxygen pressure. The presence of an Al_2O_3 preform produces two effects on the rate of directed oxidation of Al-Mg alloys. Initially, the mechanism of oxidation of Al-Mg alloy into the alumina preforms was similar to the mechanism of the oxidation of the Al-Mg alloy into free space. The weight gain rate was controlled by oxygen transport through the surface alloy layer and increased with increasing secondary nucleation of Al_2O_3 on the Al_2O_3 particles. In this regime, the weight gain rate decreased with increasing Al_2O_3 particle size. With increasing oxidation time, liquid metal transport to the oxidation front slows down rapidly. The weight gain rate data in this regime seem to be consistent with mixed control mechanism involving liquid metal transport through the composite and oxygen transport across the alloy layer.

APPENDIX A

CALCULATION OF BINARY DIFFUSION COEFFICIENT

The binary diffusion coefficient, D_{12} , which depends on temperature, pressure, molecular weights of the species and the intermolecular forces is given by the following expression [1]:

$$D_{12} = 0.002628 \frac{\sqrt{T^3(M_1 + M_2)/2M_1M_2}}{p\sigma_{12}^2\Omega_{12}^{(1,1)}(T_{12}^*)} \quad (\text{A1})$$

where,

D_{12} is the diffusion coefficient in cm^2/sec ,

p is the pressure in atmospheres,

T is the temperature in K,

$$T_{12}^* = kT/\epsilon_{12},$$

M_1, M_2 are the molecular weights of species 1 and 2,

ϵ_{12} is the maximum energy of attraction between species 1 and 2,

$\Omega_{12}^{(1,2)}$ is the collision integral for the molecules of species 1 and 2.

References

1. J. O. Hirschfelder, C. F. Curtiss and R. B. Bird, *Molecular Theory of Gases and Liquids*, Wiley, New York, NY, 1954.

APPENDIX B

ADAPTATION ROUTINE FOR THE CALCULATION OF RATE OF MAGNESIUM VAPORIZATION FROM THE Al-Mg ALLOY IN THE TGA SET-UP DURING THE INITIAL STAGE

The following adaptation routine was used along with a generally available commercial program, MicroCompact version 1.1, Innovative Research, Inc., MN, for the solution of equations of conservation of momentum, energy and concentration of magnesium vapor and oxygen in the cylindrical thermogravimetric set-up. The solution to the conservation equations are subsequently used to determine the rate of magnesium vaporization from the surface of the Al-Mg alloy melt, as a function of time. Furthermore, the corresponding rate of oxygen uptake and weight gain in the initial stage of oxidation are calculated as a function of time. Figure B.1 shows a schematic of the computational domain.

subroutine adapt

c-----definitions of terms used in the program-----

```

c      ai:  $\text{amo}2/(2.0*\text{ammg})$ 
c      amal, amar, ammg, amo2: atomic weights of aluminum, argon, magnesium and
c      oxygen
c      amuref: viscosity of the gas mixture
c      avmol: average molecular weight of the gas mixture
c      cond: thermal conductivity of the gas mixture
c      cp: heat capacity of the gas mixture
c      delta: thickness of the Mg boundary layer
c      dgas: array for storing the density of the gas mixture
c      diff: diffusivity of the gas mixture
c      flor: gas flow rate
c      flowar: cross-sectional area of flow
c      fluxmol: Mg vaporization flux from the melt surface in moles/cm2 sec
c      fluxgm: Mg vaporization flux from the melt surface in grams/cm2 sec
c      gams: viscosity of the crucible walls
c      ni: number of grids in the x-direction
c      nj: number of grids in the y-direction

```

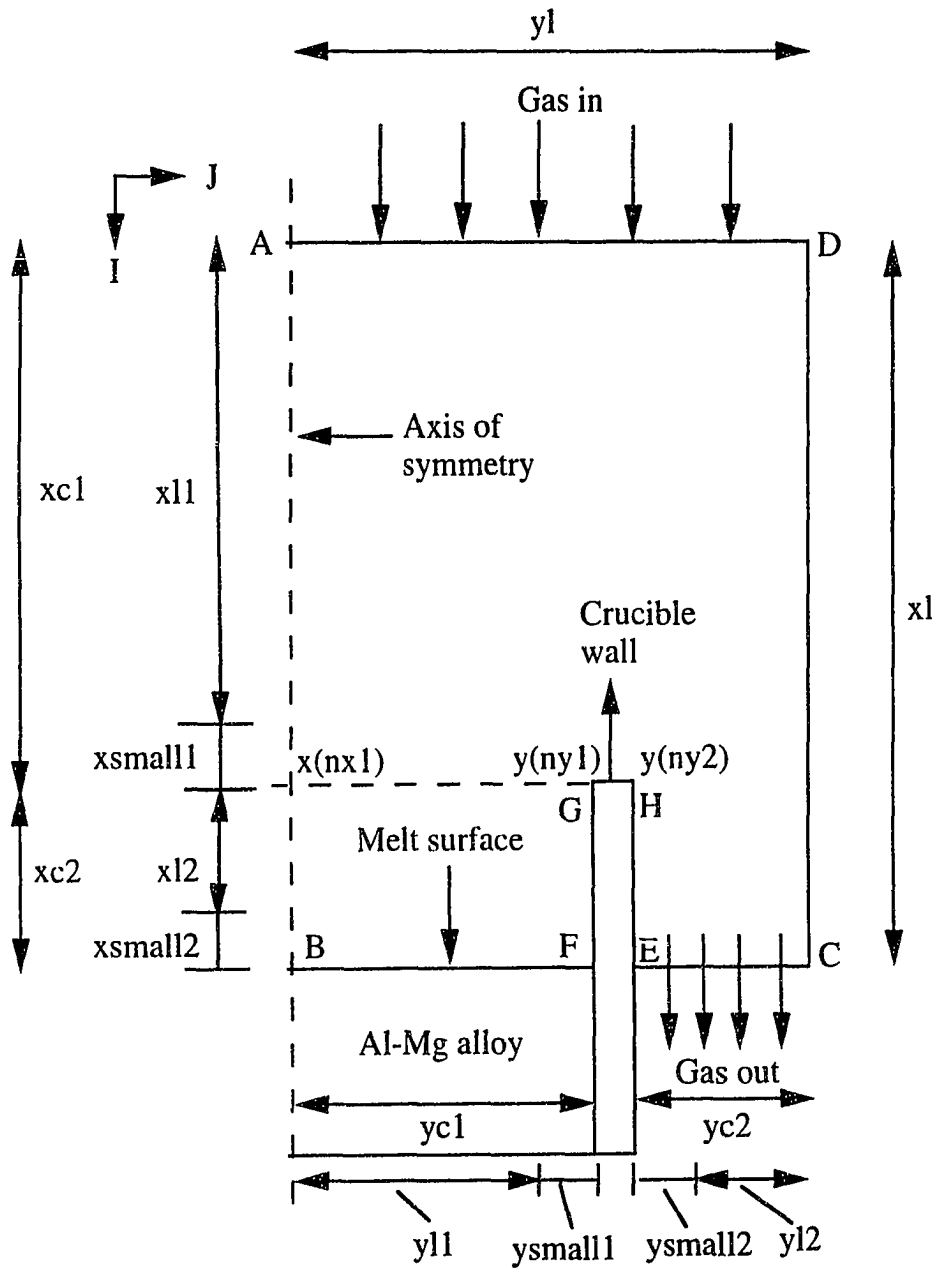


Fig. B.1 Schematic diagram of computational domain chosen for calculation of velocity, temperature and concentration fields.

```

c      pmg: equilibrium partial pressure of magnesium vapor at temperature, tsurf, in torr
c      pmgs: partial pressure of magnesium vapor in equilibrium with the alloy melt (torr)
c      press: total pressure in the reactor
c      t: array for storing temperatures in the gas phase
c      tinlet: inlet temperature of the gas mixture
c      texp: experimentally measured temperature in the equi-temperature zone
c      totcon: total number of moles of gas at the melt surface
c      tsurf: temperature of the melt surface
c      uav: average gas velocity at the inlet
c      wmg: array for storing the weight fraction of magnesium vapor in the gas phase
c      wngo2: array for storing wmg-wo2/ai
c      wtinst: weight of the Al-Mg alloy at any instant
c      wtloss: weight loss from the Al-Mg alloy due to Mg vaporization
c      wtgain: weight gained by the crucible due to MgO formation
c      wo2: array for storing the weight fraction of oxygen in the gas phase
c      wo2b: weight fraction of oxygen at the inlet
c      xc1: distance from inlet to equi temperature zone
c      xc2: length of the equi-temperature zone
c      xl: x-direction length of computational domain
c      yl: y-direction length of computational domain
c      xo2: mole fraction of oxygen in the gas phase
c      xo2b: mole fraction of oxygen at the inlet
c      xmqliq: mole fraction of magnesium in the alloy
c-----end of definition of terms

```

```

subroutine adapt

```

```

parameter(ni=40,nj=20,nfmax=8)

```

```

$include: '\ADPT.FOR'

```

```

dimension wmg(ni,nj),wo2(ni,nj),t(ni,nj)

```

```

dimension wngo2(ni,nj),dgas(ni,nj)

```

```

equivalence (f(1,1,5),t(1,1)),(f(1,1,6),wngo2(1,1)),

```

```

1(f(1,1,7),wmg(1,1)),(f(1,1,8),wo2(1,1))

```

```

c-----

```

```

entry grid

```

```

open(unit=7,file='printun')

```

```

header='Initial Oxidation'
c-----Geometric variables
  call inta6(l1,ni,m1,nj,mode,2,nx1,20,ny1,9,ny2,13)
  call data2(r(1),0.,xc2,1.8)
  call data2(xu(2),0.,yv(2),0.)
c   xl,yc1 and yl are in cm
  call data2(xl,30.0,yl,2.4)
  call data5(grx1,1.3,grx2,1.0,gry1,1.0,gry2,1.0,gry3,1.0)
  call data3(yc1,0.7,xsmall1,0.1,xsmall2,0.001)
  call data2(ysmall1,0.001,ysmall2,0.0001)
c-----
  call inta3(last,185,ichange,0,iprint,1)
c   time step, dt, in secs
  call data1(dt,1.0)
  call data2(relax(1),0.6,relax(2),0.6)
c-----system variables
c   pro2 (oxygen pressure) in torr;flux in 1.0e6 gms/cm2sec
  call data2(pro2,294.0,flux,16.32)
c   xmqliq in moles, flor in cm3/sec
  call data2(xmqliq,0.0552,flor,3.33)
c   texp, tsurf in K,total pressure (press) in torr
  call data3(texp,1391.0,tsurf,1391.0,press,700.0)
c-----physical constants
c   cond,cp,amuref,diff in appropriate cgs units
  call data3(cond,4.14e-4,cp,.52,gams,1.0e+20)
  call data2(amuref,4.78e-04,diff,3.0)
c-----start grid generation
  xc1=xl-xc2
  xl1=xc1-xsmall1
  do 1 i=3,nx1-1
1   xu(i)=xu(2)+xl1*(1.-(float(nx1-1-i)/float(nx1-1-2))**grx1)
  xu(nx1)=xu(nx1-1)+xsmall1
  nx1p1=nx1+1
  xl2=xc2-xsmall2

```

```

do 2 i=nx1p1,l1-1
2  xu(i)=xu(nx1)+xl2*(1.-(float(l1-1-i)/float(l1-1-nx1))**grx2)
   xu(l1)=xu(l1-1)+xsmall2
   yc2=yl-1.5-yc1
   yl1=yc1-ysmall1
   do 5 j=3,ny1-1
5  yv(j)=yv(2)+yl1*(1.-(float(ny1-1-j)/float(ny1-1-2))**gry1)
   yv(ny1)=yv(ny1-1)+ysmall1
   ny1p1=ny1+1
   yl2=yc2-ysmall2
   do 6 j=ny1p1,ny2-1
6  yv(j)=yv(ny1)+yl2*(1.-(float(ny2-1-j)/float(ny2-1-ny1))**gry2)
   yv(ny2)=yv(ny2-1)+ysmall2
   ny2p1=ny2+1
   yc3=yl-yc1-yc2
   do 7 j=ny2p1,nj
7  yv(j)=yv(ny2)+yc3*(1.-(float(nj-j)/float(nj-ny2))**gry3)
   return
c -----end grid generation
   entry begin
   startf='lanxst'
   savef='lanxst'
   call name2(title(5),'Temperature',title(6),'Composite wt frac')
   title(7)='Magnesium wt fraction'
   title(8)='Oxygen wt fraction'
   call data1(grea,1.0e+20)
c-----location of equi-temperature zone specified
   do 11 i=1,l1
   icrit=i-1
   if (x(i).gt.(xl-3.)) go to 12
11  continue
c -- tinlet is the inlet temperature of the gas
12  tinlet=((texp-298.0)*(31.0-x(icrit))/31.0)+298.0
c-----initial guess for temperature in the entire domain

```



```

do 16 i=1,l1
do 16 j=1,m1
16  t(i,j)=tinlet
c-----temperature distribution along the walls
do 17 i=1,l1
t(i,m1)=texp+((x(i)/x(icrit))-1.0)*(texp-tinlet)
if (i.ge.icrit)t(i,m1)=texp
17  continue
c-----temperature along melt surface and exit
do 18 j=1,m1
18  t(11,j)=tsurf
c    calculate uav and inlet velocity along AD
uav=flor*760.*tinlet/(298.0*3.1416*(yv(m1)**2)*press)
c-----velocity distribution at inlet
do 101 j=1,m1
101  u(2,j)=uav*2.*(1.-(y(j)/yl)**2)
c-----
do 110 nff=1,nfmax
ksolve(nff)=1
if (nff.gt.6) ksolve(nff)=0
kprint(nff)=1
110  kplot(nff)=1
c -- Mass transfer calculations begin -----
call data4(ammg,24.305,amar,39.95,amo2,32.0,amal,27.0)
c -- fluxmol: Mg flux in moles/cm2sec, fluxgm:Mg flux in gms/cm2sec
fluxmol=(flux*1.0e-06)/16.0
fluxgm=fluxmol*ammg
xo2b=pro2/press
c-----wo2b is the weight fraction of oxygen at the inlet
wo2b=1/(1+((1-xo2b)*amar/(xo2b*amo2)))
ai=amo2/(2.0*ammg)
c -- totcon is the total no of moles at the melt s/c
totcon=press/(760.0*tsurf*82.03)
c --  pmgs is the partial pr of Mg vapor in torr

```

```

c --  xmgliq is the mol fraction of Mg in the liq
      acon=-7550.0
      bcon=-1.41
      dcon=12.79
      pmg=(tsurf**(bcon))*(10.0**((acon/tsurf)+dcon))
c-----initial guess for concentration in the domain specified
      do 116 i=1,l1
      do 116 j=1,m1
116   wmgo2(i,j)=-wo2b/ai
      if (ichange.eq.1) call tools(start)
      return

c -----
      entry dense
c-----relaxation of density
      relden=0.6
      rel=1.0-relden
      do 150 j=1,m1
      do 150 i=1,l1

c-----determination of Mg concentration from composite conc.
      wmg(i,j)=amax1(0.0,wmgo2(i,j))
c-----determination of o2 concentration from composite conc.
      wo2(i,j)=amax1(0.0,-ai*wmgo2(i,j))
      war=1.0-wmg(i,j)-wo2(i,j)
      avmol=1.0/((wmg(i,j)/ammg)+(wo2(i,j)/amo2)+(war/amar))
      den=press*avmol/(760.0*82.03*t(i,j))
      if (iter.eq.0) rho(i,j)=den
150   rho(i,j)=den*relden+rho(i,j)*rel
c-----calculation of diffusivity of gas mixture
      do 200 j=1,m1
      do 200 i=1,l1
200   dgas(i,j)=diff*(700./press)*((t(i,j)/1391.)** 1.5)
      return

c -----
      entry output

```

```

        if(iter.ne.0) go to 300
        do 350 iunit=6,kdisk+6
350  write(iunit,301)
301  format(1x,'iter',2x,'time,s',2x,'wt gain,g',2x,'delta,cm',2x,'rsmax')
300  continue
c -----
c   Determination of Mg boundary layer thickness
        do 358 i=11-1,1,-1
        if (wmg(i,5).eq.0.0) then
            idelta=i-2
            dmax=x(i)
            go to 359
        endif
358  continue
359  delta=x(11)-dmax
c -----
        do 351 iunit=6,kdisk+6
351  write(iunit,303)iter,time,wtgain,delta,rsmax
303  format(2x,i3,1p4e10.3)
c----determination of weight gain as a function of time
c----corresponding Mg weight loss determined and alloy composition
c----in the melt corrected
        startwt=135.0/1000.0
        wtloss=wtloss+dt*3.14*(yc1**2.0)*flux11(2,6)
        wtgain=wtloss*ai
        wtinst=startwt-wtloss
        wtal=2565.0/1000.0
c----determination of new Mg concentration in the melt
        aliq=(wtinst)/ammg
        bliq=wtal/amal
        xmqliq=aliq/(aliq+bliq)
c----determination of activity coefficient of Mg in the melt
        coeff=0.89539-0.0035738*alog10(xmqliq)
c----determination of Mg vapor pressure over the melt

```

```

    pmgs=pmg*xmgliq*coeff
c -- cmgs is the equilibrium molar conc of Mg vapor
    cmgs=pmgs/(760.0*tsurf*82.03)
c -- xmgs is the eq mole fraction of Mg vapor
    xmgs=cmgs/totcon
c -- wmgs is the eq wt fraction of Mg vapor
    wmgs=1/(1+(((1-xmgs)*amar)/(xmgs*ammg)))
305  if(iter.ne.last)return
    if (iprint.eq.1) call tools(print)
c----plotting routine
    open (unit=18,file='plotinit')
    kflow=1
    write(18,9089)HEADER
9089  format(a64)
    write(18,9079)kflow,l1,m1,nfmax,mode,(kplot(nf),nf=1,nfmax)
9079  format(18i5)
    write(18,9069) (title(nf),nf=1,nfmax)
9069  format(4a18)
    write(18,9059)(x(i),i=1,l1),(y(j),j=1,m1),(xu(i),i=2,l1),
    1(yv(j),j=2,m1),(r(j),j=1,m1)
9059  format(5e12.6)
    do 9002 nf=1,nfmax
    if (kplot(nf).eq.0) go to 9002
    write(18,9059)((f(i,j,nf),i=1,l1),j=1,m1)
9002  continue
    do 360 iunit=6,kdisk+7
    write(iunit,*)'final delta, cm=',delta
    write(iunit,*)' fl rate=',flor,'cc/sec ',tinlet= ',tinlet
360  write(iunit,*)'pressure=',press,'torr ', 'po2= ',pro2
c-----tecplot output-----
    open (unit=44,file='dimox.tec')
    write(44,*) 'TITLE = "Initial oxidation"'
    write(44,*)'VARIABLES = "X", "Y", "TEM", "C(MG)","C(O)","U", "V"'
    write(44,*)'ZONE I=',l1,'J=',m1,'F=POINT'

```

```

do 9001 j=1,m1
do 9001 i=1,l1
write(44,9099)x(i),y(j),t(i,j),wmg(i,j),wo2(i,j),u(i,j),v(i,j)
9001 continue
9099 format(9(e14.4))
call tools(save)
return
c-----
entry outflo
if (iter.ne.0) go to 705
flow=0.0
c----determination of total inflow rate
do 701 j=1,m1
701 flow=flow+rho(1,j)*u(2,j)*arx(j)
705 fl=0.0
ars=0.0
umin=0.0
c----determination of total outflow rate
do 706 j=ny1,m1-1
ars=ars+rho(l1,j)*arx(j)
fl=fl+rho(l1,j)*arx(j)*u(l1,j)
if (u(l1,j).lt.0.) umin=amax1(umin,-u(l1,j))
706 continue
fact=flow/(fl+ars*umin+1.e-15)
c fact=flow/fl
c----outflow rate = inflow rate
do 707 j=ny1,m1-1
707 u(l1,j)=(u(l1,j)+umin)*fact
return
c-----
entry phi
if(nf.gt.2) go to 504
do 500 j=1,m1
do 500 i=1,l1

```

```

500  gam(i,j)=amuref
c-----u velocity in the crucible wall prescribed to be zero
c ----- viscosity in EFGH prescribed to be very large --
      do 488 i=nx1+1,l1-1
      do 488 j=ny1,ny2-1
      u(i,j)=0.0
488  gam(i,j)=gams
c-----v velocity in the crucible walls prescribed to be zero
      do 487 i=nx1+1,l1-1
      do 487 j=ny1,ny2
487  v(i,j)=0.0
      if(nf.ne.1) go to 492
c -- prescribe conditions at axis for u velocity -----
      do 489 i=2,l1-1
489  kbcj1(i)=2
c -- prescribe conditions along HC for u velocity -----
      do 494 j=ny2,m1-1
494  kbcl1(j)=2
      go to 504
492  continue
c --- specify the source term for v-velocity-----
      do 505 j=jst,m2
      do 505 i=ist,l2
505  sp(i,j)=-amuref/rv(j)**2
504  continue
      if(nf.ne.5) go to 610
c    gam for temperature specified
      do 602 i=1,l1
      do 602 j=1,m1
602  gam(i,j)=cond/cp
c    prescribe conditions at axis for temperature
      do 603 i=1,l1
603  kbcj1(i)=2
610  if (nf.ne.6) return

```

```

c    gam for weight fraction specified
      do 620 i=1,11
        do 620 j=1,m1
620   gam(i,j)=dgas(i,j)*rho(i,j)
c-----composite weight fraction at inlet specified
      do 117 j=1,ny1-1
117   wmgo2(11,j)=wmgs
c -- conc inside EFGH specified as zero
      do 851 j=ny1,ny2-1
        do 851 i=nx1+1,11
          gam(i,j)=0.0
          sc(i,j)=0.0
851   sp(i,j)=-grea
c    conc flux specified along EC
      do 843 j=ny1,m1
843   kbcl1(j)=2
c    flux specified along axis
      do 852 i=1,11
852   kbcj1(i)=2
c    conc flux along CD specified as zero-----
      do 1000 i=1,11
1000  kbcm1(i)=2
      return
c-----
      entry lc
      return

```

CAUTION: -- DO NOT DELETE OR ALTER THE FOLLOWING STATEMENT

```
$include: 'FINISH.FOR'
```

```
end
```

Parameter Statement:

The variables which required to be solved here are temperature, the composite concentration of magnesium vapor and oxygen (wmgo2), and concentrations of magnesium vapor and oxygen. Therefore, NFMAX is set equal to 8. The values of NI and NJ are set to be equal to 40 and 20 respectively.

Dimension and Equivalence Statement:

The dimensions of temperature are declared as $T(NI,NJ)$. Furthermore, $T(I,J)$ is made equivalent to $F(I,J,5)$. Similarly, $wmgo2(I,J)$, $wmg(I,J)$, and $wo2(I,J)$ are introduced and made equivalent to $F(I,J,NF)$ for $NF= 6,7$, and 8 respectively.

Entry Grid:

The length of the computational domain is $2.4\text{ cm} \times 30\text{ cm}$ (declared using $x1$ and $y1$). The size of the grid is 20×40 (declared using $l1$ and $m1$). The grid spacing is decided according to a power-law expression. The grids are generated in such a way that the grid spacing gets progressively small towards the crucible walls and towards the melt surface. The time step (dt) is specified since this is an unsteady-state problem.

Entry Begin:

A total of 185 iterations is planned. So "last" is declared as 185. The temperature distribution along the reactor walls is specified. The temperature, velocity and composite concentration at the inlet are also prescribed. In addition, the composite concentration and the temperature at the melt surface are specified. The only independent concentration variable is $wmgo2(I,J)$. Therefore, the variables to be solved for other than velocity are temperature and composite concentration. Hence, $ksolve(5)$, $kprint(5)$ and similarly, $ksolve(6)$ and $kprint(6)$ are made equal to 1.

Entry Dense:

The density of the gas mixture depends on the concentration of the constituent atoms (oxygen, magnesium, argon). Since concentration varies with location in the gas phase, the density also varies. The dependence of density on concentration is specified here. The quantity $RELDEN$ is used to underrelax the density ρ .

Entry Output:

The output is designed in two parts: a one-line output after every iteration and a field printout of the converged solution at the end.

The rate of Mg vaporization and the corresponding oxygen weight gain is calculated for every iteration. The change in the Mg composition in the alloy is also updated. The thickness of the magnesium boundary layer and the total weight gain on oxidation are also determined for every iteration. The velocity, temperature and concentration at various grid points are also monitored. Also the output for viewing the data using $TECPLOT$ is written after the last iteration. When $ITER$ equals $LAST$, the routine $PRINTUN$ is called to obtain the field printout.

Entry Outflo:

The outflow velocities at the exit are to be adjusted in OUTFLO so that they satisfy overall mass conservation. At first the inflow rate is calculated by integrating the flow rate over the inflow points. Since the inflow rate does not change, it is sufficient to evaluate it only once. Therefore, its calculation is not repeated when ITER equals zero.

Entry Phi:

With velocity as the variable, the corresponding GAM(I,J) is viscosity, μ . Viscosity in the crucible walls is specified to be large. With temperature as the variable, the corresponding GAM(I,J) is k/c_p , where k is the thermal conductivity and c_p is the specific heat. With concentration as the variable, the corresponding GAM(I,J) is $D\rho$ where D is the diffusion coefficient and ρ is the density of the gas mixture. After the specification of the array GAM(I,J), attention is turned to the source terms. Here, the source terms for concentration and temperature are zero. The only additional nonzero momentum source term is $-\mu v/r^2$.

The boundary conditions for velocity, temperature and concentration are specified here. The axis of symmetry is a zero-flux boundary for all variables except v , for which a zero value is specified on the axis. Along the wall CD, u and v are given to be zero, while the diffusion flux is zero for $wmgo2$ and t . At the crucible walls, concentration flux is specified as zero. At the exit (EC), velocity, concentration and temperature gradients are specified as zero. These considerations are used in specifying the values of KBC indicators.

Entry Lc:

No action is needed in this entry.

The data used for a sample calculation along with the resulting output is presented in Table B.1.

Table B.1 Sample calculation using the program for initial stage.

	filenames	
1	output file name	printun
2	plot file name	dimox.tec
3	start file name	lanxst

	geometric variables	
1	half width of Al-Mg alloy melt (cm)	0.7
2	radius of the reactor (cm)	2.4
3	length of reactor (cm)	30
4	height of crucible above melt (cm)	1.9
5	width of crucible wall (cm)	0.1
6	number of grids: radial direction (y)	15
7	number of grids: axial direction (x)	40

material properties		
1	thermal conductivity (J/(m s K))	4.14×10^{-2}
2	specific heat (J/Kg K)	520
3	diffusion coefficient (m ² /s)	3×10^{-4}
4	viscosity (Kg/m s)	4.78×10^{-5}

process parameters		
1	oxygen pressure (Pa)	39187
2	total pressure (Pa)	93303
3	experimental temperature (K)	1391
4	total gas flow rate (cm ³ /s)	3.33
5	initial mole fraction of Mg in the melt (%)	5.5
6	duration of initial stage (s)	185

numerical scheme parameters		
1	velocity relaxation parameter	0.6
2	concentration relaxation parameter	0.6
3	time increment (s)	1
4	number of iterations	185

Output file: "Printun"

output		
	time, s	weight gain, mg
1	0	0
2	30	7.13
3	60	14.05
4	90	20.85
5	120	27.60
6	150	34.32
7	185	42.12

U velocity, cm/s						
	I=2	I=10	I=18	I=26	I=34	I=40
J=20	0.00	0.00	0.00	0.00	0.00	0.00
J=10	0.528	1.15	0.772	$5.9e-26$	$3.2e-26$	0.00
J=5	0.577	1.27	0.444	$4.4e-4$	$-1.6e-5$	0.00
J=1	0.595	1.31	0.338	$-7.2e-3$	$-3.5e-5$	0.00

V velocity, cm/s						
	I=1	I=10	I=18	I=26	I=34	I=40
J=20	0.0	0.0	0.0	0.0	0.0	0.0
J=10	0.00	$-1.9e-3$	$2.6e-1$	$-5.4e-27$	$-2.7e-27$	0.00
J=5	0.00	$-1.1e-3$	0.104	$-3.25e-3$	$-9.9e-6$	0.00
J=2	0.00	0.00	0.00	0.00	0.00	0.00

Temperature, K						
	I=1	I=10	I=18	I=26	I=34	I=40
J=20	4.43e2	1.03e3	1.39e3	1.39e3	1.39e3	1.39e3
J=10	4.43e2	1.01e3	1.37e3	1.38e3	1.39e3	1.39e3
J=5	4.43e2	1.01e3	1.37e3	1.38e3	1.39e3	1.39e3
J=1	4.43e2	1.01e3	1.37e3	1.38e3	1.39e3	1.39e3

Magnesium weight fraction in the gas phase						
	I=1	I=10	I=20	I=37	I=38	I=40
J=20	0.0	0.0	0.0	0.0	0.0	0.0
J=10	0.0	0.0	0.0	0.0	0.0	0.0
J=8	0.0	0.0	0.0	0.0	9.1e-3	2.0e-2
J=1	0.0	0.0	0.0	0.0	9.1e-3	2.0e-2

Oxygen weight fraction in the gas phase						
	I=1	I=10	I=20	I=35	I=37	I=40
J=20	3.67e-1	3.66e-1	3.27e-1	3.25e-1	3.24e-1	3.67e-1
J=10	3.67e-1	3.66e-1	2.89e-1	0.00	0.00	0.00
J=5	3.67e-1	3.66e-1	2.52e-1	3.7e-2	8.2e-3	0.00
J=1	3.67e-1	3.66e-1	2.46e-1	3.7e-2	8.2e-3	0.00

APPENDIX C

ESTIMATION OF ACTIVITY COEFFICIENTS OF MAGNESIUM AND ALUMINUM IN Al-Mg-Si MELT

c----- definitions of terms used in the program-----

- c T is the temperature in K
- c gamal is the activity coefficient of aluminum at composition A in Figure 3.5 at temperature T
- c gammg is the activity coefficient of magnesium at composition A in Figure 3.5 at temperature T
- c xsi is the mole fraction of silicon in the melt at composition A in Figure 3.5
- c xmg is the mole fraction of magnesium in the melt at composition A in Figure 3.5
- c xal is the mole fraction of aluminum in the melt at composition A in Figure 3.5
- c xsialsi is the mole fraction of silicon at composition R in Figure 3.5
- c xalalsi is the mole fraction of aluminum at composition R in Figure 3.5
- c xmngmsi is the mole fraction of magnesium at composition Q in Figure 3.5
- c xsimgsi is the mole fraction of silicon at composition Q in Figure 3.5
- c amuexmgsi is the excess partial molar free energy of mixing of Mg in the Mg-Si binary at composition Q
- c amuexalmg is the excess partial molar free energy of mixing of Mg in the Al-Mg binary at composition P
- c amuexalsi is the excess partial molar free energy of mixing of Al in the Al-Si binary at composition R
- c amuexalmg is the excess partial molar free energy of mixing of Mg in the Al-Mg binary at composition P
- c gexalsi is the excess free energy of mixing of Al-Si binary at composition R
- c gexmgsi is the excess free energy of mixing of Mg-Si binary at composition Q
- c asumalmg is the first term on the right hand side of equation (3.3)
- c asummgsi is the second term on the right hand side of equation (3.3)
- c asumalsi is the third term on the right hand side of equation (3.3)
- c amuexmgalmgsi is the term on the left hand side of equation (3.3)
- c amuexmgalmgsi is the excess partial molar free energy of mixing of Mg in the Al-Mg-Si ternary at composition A
- c alsalsi is the first term on the right hand side of equation (3.4)
- c alsalmg is the second term on the right hand side of equation (3.4)
- c alsimgsi is the third term on the right hand side of equation (3.4)

```

c    amuexalalmgsi is the term on the left hand side of equation (3.4)
c    amuexalalmgsi is the excess partial molar free energy of mixing of Al in the Al-
Mg -Si ternary at composition A
read(*,*) xsi,xmg,T
c    estimation of composition Q
xmgmgsi=xmg+xal/2.0
xsimgsi=xsi+xal/2.0
c    estimation of composition R
xsialsi=xsi+xmg/2.0
xalalsi=xal+xmg/2.0
c    estimation of activity coefficient of Mg in Al-Mg-Si melt (composition A) at
temperature T
amgsi(1)=-1.6375*(10.0**5.0)
bmgsi(1)=-0.99474*(10.0**2.0)
amgsi(2)=0.57976*(10.0**5.0)
bmgsi(2)=0.35266*(10.0**2.0)
amgsi(3)=6.9610*(10.0**5.0)
bmgsi(3)=7.0744*(10.0**2.0)
amgsi(4)=-9.8494*(10.0**5.0)
bmgsi(4)=-12.939*(10.0**2.0)
amgsi(5)=0.0
bmgsi(5)=-5.0384*(10.0**2.0)
amgsi(6)=0.0
bmgsi(6)=-0.83281*(10.0**2.0)
asum=0.0
do 10 j=1,6
i=j-1.0
asum=asum+(amgsi(j)-bmgsi(j)*T)*(1.0-(i*(xmgmgsi**i))-(xmgmgsi**i))
10  continue
amuexmgsi=((1.0-xmgmgsi)**2.0)*asum
asummgsi=amuexmgsi*xsi*(xal+xsi)/((xsi+xal/2.0)**2.0)
c    estimation of gexalsi
aalsi=-10695.4-1.823*T
balsi=-4274.5+3.044*T
calsi=670.7-0.460*T

```

```

gexalsi=aalsi+balsi8(1-2.0*xsialsi)+calsi*(1.0-6.0*xsialsi+6.0*(xsialsi**2.0))
gexalsi=gexalsi*xsialsi*(1.0-xsialsi)
asumalsi=xal*xsi*gexalsi/((xal+xmg/2.0)*(xsi+xmg/2.0))
c estimation of amuexalmg
amuexalmg=(-1630.2+1.0292*T)*4.2
asumalmg=xal*(xal+xsi)*amuexalmg/((xal+xsi/2.0)**2.0)
amuexmgalmgsi=asummgsi-asumalsi+asumalmg
gammg=exp(amuexmgalmgsi/(8.314*T))
c
c estimation of activity coefficient of Al in Al-Mg-Si melt (composition A) at
temperature T
amuexalsi=(aalsi+4.0*balsi*xalalsi-balsi+calsi-12.0*xalalsi*calsi+18.0*
1 calsi*(xalalsi**2.0))*((1.0-xalalsi)**2.0)
asalsi=amuexalsi*xsi*(xsi+xmg)/((xsi+xmg/2.0)**2.0)
amuexmgal=(9.0-8.4*(10**(-3.0))*T)*4.2
asalmg=amuexalmg*xmg*(xsi+xmg)/((xsi+xmg/2.0)**2.0)
bsum=0.0
do 20 j=1,6
i=j-1
gexmgsi=bsum+(amgsi(j)-bmgsi*T)*((1.0-xmgmgsi)**i)
bsum=gexmgsi
20 continue
asmgsi=gexmgsi*xsi*xmg/((xsi+xal/2.0)*(xmg+xal/2.0))
amuexalalmgsi=asalsi+asalmg-asmgsi
gamal=exp(amuexalalmgsi/(8.314*T))
write (*,*) gamal, gammg
stop
end

```

APPENDIX D

DETERMINATION OF RATE EXPRESSION FOR LIQUID METAL TRANSPORT

The volumetric flow rate of the liquid alloy through existing capillaries in the composite is given by the Poiseuille equation:

$$\frac{dV}{dt} = \frac{\pi R^4 \Delta P}{8\mu x} \quad (D1)$$

where R is the capillary radius, ΔP is the pressure difference driving the flow, μ is the viscosity of the liquid alloy, and x is the depth of penetration of the liquid at time, t . The pressure difference, ΔP can be represented as:

$$\Delta P = P_c - P_v - P_g \quad (D2)$$

where P_c is the capillary pressure, P_v is the vapor pressure of magnesium in the channel, and P_g is the gravitational pressure due to the weight of the liquid in the channel. The capillary pressure, P_c , driving the flow is given by the expression:

$$P_c = \frac{2\gamma_{LV} \cos \theta}{R} \quad (D3)$$

where γ_{LV} is the surface tension of the liquid aluminum alloy and θ is the contact angle between the liquid Al alloy and alumina. Exact values of the contact angle, θ , and the surface tension, γ_{LV} , are not available. However, they can be estimated as shown below.

From Young's equation [1], we have

$$\gamma_{LV} \cos \theta = \gamma_{SV} - \gamma_{SL} \quad (D4)$$

where γ_{SV} is the surface energy of alumina and γ_{SL} is the interfacial energy between the molten aluminum alloy and the solid Al_2O_3 . Since the metal channels are present in the

grain boundaries of alumina [2], the metal is considered to have spread along the grain boundaries. The condition for metal spreading is given by the following equation:

$$\gamma_{SL} \leq \frac{\gamma_{SS}}{2} \quad (D5)$$

where γ_{SS} is the grain boundary energy in alumina. A lower estimate for $\gamma_{LV} \cos\theta$ is therefore, given as:

$$\gamma_{LV} \cos\theta = \gamma_{SV} - \frac{\gamma_{SS}}{2} \quad (D6)$$

From equation (D4) it can be seen that the higher estimate for $\gamma_{LV} \cos\theta$ can be determined by setting γ_{SL} as zero. Approximate values of γ_{SV} and γ_{SS} can be estimated from the data of Nikolopoulos [3]. The lower and the higher estimates for $\gamma_{LV} \cos\theta$ at 1373 K are 0.9455 J/m² and 1.4826 J/m² respectively.

For the lower estimate of $\gamma_{LV} \cos\theta$, P_C is 9.884×10^5 N/m² at 1373 K. From Table 4.2, it is seen that P_G and P_V are much smaller than P_C and are therefore neglected in the determination of ΔP . Therefore, the mass flow rate of Al, (dM/dt) in moles/sec, through a single metal channel is given as:

$$\frac{dM}{dt} = \rho_{Al} \frac{dV}{dt} = \frac{\rho_{Al} \pi R^3 \gamma_{LV} \cos\theta}{4\mu x} \quad (D7)$$

If f is the ratio of the total metal channel area to the area of the composite, the total mass flow rate of Al per unit area of the composite is $\frac{f}{\pi R^2} \frac{dM}{dt}$. Formation of alumina requires 48 grams of oxygen for every 54 grams of aluminum. Hence the oxygen weight gain rate per unit area, J , is given as:

$$J = \frac{48}{54} f \frac{dM}{dt} = \frac{48}{54} f \rho_{Al} R \gamma_{LV} \cos\theta \quad (D8)$$

Equation (D1) can be rewritten as:

$$\pi R^2 \frac{dx}{dt} = \frac{\pi R^4 \Delta P}{8\mu x} = \frac{\pi R^3 \gamma \cos \theta}{4\mu x} \quad (\text{D9})$$

Integrating Equation (D9) we get an expression for the depth of liquid penetration, x , as a function of time, t .

$$x = \left[\frac{Rt\gamma_{LV} \cos \theta}{2\mu} \right]^{\frac{1}{2}} \quad (\text{D10})$$

Using the above expression for x in equation (D8) we get a relation between the flux, J , and the time of oxidation, t .

$$J = \frac{48}{54} f \frac{\rho_{Al}}{4} \left[\frac{2R\gamma_{LV} \cos \theta}{\mu t} \right]^{\frac{1}{2}} \quad (\text{D11})$$

References

1. L. E. Murr, *Interfacial Phenomena in Metals and Alloys*, Addison Wesley, Reading, Mass., 1975.
2. M. S. Newkirk, A. W. Urquhart, H. R. Zwicker and E. Breval, "Formation of Lanxide™ Ceramic Composite Materials," *J. Mater. Res.*, **1** [1] 81-89 (1986).
3. P. Nikolopoulos, "Surface, Grain-Boundary and Interfacial Energies in Al₂O₃ and Al₂O₃-Sn, and Al₂O₃-Co Systems," *J. Mat. Sci.*, **20**, 3993-4000 (1985).

APPENDIX E

DETERMINATION OF ELECTRICAL CONDUCTIVITY OF AN Al₂O₃/Al COMPOSITE CONTAINING TORTUOUS METAL CHANNELS

Consider an Al₂O₃/Al composite containing Al metal in the form of channels of varying tortuosities as shown in Figure E.1. The resistances of the various Al metal channels, R_i, are given by the following expressions:

$$R_1 = \frac{\rho_{Al}L_1}{A_1}, \quad R_2 = \frac{\rho_{Al}L_2}{A_2}, \quad R_n = \frac{\rho_{Al}L_n}{A_n} \quad (E1)$$

where L_i denotes the length of channel i, A_i the area of channel i, and ρ_{Al} denotes the resistivity of Al. The total resistance of the composite, R_c, is given by the expression:

$$\frac{1}{R_c} = \frac{A_c}{\rho_c L_c} = \frac{A_1}{L_1 \rho_{Al}} + \frac{A_2}{L_2 \rho_{Al}} + \dots + \frac{A_n}{L_n \rho_{Al}} \quad (E2)$$

where A_c denotes the total cross-sectional area of the composite, L_c the thickness of the composite, and ρ_c denotes the resistivity of the composite. If the metal channels are assumed to be of equal length and cross-sectional area, i.e., A₁= A₂= -----= A_n= A_i, and L₁= L₂= -----= L_n= L_i, equation (E2) can be simplified as:

$$\rho_c = \frac{\rho_{Al}L_i A_c}{nA_i L_c} = \frac{\rho_{Al} \tau}{f_m} \quad (E3)$$

where τ = L_i/L_c= tortuosity factor and f_m is the fractional metal channel area given by:

$$f_m = \frac{nA_i}{A_c} \quad (E4)$$

It follows from equation (E3) that the conductivity of the composite, σ_c, is given by:

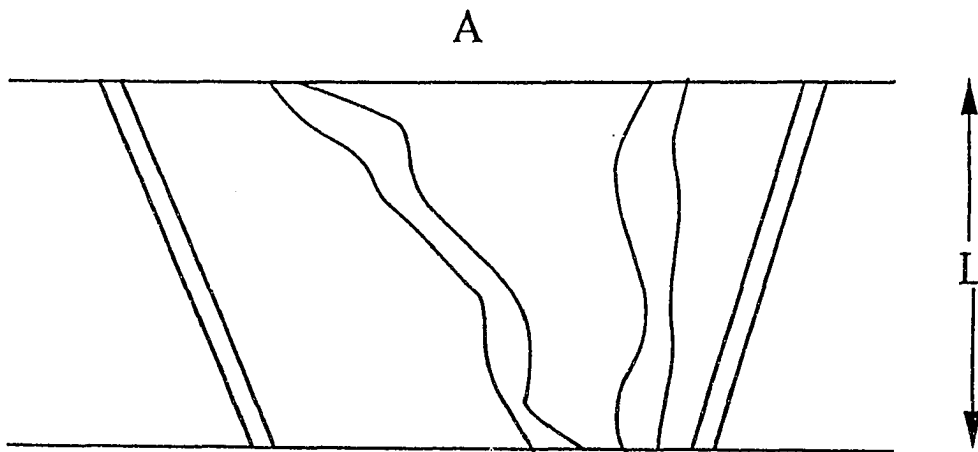


Fig. E.1 Schematic representation of metal channels in an $\text{Al}_2\text{O}_3/\text{Al}$ composite.

$$\sigma_c = \frac{\sigma_{Al} f_m}{\tau} \quad (E5)$$

where σ_{Al} denotes the conductivity of aluminum.

VITA

Hari Venugopalan was born in Madras, India, on 18 August 1970. After completion of his high school education in 1987, he joined Regional Engineering College, Tiruchirapalli, India and graduated with a B.E degree in Metallurgical Engineering in 1991. He was adjudged the best B.E student in the Department of Metallurgical Engineering in 1991. He then obtained a M.E degree in Metallurgy from the Indian Institute of Science, Bangalore, India, in 1993. His master's research work was declared the best M.E thesis in Metallurgy in 1993. He then joined the Pennsylvania State University, in Fall' 93, to pursue doctoral studies in Materials Science and Engineering. He is a student member of the American Ceramic Society, and the American Society of Metals. The following is a list of his publications.

1. H. Venugopalan, K. Tankala and T. DebRoy, "Electrical Conductivity of Alumina/Aluminum Composites Synthesized by Directed Metal Oxidation," *J. Am. Ceram. Soc.*, **77** [11] 3045-47 (1994).
2. H. Venugopalan, K. Tankala and T. DebRoy, "Probing the Initial Stage of Synthesis of Al₂O₃/Al Composites by Directed Oxidation of Al-Mg Alloys," accepted for publication in *Metallurgical and Materials Transactions*.
3. H. Venugopalan, K. Tankala and T. DebRoy, "Kinetics of Oxidation of Al-Mg Alloys in the Initial and Final Stages of Synthesis of Al₂O₃/Al Composites", accepted for publication in *Materials Science and Engineering A*.
4. H. Venugopalan and T. DebRoy, "Growth Stage Kinetics in the Synthesis of Al₂O₃/Al Composites by Directed Oxidation of Al-Mg and Al-Mg-Si Alloys", submitted for publication.
5. H. Venugopalan and T. DebRoy, "Metal Distribution in Alumina/Aluminum Composites Synthesized by Directed Metal Oxidation", submitted for publication.